

Low Noble Metal Content Catalysts for Hydrogen Fuel Technology

Westsson, Emma

DOI

[10.4233/uuid:c97f643c-002f-4dc9-a243-2df4f9a784b1](https://doi.org/10.4233/uuid:c97f643c-002f-4dc9-a243-2df4f9a784b1)

Publication date

2019

Document Version

Final published version

Citation (APA)

Westsson, E. (2019). *Low Noble Metal Content Catalysts for Hydrogen Fuel Technology*. [Dissertation (TU Delft), Delft University of Technology]. <https://doi.org/10.4233/uuid:c97f643c-002f-4dc9-a243-2df4f9a784b1>

Important note

To cite this publication, please use the final published version (if applicable).
Please check the document version above.

Copyright

Other than for strictly personal use, it is not permitted to download, forward or distribute the text or part of it, without the consent of the author(s) and/or copyright holder(s), unless the work is under an open content license such as Creative Commons.

Takedown policy

Please contact us and provide details if you believe this document breaches copyrights.
We will remove access to the work immediately and investigate your claim.

Low Noble Metal Content Catalysts for Hydrogen Fuel Technology

Dissertation

for the purpose of obtaining the degree of doctor
at Delft University of Technology
by the authority of the Rector Magnificus prof. dr. ir. T.H.J.J. van der Hagen
chair of the Board of Doctorates
to be defended publicly on

20 September 2019 at 10:00

by
Emma WESTSSON

Master of Science in Engineering Chemistry,
Umeå University
Born in Umeå, Sweden

This dissertation has been approved by the promotor:

Prof.dr. S. J. Picken and Dr.ing. G. J. M. Koper

Composition of the doctoral committee:

Rector Magnificus,	chairperson
Prof.dr. S. J. Picken	Delft University of Technology, promotor
Dr.ing. G. J. M. Koper	Delft University of Technology, promotor

Independent members:

Prof.dr.techn.ing. S. Kjelstrup	Norwegian University of Science & Technology
Prof.dr. F. M. Mulder	Delft University of Technology
Dr.ir. M.A. van der Veen	Delft University of Technology
Prof.dr. M.T.M. Koper	University of Leiden
Prof.dr. J.J.C. Geerlings	Delft University of Technology
Prof.dr. F.M. Mulder TNW	Delft University of Technology
Prof.dr. L.D.A. Siebbeles	Delft University of Technology (reserve member)

The work described in this thesis was carried out in the Advanced Soft Matter (ASM) group at Delft University of Technology, the Faculty of Applied Sciences, the Department of Chemical Engineering. This thesis is part of NanoNextNL, a micro and nanotechnology innovation consortium of the Government of the Netherlands and 130 partners from academia and industry. More information on www.nanonextnl.nl.



Copyright © Emma Westsson, 2019

ISBN 978-94-028-1696-9

Cover design: Emma, Maja and Alice Westsson

Printed by Ipskamp

All rights reserved. The author encourages the communication of scientific contents and explicitly allows reproduction for scientific purposes, provided the proper citation of the source. Parts of the thesis have been published in scientific journals and copyright is subject to different terms and conditions.

An electronic version of this thesis is freely available at <http://repository.tudelft.nl>

To my family

In memory of Tore

*“Nothing in life is to be feared, it is only to be understood. Now is the time
to understand more, so that we may fear less.”*

Marie Curie Skłodowska, first female Noble Prize winner

Table of contents

1	Introduction.....	1
1.1	General introduction to this thesis.....	1
1.2	Electrocatalysis.....	2
1.3	Aim of this thesis.....	4
1.3.1	Designing low-Pt content catalysts.....	4
1.3.2	Manipulating catalyst properties.....	5
1.3.3	Organometallic catalysts.....	6
2	Synthesis of core-shell particles in bi-continuous micro-emulsion.....	7
2.1	Abstract.....	7
2.2	Introduction.....	8
2.3	Materials and Methods.....	9
2.3.2	Micro-emulsion preparation.....	9
2.3.3	Synthesis of transition metal cores.....	10
2.3.4	Galvanic replacement.....	10
2.3.5	Synthesis of pure Pt and Ag reference particles.....	11
2.3.6	Nanoparticle characterization.....	11
2.4	Results for Pt@Me.....	14
2.4.1	Synthesis.....	14
2.4.2	Characterization.....	15
2.5	Results for Ag@Me.....	21
2.5.1	Synthesis.....	21
2.5.2	Characterization.....	22
2.6	Discussion.....	23
2.7	Conclusions.....	27
3	How to determine the core-shell nature in bimetallic catalyst particles?.....	29
3.1	Abstract.....	29
3.2	Introduction.....	30
3.3	Methods.....	32
3.3.1	Electron Microscopy/Spectroscopy.....	32
3.3.2	X-ray Scattering.....	34

3.3.3 Absorption Spectroscopies.....	35
3.3.4 Other	36
3.4 Results	37
3.4.1 Electron Microscopy and Spectroscopy	38
3.4.2 X-ray Scattering	40
3.4.3 Absorption Spectroscopies.....	41
3.4.4 Other	42
3.5 Discussion	43
3.6 Conclusion	44
4 The effect of lattice strain on catalytic activity	45
4.1 Abstract	45
4.2 Introduction.....	46
4.3 Materials and methods	50
4.3.1 Instrumentation and Measurements.	50
4.3.2 Electrochemical measurements.	50
4.4 Results	51
4.4.1 XRD response.....	51
4.4.2 Catalytic performance.	53
4.4.3 Activity vs strain	53
4.5 Discussion	55
4.5.1 Characterisation	55
4.5.2 Catalytic performance	56
4.5.3 Activity vs strain	57
4.6 Conclusions.....	59
5 The effect of magnetic field on catalytic properties in core-shell type particles.....	61
5.1 Abstract	61
5.2 Introduction.....	62
5.3 Materials and Methods	64
5.3.1 Setup.....	64
5.3.2 Experimental	65
5.4 Results	66
5.5 Discussion	69
5.6 Conclusions.....	73
Appendix Chapter 5.....	74

6 The ambiguity of the active centre in noble metal electrocatalyst alternatives.....	77
6.1 Abstract	77
6.2 Introduction.....	78
6.3 The role of nitrogen in doped graphitic structures	79
6.4 The role of transition metals in doped graphitic structures	83
6.5 Dopant free graphitic structures	84
6.6 Conclusions.....	85
Summary	87
Samenvatting.....	89
Bibliography.....	92
Acknowledgements	103
About the author.....	106

1 Introduction

1.1 General introduction to this thesis

Energy related challenges

The energy thirst of modern society is unprecedented. Our ability to efficiently appropriate energy has enabled us to improve our standard of living multifold in the last few centuries. Despite the large split in living conditions across the world, reports about global progress indicate that the proportion of the world population living in extreme poverty has almost halved in the last 20 years [1, 2]. This is an enormous success. Inevitably energy is a part of the success story. In the last 100 years the total energy use of the world population has increased more than 15 times. This is to be compared with a population growth that doubled during the same period [3]. From a global perspective, energy use per capita is however severely distorted. Europe and North America, together adding up to approximately 15 % of the world population, are using around half of the current worldwide energy conversion. Unfortunately such energy demand comes at a high price, not the least in terms of a number of negative effects on the global climate [4]. Excessive and often inefficient energy use are resulting in the release of large quantities of greenhouse gases, such as carbon dioxide and methane, into the atmosphere. Simultaneously, our natural carbon dioxide buffers – forests – are removed at a high pace, giving way to e.g. pasture for (methane emitting) livestock. It is no longer an academic debate whether or not human activities have a direct effect on the temperature rise in the atmosphere and significantly altering the ecosystems. In 2015 one important milestone in global action against rising greenhouse gas emissions was reached with the Paris agreement [5]. A treaty signed by every independent nation on the planet, urging nations to reduce emissions in order to keep global temperature rise below 1.5 °C above pre-industrial levels. IPCC (Intergovernmental Panel Climate Change of United Nations) concludes that if the 1.5 °C limit is to be reached, emissions must be cut from 2010 levels by 45% by 2030 and to net zero by 2050 [4]. A study at Stanford estimates that hitting 1.5 °C instead of 2 °C will save the world \$30 trillion in climate related damages by 2030 [6].

In order to stop depletion of our energy conversion material resources and to ensure minimal human influence on the ecosystem of the planet, a combined approach is needed; a reduction of the global energy conversion as well as more efficient and less polluting conversion techniques. Economic incentives alongside political decisions and technological advancements are currently challenging old energy infrastructure. It is inevitable that the previously dominating oil and gas based energy supply will be completely replaced by a myriad of other technologies, such as wind, solar, hydroelectric etc. The average share of renewable energy in Europe today is approximately 20% [7]. Around 30% of the total energy conversion in Europe accounts for transportation, of which only approximately 0.5% are non-fossil fuelled. In order to facilitate the impressive energy transition lying ahead of us, the European Commission Research Council has defined the theme of Renewable Energy as being of utmost priority, fuelling an ever-growing research interest in sustainable energy storage and conversion technologies.

Many questions still remain as to which technology will play a role in which sector, and which fuel will be produced where and how. However, remarkable advancements have been made in recent years in the fields of batteries, fuel cells, electrolyzers, photovoltaics, wind and geothermal energy etc., taking commercialisation beyond subsidy dependence.

It has been predicted that hydrogen will play a major role in the future renewable energy economy, in view of its high energy density and natural abundance. Hydrogen is the simplest fuel alternative for a fuel cell – an electrochemical device converting chemical energy to electrical energy with little pollutant emission and high energy conversion efficiency. Furthermore, fuel cells offer flexibility, both in terms of operating temperature range and fuel type as well as size and weight. These advantages allow fuel cell technology to extend its applications to transportation (such as cars and buses), stationary power units (for domestic as well as public buildings), portable applications (such as mobile chargers) and special applications like power units in combination with freshwater supply on space shuttles [8]. On a small scale there are already examples demonstrating how these applications intertwine, showing an example of what a hydrogen economy potentially could look like, involving domestic energy generation, storage and hydrogen-powered transportation [9, 10].

Way before the first prototype of a fuel cell had been sketched, Jules Verne predicted in 1877 [11]:

“Water will one day be employed as fuel, that hydrogen and oxygen which constitute it, used singly or together, will furnish an inexhaustible source of heat and light, of an intensity of which coal is not capable... When the deposits of coal are exhausted we shall heat and warm ourselves with water. Water will be the coal of the future.”

Unfortunately electrochemical conversion of water into its substituents and back, is not as easy as described by Jules Verne, but relies on advanced electrocatalysts. Despite the technology being the subject of on-going humour saying that “Fuel cell technology is always 10 years away” [12], perhaps the future Jules Verne is referring to is now.

1.2 Electrocatalysis

Three seemingly simple reactions, the oxygen reduction reaction (ORR), oxygen evolution reaction (OER) and hydrogen evolution reaction (HER) and the catalysts accelerating them, all play key roles in renewable energy technologies [13-18]. Hydrogen fuel generation can be achieved by HER via photo-electrochemical water splitting, ORR enables energy conversion in fuel cells and through OER energy can be stored in metal–air batteries. In essence these catalysed reactions are similar, all involving adsorption of reactants and intermediates, electron transfer and desorption.

Thermodynamically, electrochemical energy conversion has an overall higher efficiency than conventional energy conversion system, for example internal combustion engines (ICE) in which the maximum efficiency is limited by the Carnot cycle [19]. Fuel cells offer electric efficiency rates up to 70% which greatly exceeds conventional power production technologies. An overview of the various fuel cell types and their basics is illustrated in Fig 1 and in various excellent books [19-21]. About 75% of all shipped fuel cell units during 2017 were Polymer Electrolyte Membrane Fuel Cells (PEMFC) [22]. The high share is partly due to their dominance in automobiles, fork lift trucks and telecommunication due to the low operating temperatures (<90 C).

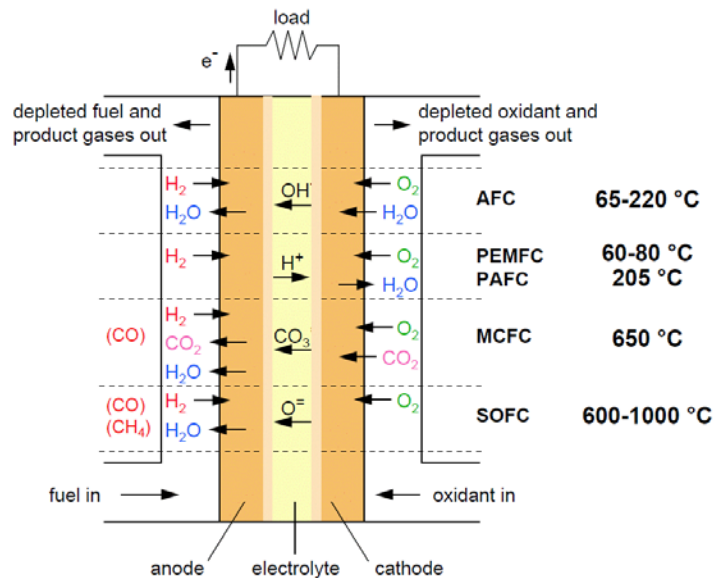


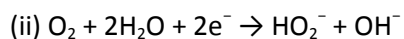
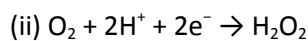
Figure 1 Overview of fuel cell types. Adapted from Ref [19]

In a PEMFC oxygen reduction takes place on the cathode and hydrogen oxidation on the anode. HOR is a one-electron transfer reaction with a relatively low activation barrier meaning it can be catalysed with low catalyst loadings and still remain at a low overpotential [20]:



Typically platinum is used as a catalyst on the anode. Despite the relatively low contribution of overall fuel cell voltage drop from the HOR, there is still substantial on-going research addressing replacement of platinum on the PEMFC anode.

The reduction of oxygen on the cathode side, on the other hand, is a multi-electron transfer reaction involving breaking the double bond of the oxygen molecule. The performance of PEM fuel cells largely depends on the catalytic activity of the cathode catalyst [23, 24]. In other words, the ORR overpotential at the cathode is the main contributor to the fuel cell voltage drop when polarized by a load. ORR proceeds mainly through two different pathways; direct 4-electron transfer (i) or 2-electron transfer via peroxide formation (ii) [25]:



Current commercial PEMFCs use platinum nanoparticles as a catalyst speeding up the oxygen reduction reaction. What does it take to catalyse the oxygen reduction reaction? The reaction is a multi-electron process involving a number of elementary steps and intermediates. Although two main routes have been identified, the exact mechanism is still not fully understood. The oxygen reduction reaction mechanism is most extensively studied on platinum. Norskov et al. showed through Density Functional Theory (DFT) modelling that among the pure metals, platinum seem to possess the closest-to-optimal binding strength with the oxygen molecule in order to carry out the reduction reaction [26]. In essence, they constructed a so-called “Volcano plot” describing the oxygen reduction activity for various metals as a function of oxygen binding energy, according to the Sabatier principle. Nevertheless, the catalyst needs to bind with an optimal energy not only to molecular oxygen but to all oxygen reduction intermediates as well in order to qualify as an optimal catalyst [27]. From studies of ORR on platinum, the general consensus seems to be that an end-on chemisorption mode of the oxygen molecule tends to favour the 2-electron reduction path to hydrogen peroxide. On the other hand, a bridge like chemisorption tends to increase the bond length in the oxygen molecule, thereby weakening the bond and hence facilitating the subsequent reduction steps following the 4-electron reduction pathway to water. The understanding of the oxygen reduction reaction has expanded substantially in the last years [15, 21, 27-29], however, the question still largely remains as to *why* platinum, among similar elements, exhibits such great electrocatalytic properties.

Although being the best alternative to date, ORR overpotential on the platinum cathode poses a major challenge in fuel cell technology [26]. Furthermore, platinum catalyst particles suffer from oxidation, dissolution and aggregation in the harsh operating conditions of the fuel cell [30, 31]. Moreover, platinum is a scarce noble metal and mined under challenging conditions. Its price is volatile not the least for geopolitical reasons. Recent technological advancements have pushed down the total platinum loading in commercial fuel cell cars to <10 g/car which is roughly the same amount platinum as in the catalytic converter in an internal combustion car [32]. Nevertheless, the cost contribution from the catalyst still amounts to approximately 30% of the total fuel cell cost and is hence formulated by fuel cell manufacturers as being of urgent concern [33].

1.3 Aim of this thesis

Finding efficient, durable and abundant oxygen reduction catalyst alternatives and to understand the origin of their catalytic activity remains as challenging as it is necessary, in order to reduce the amount of and eventually replace platinum as a catalyst in PEM fuel cells. Both these issues are being addressed in this thesis. The aim of this thesis is to describe how electrocatalyst particles with core-shell structure, using platinum as surface species, can be synthesized and how to reveal the true nature of such particles. Secondly, the effects on catalytic activity as a result of lattice modifications are investigated. Furthermore, we show that also the presence of an external magnetic field affects the electrochemical behaviour of platinum-based nanocatalysts. Finally, we delve into the origin of catalytic activity in non-noble metal catalysts.

1.3.1 Designing low-Pt content catalysts

As a first step towards complete elimination of platinum as a fuel cell catalyst, a significant reduction of the amount of platinum is sought for. Early on the alternative of alloying platinum with cheaper

metals, e.g. Cr, Mn, Co, Ni and V, was suggested [19, 34, 35]. An advantage of alloys compared to their pure metal analogues is that their composition can be varied to an almost infinite degree, consequently tuning the properties of the material. The alloys can be ordered, random, layered etc., containing two or more different elements [35, 36]. The properties of the neighbouring atoms in the alloy lattice will determine the interatomic distance and geometry, hence affect the adsorption behaviour of the reactant – the oxygen molecule in the case of ORR [37].

Special attention has been given to nanoparticles with a core-shell-like structure [15, 38, 39]. Such structures can be achieved through enriching one alloying species to the surface of the particles, by depositing it onto the particle surface or by displacing atoms from the outermost shell in favour for the new metal species. Examples from the literature suggest that mass-specific activities higher than that of pure platinum can be achieved. Adzic et al. show through their synthesis of carbon supported Pt-Au-shell Ni-core-particles that a mass-specific activity about 20 times higher than for pure platinum can be demonstrated [40]. Despite impressive activities, such multiple-step synthesis is complex and the final structure not trivial to verify.

Keeping in mind the complexity of many of these techniques it raises the question if these materials really provide a cost reduction considering the alternative of pure platinum nanoparticles? We describe how core-shell type particles can be made in a room-temperature, tuneable, scalable one-pot synthesis and how they can be characterized with commonly available analysis techniques.

1.3.2 Manipulating catalyst properties

Although the electrochemical properties of platinum earns it the top-most spot of the “volcano curve” amongst pure metals, as electrocatalyst for ORR Pt is still not optimal [41]. Alloying Pt with a number of other metals could theoretically bring the catalytic activity even higher than pure Pt, however, a serious problem is the harsh operating conditions in a fuel cell causing dissolution of most other metals. Hence, a covering layer of platinum serves as oxidative protection as well as being the active catalytic surface.

Interestingly, there are ways to access and manipulate the electrochemical properties of Pt. In this thesis we explore two routes aiming to understand and modify the electrochemical behaviour of Pt:

- ❖ *Manipulation of the lattice parameters of Pt.* This is achieved by making core-shell type particles with a number of different core materials as well as shell thicknesses and studying the response in electrocatalytic activity. The results are presented in Ch. 4.

- ❖ *Magnetic field effects on electrochemical behaviour of Pt.* Using magnetism as a steering tool for catalytic activity is an established concept, however much less explored in terms of electrocatalysis. The presence of a magnetic field brings about a change in the spin configuration of particles, as long as unpaired spin states prevail, which can influence the catalytic activity [42, 43]. Our study, exploring the effects of a magnetic field on the behaviour of Pt in a fuel cell cathode environment, is presented in Ch. 5.

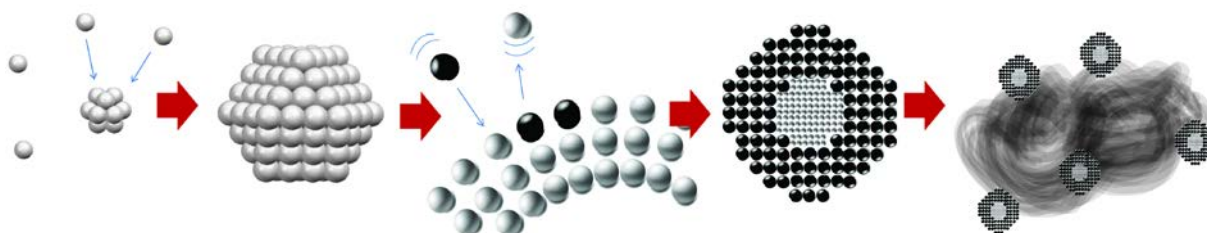
1.3.3 Organometallic catalysts

As for alternative materials to platinum, a lot of attention has been drawn to organic or metalorganic molecules – inherently cheap and abundant materials. By analogy to naturally occurring oxygen activation molecules, like the haeme-group in haemoglobin, it is believed that moieties consisting of transition metals coordinated in a Me-N₂ or Me-N₄ fashion exhibit catalytic activity towards oxygen reduction. However, it is not well understood what the role of the metal core in the structure is [13, 14, 44-47]. In case of the structures created from simple nitrogen-containing precursors it has been suggested that the metal helps creating the active centre. Nevertheless, in experiments continued by subsequent removal of the metal from the structure, a remaining activity indicates that the activity is not necessarily closely connected to the presence of a metal core in the final structure.

Materials like phthalocyanines and porphyrines have been potential candidates due to their relatively high stability in acidic conditions. Following on the discovery of graphene and carbon nanotubes, the possibility of introducing similar moieties into graphitic lattices was explored. Numerous reports show how electrocatalytic properties can be achieved upon introducing nitrogen as a heteroatom – with or without a transition metal core – into the graphitic structure [13, 14, 21, 25, 48, 49]. Despite showing stability in acidic aqueous solutions, the harsh conditions in a PEM fuel cell still provides a major challenge [50]. Moreover, the synthesis of such materials often involves high temperature treatment that alters the original structure of the material with a rather random inclusion of the nitrogen as a result [51, 52]. This leaves the exact nature of the active site in obscurity [50, 51]. There is a general lack of understanding and consensus about the catalytic mechanism of these materials as well as how the activity and stability can be tailored.

In order to achieve significant progress in the area of non-noble ORR catalysts it is of crucial importance to understand how the molecular structure of a material influences its catalytic properties. In Ch. 6 of this thesis we discuss the latest progress in the world-wide race of unravelling the true nature of catalyst active centres and the origin of catalytic activity in non-noble metal catalysts.

2 Synthesis of core-shell particles in bi-continuous micro-emulsion



2.1 Abstract

The use of (bi-continuous) micro-emulsions as nano-reactors for particle synthesis allows the high yield production of monodispersed nanoparticles through a simple room temperature procedure. Here, we demonstrate how bimetallic core-shell type catalyst particles can be efficiently tailor-made using such micro-emulsion systems. Various routes all involving micro-emulsion routes for synthesizing core-shell nanoparticles were investigated in order to find a suitable synthesis procedure. With the core material, typically Fe, Ni or Cu, we first produce particles of diameter 3 ± 0.6 nm. The shell – Pt or Ag – is subsequently added through galvanic displacement in which the outer-most core layer(s) is exchanged in favour of platinum. The final catalysts were characterized by SEM, TEM, DLS, ICP-AES, XRD, CV, HV, SQUID and XPS to obtain data on particle size, monodispersity, composition, surface species, surface area, oxidation state etc. Using a transition metal as core material not only reduces the amount of precious metal in the particles but also offers a number of additional benefits. Apart from a magnetic core facilitating the separation and administration of catalyst particles (Duan et al., *Materials International*, 2013) the electronic configuration and lattice structure of the core metal influences the properties of the shell metal, as studied in depth in Chapter 4.

2.2 Introduction

Despite a number of degradation issues [20], platinum has long been considered the best oxygen reduction catalyst at low pH amongst the pure metals, commonly demonstrated by Volcano-type plots [26] semi-logarithmically displaying catalytic activity versus intermediate binding affinity. It is worth noting that the oxygen reduction is a multiple step reaction with specific binding energies between the substrate and oxygen reduction intermediates for every step throughout the 4-electron reduction, for which the exact reaction path is still being discussed [27, 53]. Pt(111) comes close to an “optimal” binding energy for one of the proposed intermediates, namely Pt-O, but could nevertheless not be entitled the ideal catalyst simply because the other binding energies are less optimal.

An interesting catalyst material equivalent for oxygen reduction in alkaline conditions is silver, due to its high abundance and catalytic properties. Apart from its potential in alkaline fuel cell (AFC) catalysis, its applicability extends to other electrochemical reactions as CO₂ reduction and water purifications.

Striving to improve the catalysis of Platinum and Silver tremendous efforts have been made in alloying them with a variety of cheaper metals, like Cr, Mn, Co, Ni, V, Ti or adapt the core-shell principle in which a thin layer – even monolayer – of platinum is coated on a cheaper bulk metal [19]. Such materials must not only meet the requirements of possessing high catalytic activity, oxidative stability etc., but also be produced in a cheap, facile way resulting in well-defined, monodispersed catalyst particles. It is of utmost importance to understand the catalytic properties behind these materials as they are likely to continue to play a key role in catalysis.

The use of core-shell particles as catalyst entails a number of benefits. Firstly, it opens up the possibility to assess the properties of individual layers as well as to manipulate their structure. Secondly, core-shell particles as opposed to pure particles offer a more efficient material usage. Finally, it offers opportunities to use the core material properties for manipulation and handling of the particles [54]. Synthesizing such particles in a micro-emulsion matrix provides a relatively simple, low-temperature pathway to highly monodispersed particles.

Micro-emulsions basically consist of a hydrophilic phase and a hydrophobic phase stabilized by surfactants, which composition and hence structure can be varied and graphically visualized in a ternary phase diagram [55]. Nanoparticles can be synthesized by mixing two micro-emulsions; one containing the metal precursor and the other containing the reducing agent. One major advantage of synthesizing nanoparticles inside the channel junctions made up by surfactants in a micro-emulsion, arises from the prevention of aggregation of the particles, keeping the particles uniformly sized at a scale of only a few nanometres. Further, the synthesis in micro-emulsions takes place at room temperature, providing a cheap and easy alternative to conventional synthesis methods [36, 56, 57]. Using a surfactant:oil:water ratio that takes a bi-continuous shape implies a high yield of particles relative to the total weight of the emulsion [58].

There are a number of ways to obtain core-shell structured nanoparticles. The two metals can be introduced simultaneously in the reduction process and being subsequently segregated through reduction environment. Other routes for adding shells to already existing cores can involve a second reduction step comprising of a fresh addition of reducing agent and metal ion solution to the core particles. Yet another technique takes advantage of different reduction potentials between the core

and shell metal. In galvanic replacement a redox reaction between the core and precursor shell ions, takes place without any additional reducing agent. It is only suitable if the shell has a higher thermodynamic equilibrium potential than the core. Also, the size of the core will be reduced by the shell metal ions.

The possibility of using micro-emulsions to create *bimetallic* and *core-shell* structures is described in this chapter, tailoring the micro-emulsion composition, reaction conditions and precursors. Core-shell synthesis through galvanic replacement has also been previously described in literature but this work adds the use of galvanic replacement in a micro-emulsion synthesis [59, 60].

2.3 Materials and Methods

2.3.1 Chemicals

Surfactant "AOT" or sodium bis(2-ethylhexyl) sulphosuccinate ($C_{20}H_{37}NaO_7S$, 98%), heptane (C_7H_{14} , $\geq 99.9\%$), chloroplatinic acid hydrate ($H_2PtCl_6 \cdot 6H_2O$, $\geq 99.9\%$), iron (III) chloride hexahydrate ($FeCl_3 \cdot 6H_2O$, $\geq 97\%$), copper chloride ($CuCl_2$, $\geq 99.9\%$), nickel chloride ($NiCl_2$, $\geq 98\%$), sodium borohydride ($NaBH_4$, $\geq 99\%$), tetrahydrofuran (THF $\geq 99.9\%$), hydrochloric acid (HCl, 37%), silver nitrate ($AgNO_3$, 99.9999%), iron (II) sulphate heptahydrate ($FeSO_4 \cdot 7H_2O$, $\geq 97\%$), Triton-X100 ($t\text{-Oct-C}_6\text{H}_4\text{-(OCH}_2\text{CH}_2)_x\text{OH}$, $x=9\text{-}10$) all used as received from Sigma Aldrich. Nafion solution (5 wt % ; 250 ml) and carbon black powder (Vulcan XC-72R) were used as received from Quintech and FuelCellStore (College Station, TX, USA) respectively. For all sample preparations, reagent-grade water produced by a Milli-Q ultrapure purification system from Millipore BV was used. MicroPolish Alumina Suspension (grades 1,0, 0,3 and 0,05 μm) purchased from Buehler (Lake Bluff, IL, USA) was used to polish the glassy carbon.

2.3.2 Micro-emulsion preparation

A method of producing platinum particles in bi-continuous micro-emulsions (BME) was developed in our group [58, 61, 62]. For the synthesis of core-shell particles in bi-continuous micro-emulsion the procedure of synthesizing pure platinum particles described in their work was adapted to produce a variety of core metals and extended with a final, galvanic displacement step after synthesizing transition metal core nanoparticles, see Fig 2.

In essence a micro-emulsion consists of three phases; surfactant, oil and water. At low water content, the micro-emulsion consists of water-filled micelles in oil. At higher water content, the micelles are inverted containing oil in water. An intermediate situation exists in between these two extremes in which the system consists of alternating oil/surfactant/water layers, tubes or interconnected channels as illustrated in Fig 1, the latter phase being called bi-continuous since both the aqueous phase and the oil phase are continuous and form intertwined channels [62].

Two types of micro-emulsions were used; AOT/Heptane/Water as well as emulsions based on Triton-X/Toluene/Water. In both cases a surfactant:oil:water ratio corresponding to the bi-continuous phase. For the AOT system a bi-continuous micro-emulsion was prepared by mixing 56 wt% Na-AOT, 20 wt% milli-Q water and 24 wt% heptane [58], in which the water phase was added after having dissolved all surfactant in the oil phase. Corresponding ratios for the Triton-X system was 55 wt% Triton-X, 20 wt% water and 25 wt% toluene. The solution went from being rather turbid to clear as

the emulsion was formed, requiring about an hour. All syntheses were carried out at room temperature and at atmospheric pressure.

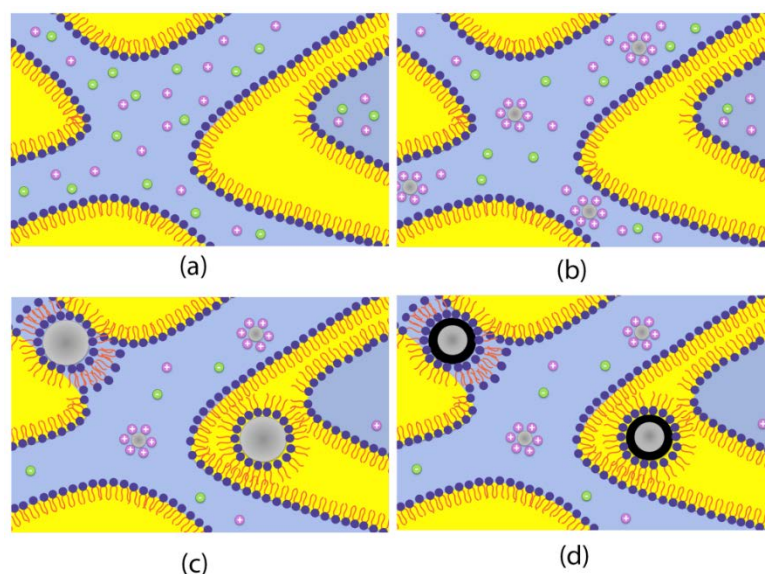


Fig 1 Schematic picture of core particle formation (a)–(c) and subsequent galvanic displacement to form final core-shell particles (d). Figure adapted with permission from original in [58].

2.3.3 Synthesis of transition metal cores

The synthesis of transition metal cores was achieved by reduction of a transition metal salt by sodium borohydride in the aqueous phase of a bi-continuous micro-emulsion. One micro-emulsion, in which the transition metal precursor was dissolved in the water phase, was mixed with a second micro-emulsion containing reducing agent, resulting in the formation of metallic nanoparticles, their size being controlled by the size of the water channels in the emulsion. Cores with four different types of metals were synthesized; Fe, Ni, Cu and Co. Each micro-emulsion weighed 30 g (16.8 g AOT, 7.2 g heptane and 6 g water), in which 0.15 M of metal salt or maximum 0.75 M NaBH_4 was dissolved in the water phase. The reducing agent and the metal precursor were mixed with 3-5 times excess of reducing agent, the lower ratio (3) being used for the Cu and Ni based cores.

2.3.4 Galvanic replacement

After completion of the reduction process of the core, a third micro-emulsion containing shell metal salt precursor (0.1 M dissolved in the water phase of a 30 g micro-emulsion) is added slowly to the core emulsion. The subsequent galvanic replacement is left to proceed for at least 2 hours after which addition of 60 wt% carbon support (assuming 80% conversion of the core metal) under sonication follows. The particles are allowed to adsorb on the carbon surface during at least 8 hours. Subsequently a washing procedure of 6 steps follows. Washing is intended to remove heptane/toluene and surfactant from the particles. In the acid washing step any uncoated core metal and core-shell particles that have not adsorbed on the carbon support are washed away.

In the first two washing steps THF is added dropwise to the dispersion during stirring followed by ultra-sonication for 10 min to remove the surfactant from the particle surface and centrifugation at 6000 rpm for 10 min. In step 3-4 the particles are washed with 50 ml 1 M HCl in order to dissolve any

uncoated core particles. More than two acid washing steps have proven not to remove more (core)material from the sample. In the last two steps the particles are washed with 50 ml Milli-Q water and centrifuged. The powder is left to dry at 60 °C for 12 h.

Two other methods proving not to produce core-shell particles were:

- *Sequential formation*: With this procedure the shell is formed without sacrificing core material but rather through the addition of separate reducing agent. The idea here is that the core will offer nucleation sites for the shell metal atoms to nucleate and grow.
- *Galvanic replacement without shell metal micro-emulsion*: The core was prepared in a micro-emulsion and subsequently adsorbed to a carbon support. After adsorption had been allowed to take place an aqueous solution of Pt-salt was added.

In the case of sequential formation, separate core and shell-material pure particles were formed and the final product contained exclusively platinum particles since iron particles were dissolved in the acid washing step. When using the procedure in which the carbon was added straight after core synthesis with later addition of aqueous Pt, no particles at all were detected in subsequent material characterization.

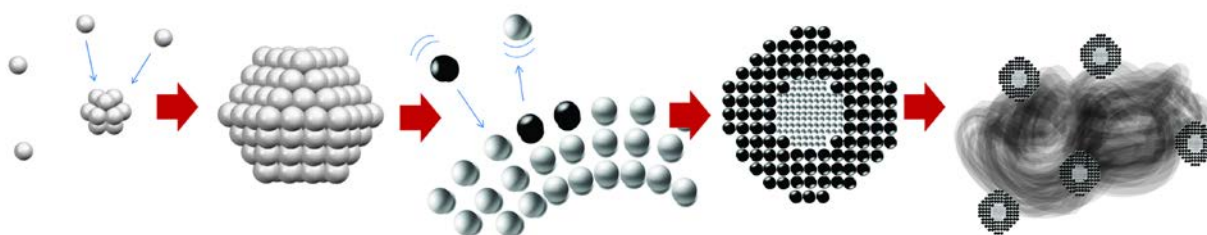


Fig 2 Illustration of particle synthesis involving galvanic replacement and particle adsorption on carbon support

2.3.5 Synthesis of pure Pt and Ag reference particles

Samples with pure Pt as well as Ag particles on carbon were made similarly to the core-shell particles but using Platinum and Silver as core metal and skipping the step of galvanic replacement. Analogous to the core-shell particles the pure Pt and Ag particles were supported on carbon and washed in six steps including acid washing.

2.3.6 Nanoparticle characterization

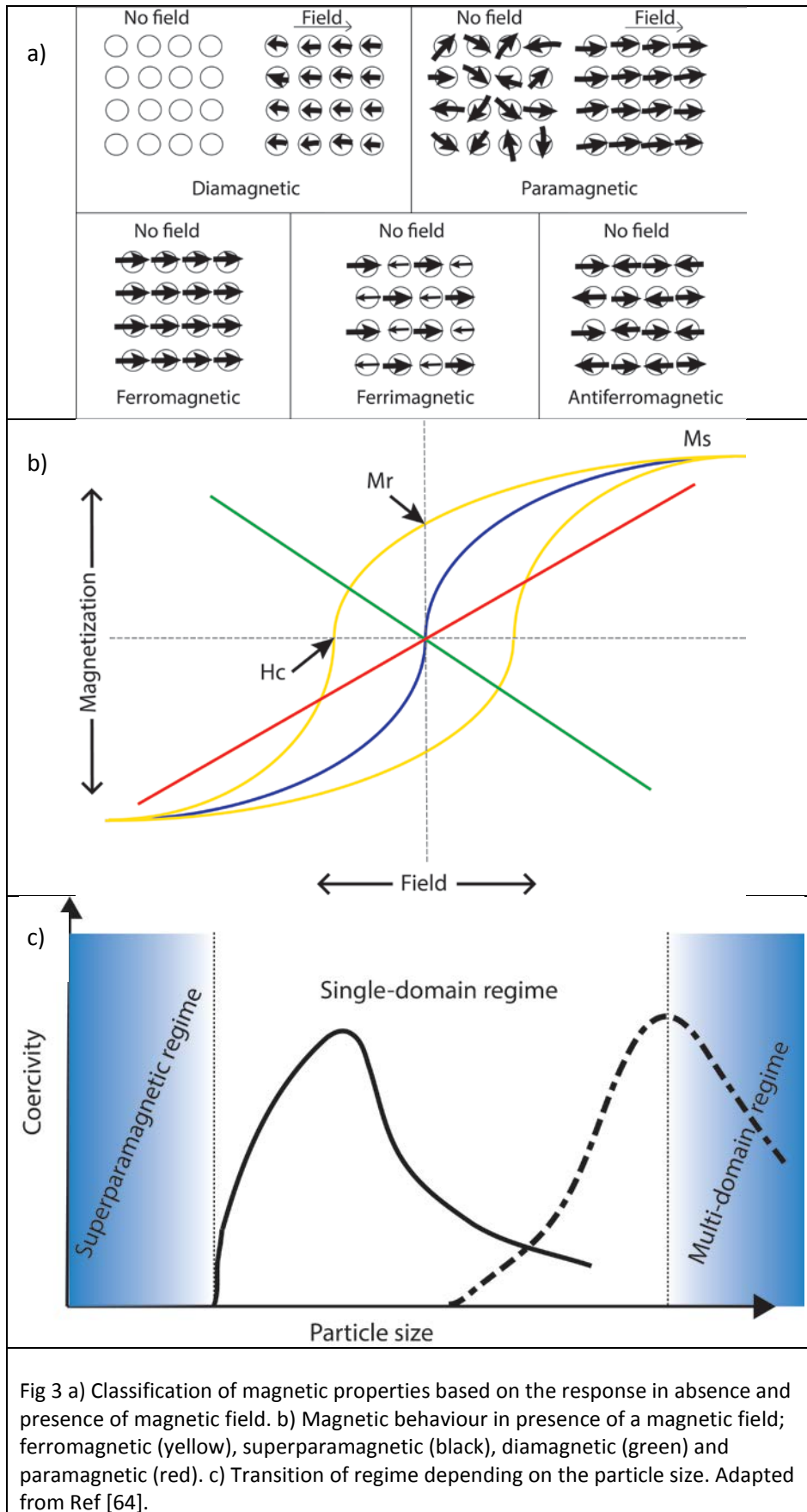
A Bruker AXS D8 Discover instrument was used for powder X-ray diffraction (XRD) using a copper $K\alpha$ radiation of wavelength 1.54 Å. Samples were placed on a silicon wafer during measurements. A JEOL JSM-6010LA InTouchScope was used for Scanning Electron Microscopy (SEM) analysis and Energy-Dispersive X-ray Spectroscopy (EDX). Samples were fixed on carbon tape when measured. EDX analyses were also carried out during Transmission Electron Microscopy (TEM) measurements using a JEOL JSM 2012. Samples were crushed in ethanol and drop-casted onto a copper grid. Dynamic Light Scattering (DLS) was used to analyse particle size distributions, using a Malvern Zetasizer Nano ZS. Samples – before the addition of carbon support – were firstly diluted 20 times in heptane and sonicated for at least one hour before the analysis, in order to break up the micro-emulsion aggregates. It is important to note that the particles at this stage are not washed implying that the hydrodynamic radius observed includes the length of surfactant particles.

For elemental analysis using Inductively Coupled Plasma - Atomic Emission Spectroscopy (ICP-AES) an ICP Optical Emission Spectrometer PerkinElmer Optima 5300DV was used. The samples analysed were liquid samples, dissolved in aqua regia in a microwave. Surface analysis was performed by X-Ray Photoelectron Spectroscopy (XPS) using a Kratos axis Ultra DLD Photoelectron spectrometer, equipped with an Al Ka X-ray source.

For all electrochemical measurements, an Autolab PGSTAT 20 potentiostat was used, along with a 3-electrode cell and a Rotating Disc Electrode (RDE) from Pine Instruments with a 5 mm in diameter glassy carbon disk and hence an electrode area of 0.198 cm^2 . The working electrode were prepared by thoroughly polishing the glassy carbon disk with 1.0, 0.3 and $0.05 \mu\text{m}$ alumina particle polishing suspensions, rinsing in between each step. Any residual polishing medium was cleaned off in an ultrasonic bath. An ink was made by mixing 6.0 mg of catalyst powder (i.e. carbon + core-shell particles) with $4.56 \mu\text{l}$ Nafion suspension (5wt%) and 12 ml isopropanol. The ink was mixed using an ultrasonic bath. To make the catalyst ink layers on the electrode $13 \mu\text{l}$ of catalyst ink was drop casted on the disk. All experiments were conducted in an electrolyte saturated with Ar for the cyclic voltammetry and O_2 for the hydrodynamic voltammetry using rotation speeds of 400, 900, 1600 and 2500 rpm. Scan speed for CV was 50 mV and 5mV for HV. In a first electrochemical cleaning step, potential cycling at a speed of 100mV/s for 50 cycles was used.

For Pt@Me the activity measurements were carried out under acidic conditions according to a standardized RDE procedure [63]. The electrolyte used was a 0.1 M HClO_4 solution. The reference electrode was a RHE electrode – in essence a Pt wire with freshly prepared H_2 gas - and the counter electrode was a platinum wire wound into a spiral shape. For Ag@Me the activity measurements were carried out in alkaline conditions. The electrolyte used was 0.1 M KOH and the reference electrode was in this case an Ag/AgCl electrode (0.23 V vs SHE).

A Superconducting Quantum Interference Device (SQUID) MPMS XL magnetometer from Quantum Design was used to characterize the magnetic behaviour of the core-shell particles. Based on the response of the intrinsic magnetic dipole and the net magnetization in the presence and absence of an applied magnetic field, particles are typically classified as being either diamagnetic, paramagnetic, ferromagnetic, ferrimagnetic, and antiferromagnetic, see Fig 3a. The magnetic behaviour of nanoparticles is further governed by many factors, including size, shape, composition and core-shell structure [64]. By studying the magnetization as a function of applied magnetic field, the saturation magnetization, M_s , i.e. maximum magnetization possible can be estimated, as well as remanent magnetization, M_r , corresponding to the induced magnetization remaining after the external field is removed, see Fig 3b. Furthermore, the coercivity, H_c , i.e. the intensity of a field required to force the magnetization back to zero, can be extracted from such measurement.



Reducing the size of a magnetic particle to values smaller than the thickness of a domain wall will yield a single-domain particle. Among magnetic properties, the saturation magnetization, M_s , is independent of specimen size, at least until the number of atoms on the surface becomes significant compared to the total number of atoms in the sample volume. As the size of magnetic particles is reduced to the nanometre scale, the coercivity increases because of the transition from multi- to single-magnetic domains. When forming a single domain, the coercivity reaches a maximum value and begins to decrease with further size reduction due to the depletion of the number of magnetic spins. As the size of the nanoparticle decreases, the magnetic anisotropy energy per nanoparticle decreases. At a characteristic size for each type of nanoparticle the anisotropy energy equals the thermal energy, allowing random flipping of the magnetic moment. At this characteristic size the nanoparticle is defined as being superparamagnetic. The different regimes are displayed in Fig 3c.

2.4 Results for Pt@Me

2.4.1 Synthesis

Upon mixing of the micro-emulsions containing reducing agent and core precursor, most of the metal core nanoparticles are formed within minutes, and the reaction is complete after 2 h. Leaving the reaction to proceed longer than 2 h does not result in a considerably higher yield of core particles. The ratio Pt:Me, where Me stands for the core metal used, in the final catalyst could be varied by the concentrations of the precursors. Also for the minimum time required for the shell to form in the galvanisation step was approximately 2 h. Leaving the core particles in the Platinum ion rich solution did not yield pure Pt particles even for an extended amount of time. Considering the time scales for (1) primary particle formation, (2) shell formation through galvanic replacement and (3) adsorption of particles onto carbon support, the latter is the slowest process. The adsorption time needed was approximately 8 hours. Thus, initiating the washing procedure too soon after the carbon support is added results in very low contents since formed particles simply are washed away. The adsorption of Pt on the carbon is indeed expected to be the time limiting step since the surfactant present competes in adsorbing and may slow down the adsorption of Pt onto carbon. Nevertheless, experiments also show that the surfactants can function as anchors between the particles and the carbon support hindering agglomeration. For ratios smaller than Pt:Me 1:2 (at) for a particle size of 3 nm the Pt content is too low in order to form a continuous shell. Hence the smallest fraction of Platinum used here is Pt:Me 1:1.

For all Pt@Me particles – where Me=Fe, Ni, Cu and Co – AOT/heptane/water emulsions were used. Additionally the Triton-X/toluene/water emulsion system was used for exploring the possibility to produce Pt@Fe core-shell particles as a sulphur-free alternative synthesis route. Pt@Fe particles could successfully be synthesized in the Triton-X system but considering that the final yield of Pt@Fe particles was only 20% of the yield using AOT, the route was not further exploited.

Furthermore, newly formed Ni and Cu cores seem sensitive to high concentrations of NaBH_4 . If the core syntheses for these metals are carried out with more than 4 times excess of reducing agent, the core particles – still in micro-emulsion – would dissolve/disintegrate in less than one hour. On the contrary, Ni and Cu particles synthesized using lower ratios of reducing agent, along with Fe and Co core particles, remained stable for more than 24 h.

Once suitable concentrations, ratios and synthesis step times as described above was established, batches of particles could be synthesized with size and composition differences in the same range as the measurement errors of the characterization techniques used. Particles synthesized with this procedure has been used throughout this thesis.

2.4.2 Characterization

Size measurements based on DLS confirm a narrow size distribution and no significant size change between core and core-shell particles, both being 3 ± 0.6 nm, in agreement with TEM measurements, see Table 1 and Fig. 4 and Fig. 5 for an example.

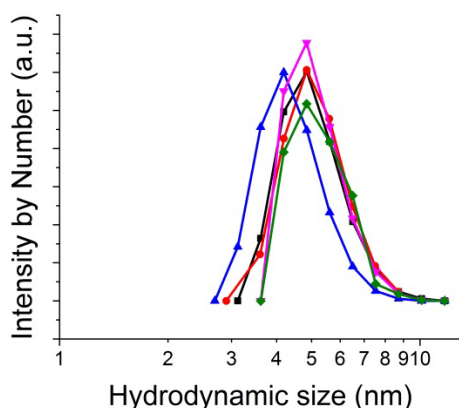


Fig 4 DLS measurements of Pt@Cu (black), Pt@Fe (red), Pt@Ni (blue), Pt@Co (green) and pure Pt (pink) made in a bi-continuous micro-emulsion. Note that the hydrodynamic particle size here includes the surfactant length (0.8 nm for AOT). (The lines are guides to the eye)

An estimate of the final composition of the particles was obtained using SEM-EDX and ICP-AES, a summary is presented in table 1. These results confirm the presence of both metals in the final catalyst after extensive (acid) washing. TEM micrographs further demonstrate a spherical shape of the particles. Agglomeration of the particles could be identified for samples washed with acid. Due to the small size of the particles and the resolution of the TEM no difference in contrast between core and shell could be spotted. In the elemental analysis by SEM-EDX in Fig 6, it is observed that the two metals in each core-shell sample are well dispersed over the carbon support.

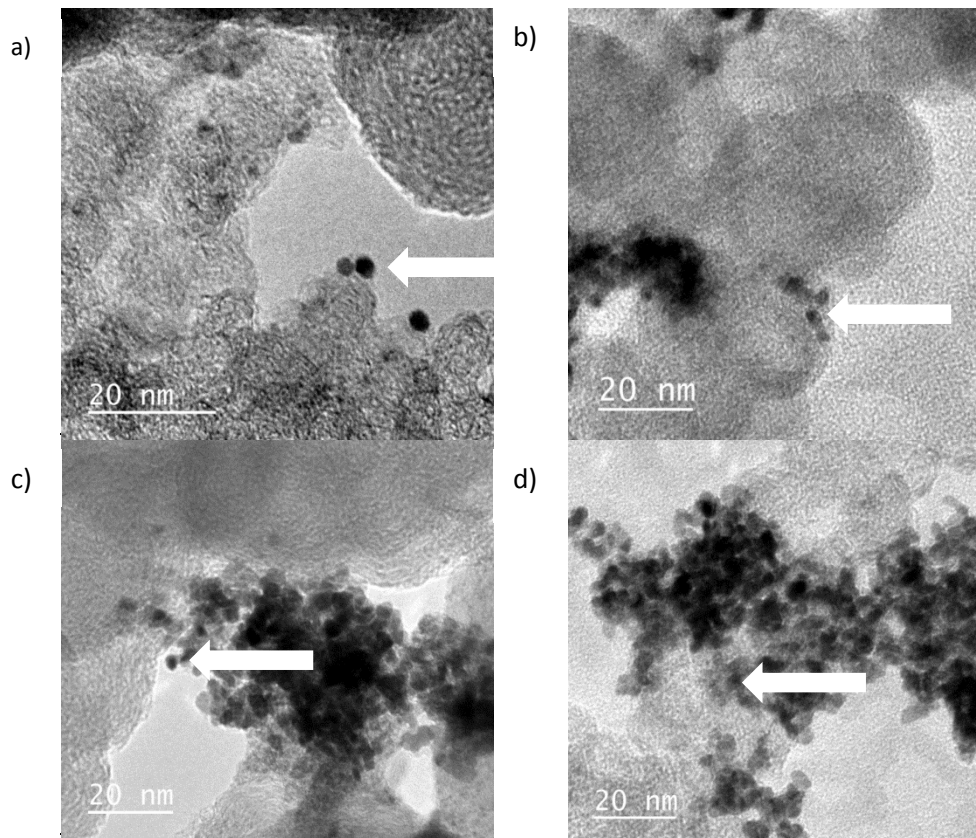
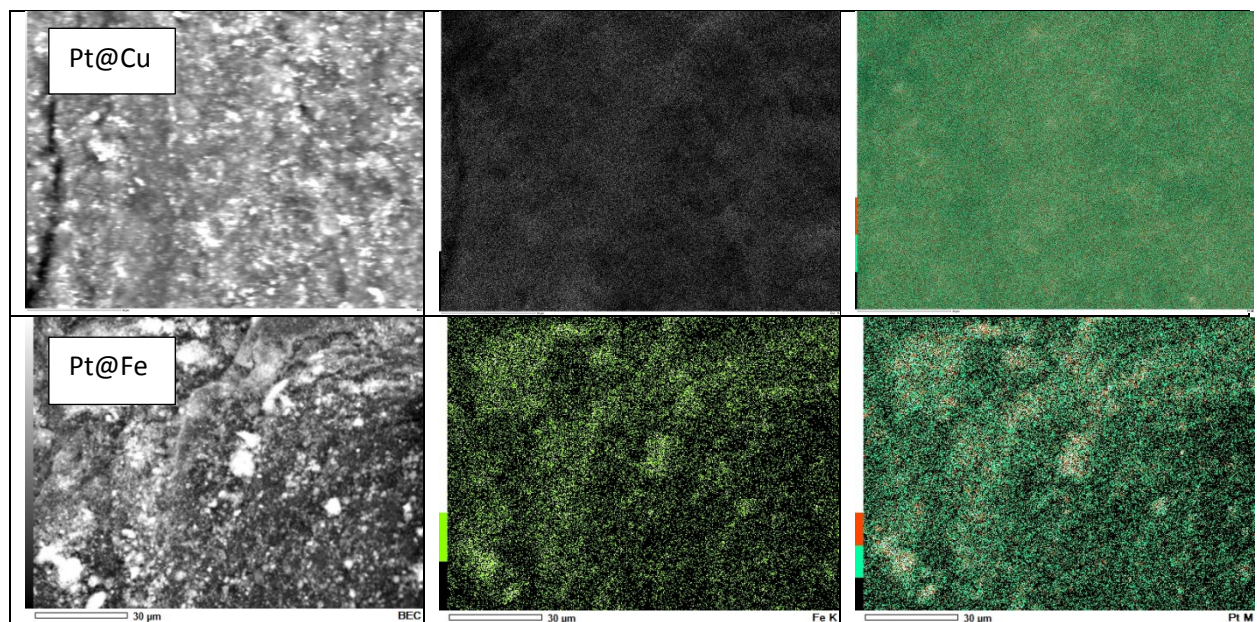


Fig 5 TEM pictures of (a) Pt@Cu, (b) Pt@Co, (c) Pt@Ni and (d) Pt@Fe particles supported by high surface area carbon (Vulcan XC72). The white arrows indicate the locations of the spherical particles and the surrounding grey structure is the carbon.



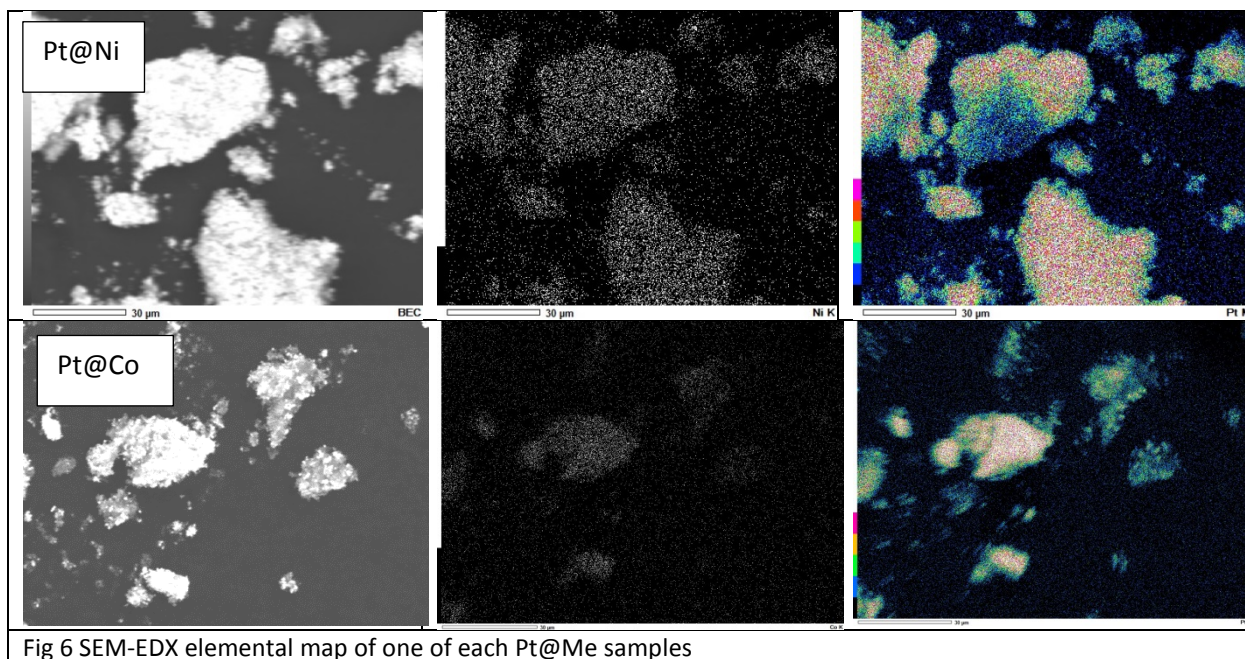


Fig 6 SEM-EDX elemental map of one of each Pt@Me samples

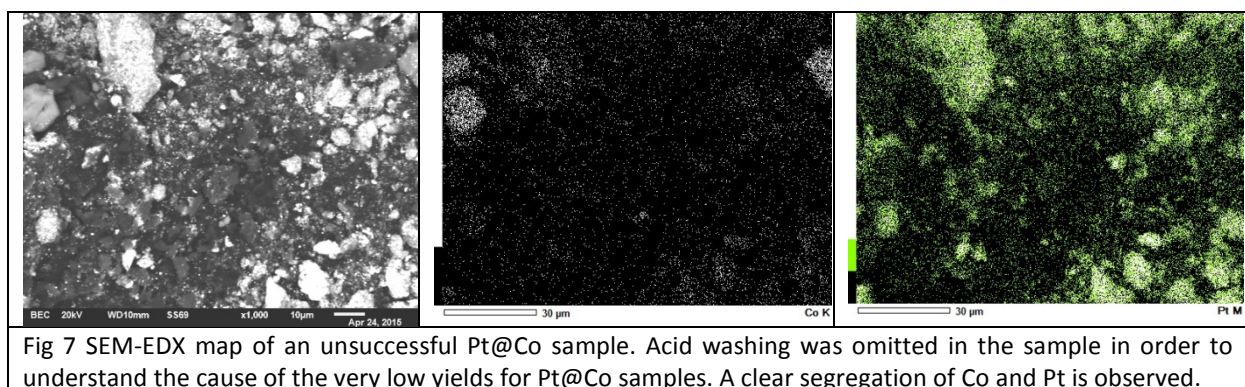


Fig 7 SEM-EDX map of an unsuccessful Pt@Co sample. Acid washing was omitted in the sample in order to understand the cause of the very low yields for Pt@Co samples. A clear segregation of Co and Pt is observed.

Interestingly, all syntheses of Pt@Co particles yielded very low amounts of core-shell particle, corresponding to a conversion of <5 % rather than approximately 60-80% that was typically achieved for the other metals. Only one synthesis of Pt@Co generated a sample with particle amounts high enough to even do a full characterization. In Table 1 the final sample composition of this sample is presented. To investigate possible causes of this low yield, a Pt@Co sample for which the washing step had been omitted, was analysed with EDX. In Fig 7 the results suggest that Co and Pt are, to a certain extent, not evenly distributed over the sample. If Co particles are not covered by Pt in the galvanic displacement step, the Co will be lost in the washing procedure. Simultaneously, the yield of Pt will be low since reduction of Pt depends exclusively on the oxidation of Co and no additional reducing agent will keep the Pt yield high.

Table 1 Results table for one of each sets of particle types (*this sample is also the *only* sample of Pt@Co)

Sample	Atomic ratio Pt:Me	Composition wt% (C:Pt:Me)	Particle size, d
Pt@Ni	2:1	72:25:3	2.7 ± 0.6 nm
Pt@Fe	5:1	58:41:1	3.2 ± 0.6 nm
Pt@Cu	2:1	54:41:5	3.2 ± 0.6 nm
Pt@Co*	5:1	94:5:1	3.2 ± 0.7 nm
Pt commercial	-	0:60:40	
Pt BME	-	0:40:60	3.2 ± 0.6 nm

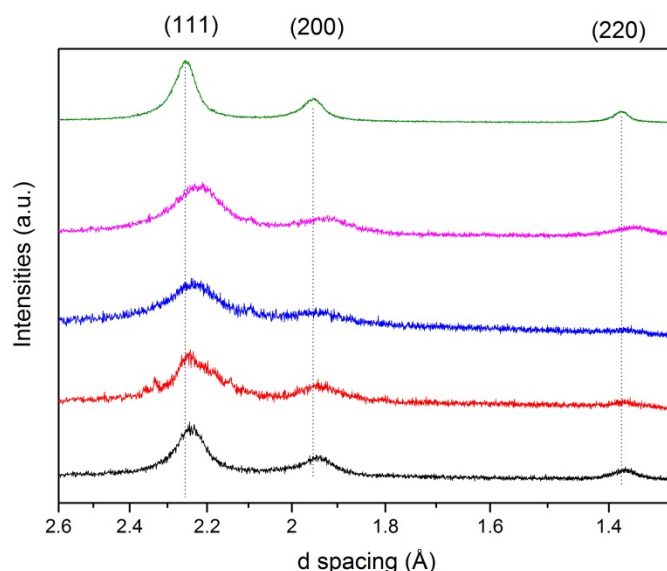


Figure 8 XRD result example of Pt@Cu (pink), Pt@Fe (blue), Pt@Ni (red), Pt@Co (black) as well as pure Pt (green). The lines indicate the peak position for pure micro-emulsion made Pt nanoparticles and are intended as a guide to the eye. The shift will be discussed in Chapter 4.

Figure 8 presents some XRD spectra from every sample type. In general Pt reflections are observed in all samples. The shift of the peak position in core-shell samples relative to pure Pt will be discussed in Chapter 4. As also discussed in Chapter 4, reflections corresponding to the core metals are not detected.

The XPS spectra for Pt@Fe particles showing the relative composition of metallic and oxidized species for the Pt shell as well as the Fe core. The Pt shell consisting of only a few layers of Pt allow signal penetrating also from the underlying Fe, as seen in Fig 9. The found peak positions for Pt corresponds to the binding energies of Pt4f at 72.0 eV and 75.0 eV as compared to literature values of 71.3 eV and 74.8 respectively [38]. The slight shift to higher binding energies can be attributed to the influence of the core. For the 2p binding energies for Fe, peak positions identified correspond to a contributions from the three oxidations states of Fe; Fe⁰ at 706.7 eV, Fe²⁺ at 709.6 eV and Fe³⁺ at 710.8 eV for the Fe2p_{3/2}. Fe2p_{1/3} peaks correspond to 720.3 eV, 723.4 eV and 725.0 eV respectively. The results indicate that the Fe core is likely to consist of partly oxidized iron, possibly in the arrangement of a core-shell-shell in which there exists a Fe⁰-rich and a FeO-rich phase.

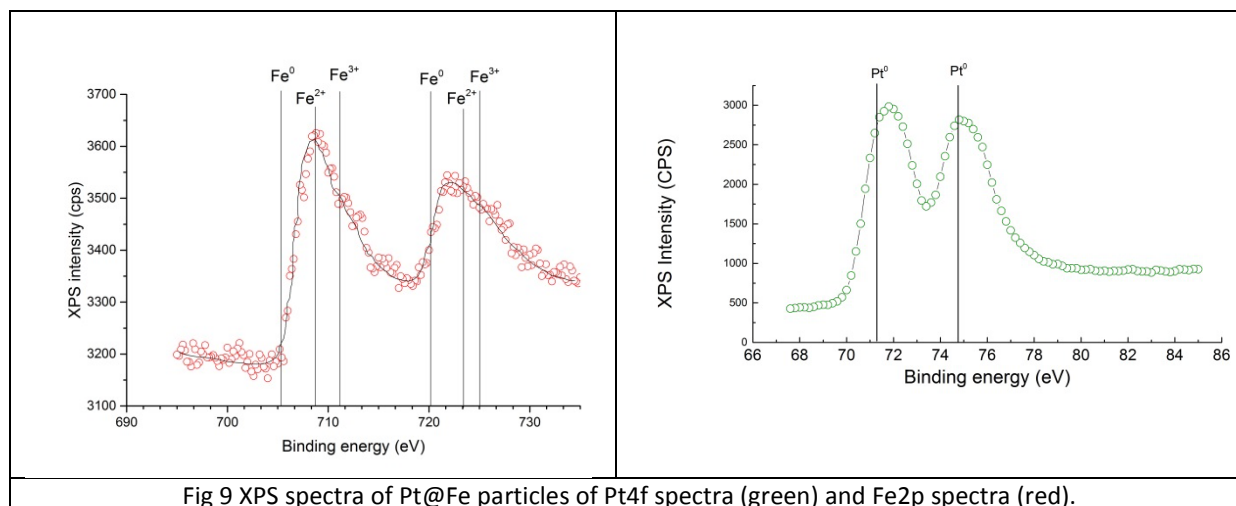


Fig 9 XPS spectra of Pt@Fe particles of Pt4f spectra (green) and Fe2p spectra (red).

From the multiple-cycle voltammograms performed in deaerated electrolyte, information can be extracted about the surface dominating species and whether it is completely covering the core. In the event that some particles with an uncovered core would have persisted after the acid washing, they would leach out upon atom rearrangements driven by the potential cycling. For at least 100 cycles no significant persisting change in the voltammograms was observed for any of the presented samples, i.e. for shell to core atomic ratios above 1:2. Moreover, changes seen in the first few cycles, usually ascribed as being surface cleaning or even surfactant removal, are not different from pure Pt samples [24]. The cyclic voltammetry data for the core-shell samples show typical characteristics of Pt, including hydrogen adsorption and desorption, as presented in Fig 10.

The electrochemical surface area (ECSA) calculated based on the hydrogen adsorption and desorption peak areas are similar between core-shell samples and slightly lower than for commercial Pt, as presented in Fig 10. This is to be expected since the thorough washing procedure as a part of the core-shell synthesis, cause some agglomeration. The commercial Pt is more optimally distributed on the carbon support. Moreover, ECSA calculations are based on a number of assumptions not taking into account any lattice structure modifications of the Pt shells due to the core-shell structure. Still mass activities of the core-shell particles are comparable to, or better than, that of pure Pt particles, as presented in table 2.

Table 2 Mass activity results from hydrodynamic voltammetry in oxygen saturated electrolyte at 900 rpm

	Pt@Fe	Pt@Ni	Pt@Cu	Pt BME
j (mA/mg Pt)	221	121	141	150

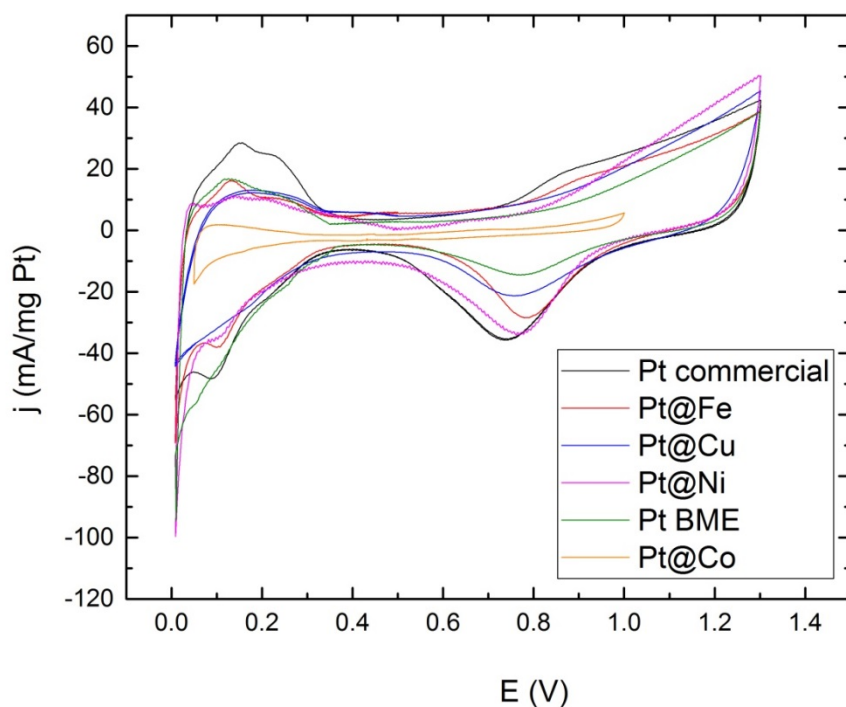


Fig 10 Cyclic voltammograms in Ar-saturated HClO_4 for Pt@Co (orange) Pt@Fe (red), Pt@Cu (blue), Pt@Ni (pink), pure Pt made in micro-emulsion (green) and commercial Pt (black)

The changes in magnetization with applied field was analysed using SQUID for three samples – Pt@Fe, Pt@Ni and Pt@Co. Magnetization was measured as a function of applied field from -5 to +5 T at 5K. Results are presented in Fig 11 and table 3.

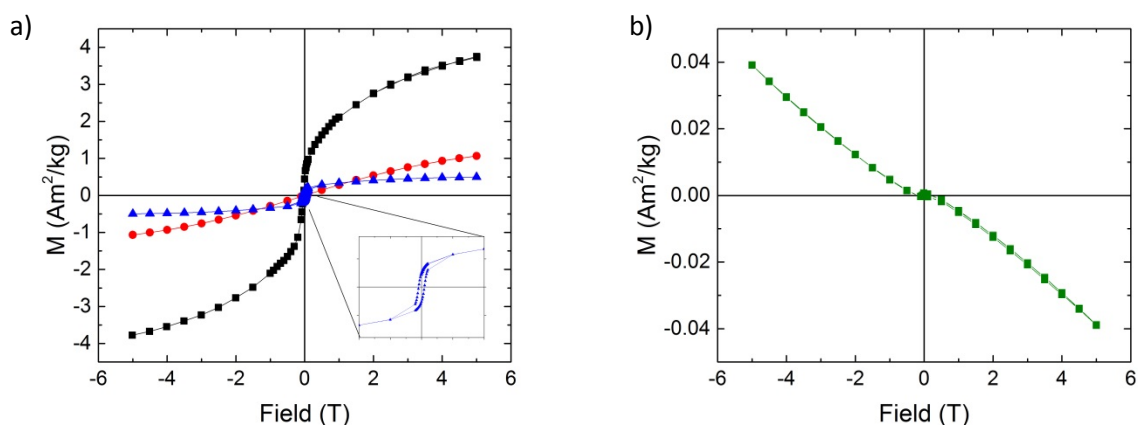


Fig 11 Magnetization as a function of magnetic field at 5 K for a) Pt@Fe (black), Pt@Ni (red) and Pt@Co (blue) b) Pt made in micro-emulsion (green)

Table 3 Magnetic behaviour of core-shell particles as well as a pure Pt sample made in bi-continuous micro-emulsion. Two literature values are also presented for comparison.

Sample	Magnetic behaviour	Estimated M_s (Am^2/kg)
Pt@Fe	superparamagnetic	3.7
Pt@Ni	superparamagnetic	1.1
Pt@Co	ferromagnetic	0.5
Pt BME	diamagnetic	
Bulk α -Fe [65]	ferromagnetic	222
Fe NP sized 7 nm [66]	superparamagnetic	67

If a Fe_2O_3 or FeO phase is present in the Pt@Fe particles, this might further contribute to a decrease in saturation magnetization relative to pure Fe [67]. Further, M_s depends on particle size and, since the core is expected to contribute the most to this property, the small size of the core contributes greatly to the low saturation magnetization.

Figure 11b shows diamagnetic behaviour in the pure Pt particles. This behaviour has been previously reported for clusters of Pt nanoparticles [65]. The magnetization behaviour of CoPt in Fig. 11a displays a hysteresis loop, indicating ferromagnetic behaviour. All other Pt@Me particles show superparamagnetic behaviour.

2.5 Results for Ag@Me

2.5.1 Synthesis

Upon addition of the transparent aqueous solution of AgNO_3 into the oil/surfactant solution a spontaneous reduction process started immediately even before addition of reducing agent, giving the emulsion a progressively more orange colour with time, as presented in Fig 12. DLS measurements suggest that the Ag-seeds formed are smaller than the 2 nm lower detection limit.

Possible causes of this phenomenon have been previously discussed [68-71], including options like the possible impurities in the surfactant, reduction by hydroperoxides formed from the Triton X-100 polyether chains and the photo-reduction of the silver-ions in presence of UV-light. For this reason both an AOT-based and Triton X-based micro-emulsion were used as particle synthesis scaffold. Moreover, the synthesis was also carried out both in absence and presence of light.

When performing the synthesis in presence and absence of light, no difference is observed neither in the speed of coloration of the emulsion nor the colour. This holds for both micro-emulsion systems.

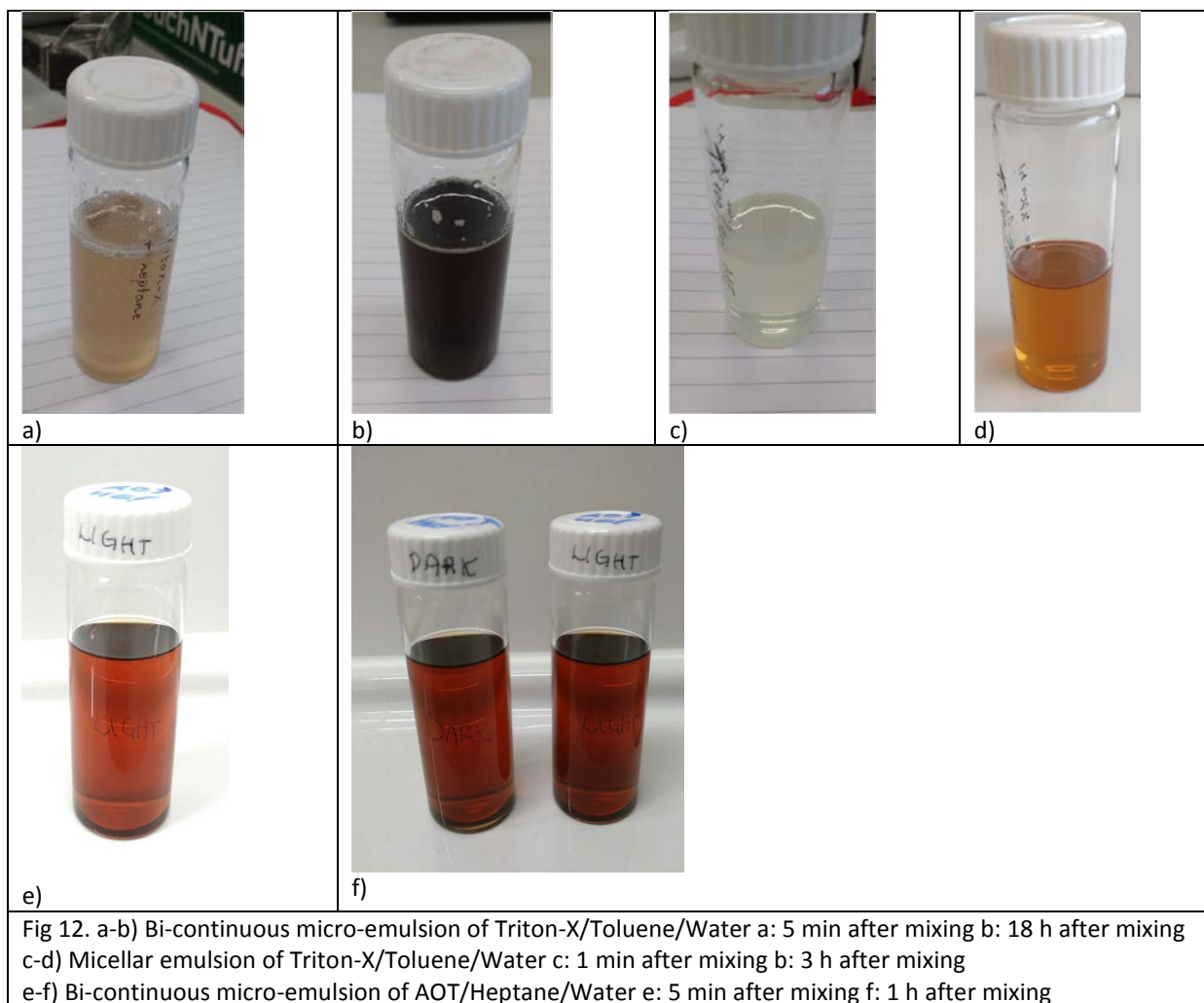


Fig 12. a-b) Bi-continuous micro-emulsion of Triton-X/Toluene/Water a: 5 min after mixing b: 18 h after mixing
 c-d) Micellar emulsion of Triton-X/Toluene/Water c: 1 min after mixing b: 3 h after mixing
 e-f) Bi-continuous micro-emulsion of AOT/Heptane/Water e: 5 min after mixing f: 1 h after mixing

Such spontaneous reduction of silver ions is most likely not compatible with core-shell synthesis based on galvanic replacement, since the crucial step relies on the shell metal being reduced only by means of oxidizing the core metal. A possibility is still to achieve core-shell particles with Ag-seeds making up the shell surrounding the Fe core.

2.5.2 Characterization

When the synthesis was carried out according to the core-shell synthesis method described in this chapter, in order to see if raspberry type Ag@Fe core-shell particles could be made, analysis by ICP-AES and EDX reveal that no Fe is present in the final catalyst. Pure Ag samples were also synthesized using both micro-emulsion systems. DLS analysis reveal particle sizes predominately around 30-50 nm, as presented in Fig 13.

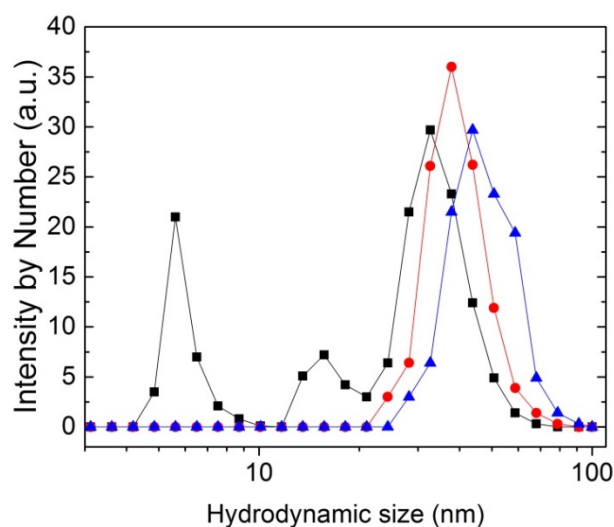


Fig 13 Hydrodynamic particle sizes for the particles made in AOT/Heptane with core-shell procedure (black), pure Ag particles made in AOT/Heptane (red) and pure Ag particles made in Triton X/Toluene. The lines are guide to the eye.

The catalytic activities of commercial Pt and micro-emulsion made Ag towards ORR in alkaline media is shown in Fig 14. The Ag particles show catalytic activity however exhibiting an overpotential approximately 200 mV larger compared to commercial Pt.

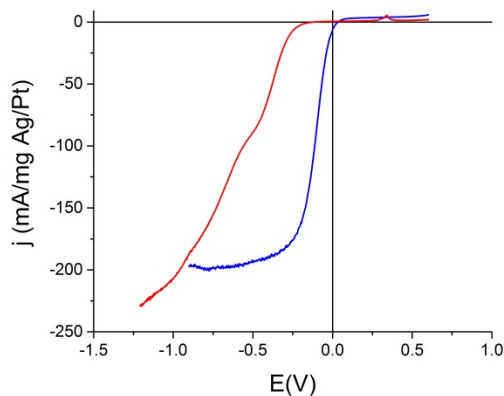


Fig 14 Hydrodynamic voltammogram in alkaline electrolyte at 900 rpm for commercial Pt (blue) and Ag made in micro-emulsion (red)

2.6 Discussion

Particle synthesis

When synthesizing core-shell nanoparticles in micro-emulsion the surfactant molecules prevent particles from agglomeration and hence enable high yield and monodispersity, due to the affinity for the surfactant head group to stick to the metal surface. However, upon completion of the synthesis, any remaining surfactants on the metal surface will affect the chemical and physical properties of

the nanoparticles. On the other hand it has been suggested that this effect may depend on surfactant type and hence where they bind to the metal surface [72]. Newton *et al.*, show an example of Pt nanoparticles with the non-ionic surfactant NP9 adsorbed on the surface that show similar activity to surfactant-free Pt nanoparticles, meanwhile Pt nanoparticles with adsorbed cationic TTAB show a complete absence of Pt characteristics. Surfactant present on the surface of nanoparticles may further influence the surface plasmon behaviour of the particles. In a study by Crespo *et al.*, gold nanoparticles were prepared with a tetraalkylammonium capping agent to demonstrate the influence of surfactant on the magnetic behaviour of the particles. The surface plasmon resonance was measured with UV-vis and it was shown that the density of $5d$ holes could be altered to represent that of bulk gold. Since the magnetic behaviour is determined by the d orbital electrons the presence of surfactants on the surface of the particles induced diamagnetic behaviour of the nanoparticles [73].

One approach that has been employed for efficient surfactant removal is the use of photo-destructible surfactants. Phase separation after synthesis of nanoparticles could be achieved by irradiating and hence decomposing the light sensitive surfactants into non-surface active molecules in a study by Vesperinas and Eastoe [74, 75]. It is sometimes argued that surfactant molecules that remain adsorbed to the catalyst particle surface directly influence the catalytic performance since surface active sites are blocked [76]. The catalytic performance of the core-shell particles synthesized by us in bi-continuous micro-emulsion seem to at least partially agree with such arguments, since platinum characteristic peaks are absent in the voltammogram recorded for core-shell particles produced leaving out *all* the washing procedure, as can be seen in Figure 15.

Regarding the washing procedure the acidic washing step is needed to ensure core-shell structure as mentioned above, however it efficiently washes away surfactant molecules acting partly as anchors between the particles and the carbon support. Too much remaining surfactant lowers the conductivity of the sample and might limit the accessibility of the catalytic particle surface. However, extensive removal appears to induce loosely bound particles and hence lead to agglomeration of particles. This requires further optimization of the procedure.

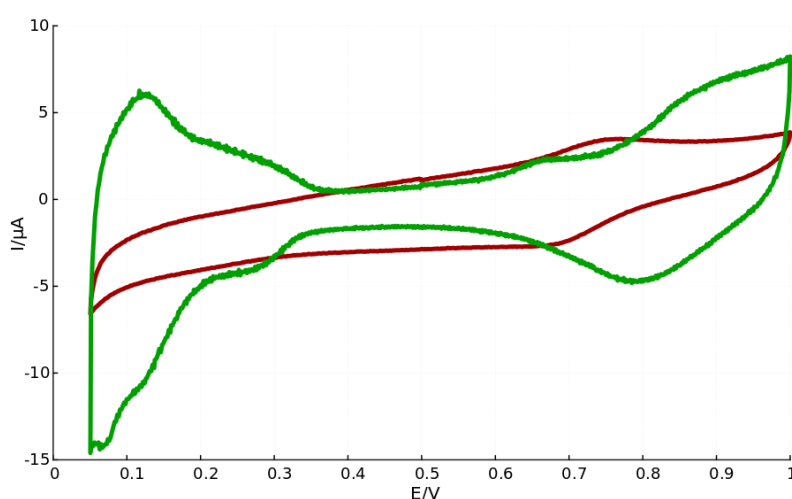


Fig 15. Cyclic voltammograms for Pt@Fe nanoparticles prepared in micro-emulsion, where particles after washing (green curve) exhibit characteristic Pt-peaks and particles with remaining surfactants (red curve) lack this feature.

The mechanism of particle growth in bi-continuous micro-emulsions has been reported previously by our group [58]. The mechanism of galvanic replacement has been described in literature previously [59, 60, 77].

Using the micro-emulsion based method described in this chapter we have successfully produced core-shell particles made of Pt@Fe, Pt@Ni and Pt@Cu. The particles are of core-shell nature on the basis of the following observations:

- 1) Both metals are present in the particles. Due to the washing steps in the synthesis procedure any uncoated core metal should be washed away, hence the presence of both metals in the final particle indicates core-shell type.
- 2) The particle surface. Voltammetry shows activity for ORR in the same (or better) range than pure Pt particles made in bi-continuous micro-emulsion.

Furthermore, using micro-emulsions as a template for making nanoparticles generates very similar core-shell particle size distributions independent on metal precursor, as long as the core synthesis is allowed sufficient time. The synthesis can be used for various metal combinations as long as the shell metal has sufficiently higher reduction potential relative to the core metal. The intrinsic particle growth control offered by the micro-emulsion enables a monodispersed sample despite the addition of a Platinum shell. This underlines the suitability of using micro-emulsions as template for making core-shell particles. Moreover, a high yield of particles is obtained using this scalable method. Nevertheless, what was learned from the synthesis of one core metal type in terms of reaction parameters could not be used without adaptation to make core-shells with another core metal type. The core-surfactant and shell-surfactant affinity difference is expected to play a major role regarding the extent of galvanic replacement.

Limited success was encountered in two cases; Pt@Co and Ag@Me. Synthesizing Pt@Co using our micro-emulsion synthesis proved only partially appropriate. The results suggest that core-shell particles *can* be made but the current synthesis yield a very low amount of core-shell particles. The problem seems to lie in the galvanic replacement step rather than the formation of the core, since pure Co particle synthesis yield similar amount of Co relative to synthesis of Fe, Ni and Cu. One contributing factor might be that cobalt takes hexagonal crystal structure unlike Fe, Ni, Cu and Pt, which rather forms cubic crystals, see Table 4. Such crystallographic mismatch between the core and shell material may of course be further influenced by any oxidized outer layer(s) of the cores. EDX maps suggest that additional Co-rich agglomerates form separately from the rest of the catalyst material, and only a small portion of Co is then available to be covered by Pt. A study by Kettner *et al* presents results suggesting that when a thin layer of Pt is deposited on bulk Co, the Pt tends to segregate from the surface, until almost the entire surface is covered by Co. For nanoparticles with a few Co atoms as a core, however, this is not the case. They suggest that while 3d-metals like Co do not segregate in Pt, the underlying crystal structure is decisive to whether segregation takes place or not, for example if induced by lattice strain [78].

Table 4 Crystal structure and lattice parameters of the metals constituting the nanocatalysts

	Crystal structure	Lattice constants (pm)
Fe	fcc/bcc	a=b=c=286
Ni	fcc	a=b=c=352
Cu	fcc	a=b=c=361
Co	hcp	a=b=251 c=407
Pt	fcc	a=b=c=392

Regarding the synthesis of Ag@Me particles, core-shell particles were not achieved. Attempts to explain the auto-reduction of Ag in micro-emulsion have been made earlier, the main suggestions being surfactant impurities, reduction by hydroperoxide formed from the surfactant polyether chains and the photo-reduction of silver ions in UV-light. The two latter explanations do not fit well with our experimental results. However, if the early reduction of Ag⁺ to Ag⁰ in the emulsion is indeed caused by oxidation of oxyethylene groups into hydroperoxides and subsequent reduction of Ag⁺ by the hydroperoxides, scavengers may play a role to block this reaction. An intrinsic advantage of using *dense* micro-emulsions is the high particle yield in the formation of nanoparticles, however, this is turned into a disadvantage in the case of Ag particles. As soon as crystals of Ag are formed in the micro-emulsion the suitability of using it in a galvanic replacement based synthesis is lost. Structures similar to the raspberry structure described in [79] might be a possible outcome of such synthesis although we were not able to observe this. On the other hand, simple mono-metallic particles seem to be the most likely outcome of this synthesis, further affected by Oswald ripening. In essence – micro-emulsions fail to provide a scaffold for nanoparticle synthesis if reduction is not controlled. Ag particles generated in the micro-emulsions are approximately 30-40 nm, thus considerably larger than the micro-emulsion water channels!

Characterization

Regarding the miscellaneous nature of the iron core in the Pt@Fe particles, the XPS spectra and the low magnetization saturation values obtained in the SQUID analysis seem to suggest a *core-shell-shell* configuration with a Fe-FeO-Pt configuration. It is not unexpected that a slow oxidation takes place, even if the conditions are not deliberately aimed for oxidation. For core-shell particles as small as 3-4 nm, depending on the composition, the penetration depth in XPS is approaching the particle diameter. This makes it rather a “bulk” technique than a surface sensitive technique, allowing for analysis of the core material.

Considering the impact of a core-shell structure on the magnetic properties of nanoparticles, it is fair to assume that some effect will be present on the magnetic properties of the core. Since saturation magnetization is defined as “per gram”, a non-magnetic shell will inevitably decrease its value. A magnetic shell on the other hand might alter the anisotropy causing a shift in the hysteresis loop [64]. The low saturation magnetization observed for our Pt@Fe particles is mainly a result from the very small size of the core and possibly partly oxidized nature. The ferromagnetic behaviour observed for the Pt@Co particles might be a result of a thinner Pt shell or possibly the presence of large undissolved Co clusters. The domain size might indeed be larger than that required for superparamagnetic behaviour.

2.7 Conclusions

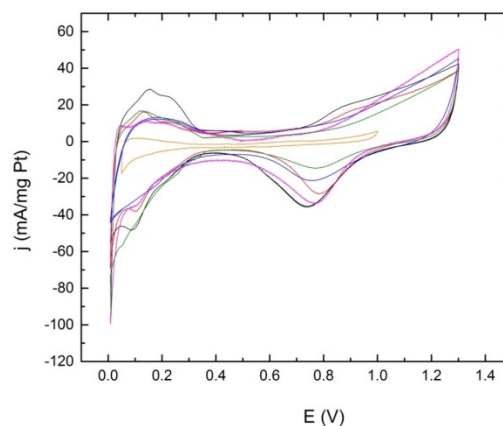
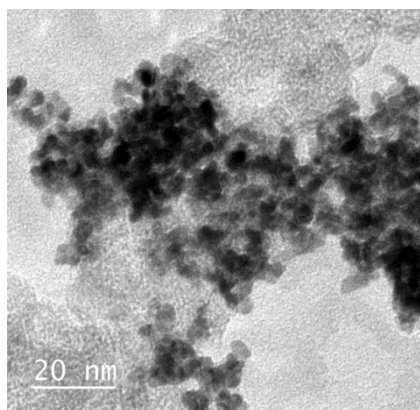
In conclusion we find our micro-emulsion core-shell synthesis to be a suitable technique to produce monodispersed bi-metallic core-shell particles, where the shell is Pt and the core is Fe, Ni or Cu, in a scalable fashion.

In two cases, a high core-shell particles yield could not be achieved with this method;

- 1) For Pt@Co particle synthesis, the method proposed produce very low yields of actual Pt@Co particles and most of the initial metal content is lost, possibly due to the mismatch of crystal structures between Co and Pt.
- 2) The method proved not to be suitable for synthesise of Ag@Me particles due to the formation of Ag crystals prior to the addition of reducing agent in the micro-emulsion. This would imply that a mix of core-shell particles and pure silver particles would be formed or possibly only pure silver particles. The “Ag@Fe” particles that were synthesized in bi-continuous micro-emulsion contained no Fe by the end of the synthesis. The pure Ag particles show activity towards ORR but with a higher overpotential compared to Pt nanoparticles. Moreover, the Ag particles are approximately 10 times larger than observed for other similarly prepared metals, losing out on the benefits of micro-emulsion synthesis. The auto-reduction of silver ions taking place in micro-emulsion does not seem to depend on the presence of UV-light.

What was learned from one the synthesis of one core-shell metal type could not be translated directly into another core type without adaptation. Core-surfactant and shell-surfactant affinity plays a major role. The most important factor in obtaining a high yield of Pt@Fe, Pt@Ni and Pt@Cu seem to be the adsorption time of the particles on carbon.

3 How to determine the core-shell nature in bimetallic catalyst particles?



3.1 Abstract

Nanometre-sized materials have significantly different chemical and physical properties compared to bulk material. However, these properties do not only depend on the elemental composition but also on the structure, shape, size and arrangement. Hence, it is not only of great importance to develop synthesis routes that enable control over the final structure but also characterization strategies that verify the exact nature of the nanoparticles obtained. Here, we consider the verification of contemporary synthesis strategies for the preparation of bimetallic core-shell particles in particular in relation to potential particle structures, such as partial absence of core, alloying and raspberry-like surface. It is discussed what properties must be investigated in order to fully confirm a covering, pin-hole free shell and which characterization techniques can provide such information. Not uncommonly, characterization strategies of core-shell particles rely heavily on visual imaging like transmission electron microscopy. The strengths and weaknesses of various techniques based on scattering, diffraction, transmission and absorption for investigating core-shell particles are discussed and, in particular, cases where structural ambiguities still remain will be highlighted. Our main conclusion is that for particles with extremely thin or mono-layered shells—*i.e.*, structures outside the limitation of most imaging techniques—other strategies, not involving spectroscopy or imaging, are to be employed.

3.2 Introduction

For particles in the size range beneath 5 nm, optical, chemical and physical properties of the nanocrystal surface are strongly altered compared to those of bulk material [80, 81]. Moreover, the high surface-to-volume ratio makes them suitable candidates for catalysis applications [82, 83]. Such particles may be composed of one or more elements, typically metals, arranged into mixed or structured configurations. For catalysis purposes special attention has been drawn to bimetallic core-shell nanoparticles, since such particles maximize the use and exposure of the catalytically active surface material. Apart from the obvious benefit of a core-shell structure, namely adding a bulk property such as reduction of particle mass while maintaining surface properties, it is believed that geometric effects, e.g., lattice strain, caused by the underlying structure play a key role in enhancing the catalytic properties of the surface metal [84-88].

There is a wide spectrum of strategies used for producing core-shell nanoparticles, relying on precipitation, decomposition, surface enrichment, leaching or deposition to obtain core-shell structured particles. The segregation into two spatially separated phases—core and shell—commonly relies on differences in physical and chemical properties between the two metals, e.g., differences in reduction potentials or in affinity for adsorbates, or by the sequence in which the synthesis is carried out. In the first case, the resulting structure is close to local thermodynamic equilibrium whereas in the second case the material is kinetically trapped in the structure.

Particle formation through precipitation is commonly carried out by reduction of metal containing precursors in aqueous or organic solution at high [89, 90] or low [60, 91, 92] temperature. Decomposition of thermally unstable metal-organic precursors is another, relatively classical route that lately has been refined and tuned [83, 86, 93]. Furthermore, alloy nanoparticles can be treated, either thermally [94, 95] or by adsorbates [85, 96], in such a way that one metal component thermodynamically prefers to segregate to the surface. Removing a metal component from the surface of an alloy particle through leaching can be done (electro)chemically [97, 98]. By depositing one metal on top of the other, the core particle can be used as a seed or nucleation centre when e.g., reducing a second metal precursor [90, 99, 100]. Alternatively, the outermost atoms of the core particle are sacrificed by using galvanic displacement of the core metal in favour of the shell metal [60, 101, 102]. Irrespective of the synthesis route, the technique ideally needs to ensure controllability of the core size and shell thickness as well as the formation of a uniform and intact shell. This turns out to be neither trivial nor easily achieved.

As a way to control the growth of nanoparticles, micro-emulsion techniques can be employed, in which the nucleation and growth of the particles takes place within the confined space of inverted micelles or channels [103]. Micro-emulsions are nanostructured dispersions of two immiscible liquids, stabilized interfacially by surface active molecules. The key aspect of most micro-emulsion techniques is that water-phase nanoreactors can be tuned in size and yield monodispersed nanoparticles [83, 103]. Recently, we have developed a synthesis method based on bi-continuous micro-emulsions that is capable of high yield production of ultrafine, monodispersed nanoparticles, see [58] and references therein. By expanding this method we have explored the possibilities of synthesizing also core-shell nanoparticles in a dense heptane/water/AOT bi-continuous micro-emulsion system. Using this example we will discuss some of the specific characterisation challenges that are associated with nanoparticles produced in micro-emulsions.

For micro-emulsion techniques as well as aqueous synthesis techniques, it is common to use galvanic displacement for adding the shell material, relying on the difference in the electrochemical reducing potential between the core and the shell metal [60, 104-106]. It is here assumed that the dominating mechanism involved is replacement of core surface atoms with shell precursor ions, preventing the reduction of shell ions exclusively on the core surface in the system. The success of galvanic replacement appears to largely depend on the reaction conditions, the metals used and the compatibility between them. It is important to point out that galvanic replacement in aqueous media is strictly confined to the aqueous chemistry of the metals involved. Many non-noble metals like iron or copper form oxides at neutral or high pH, limiting the reducing potential of the surface core atoms [60].

When relying on galvanic displacement for depositing the shell, a uniform dispersion of the shell precursor is crucial. This is especially critical when the synthesis takes place within a micro-emulsion where the dispersion naturally is limited by the exchange between the micelles/channels. In case of excessive amounts of shell precursor present, the core particles could be completely oxidized upon the formation of particles consisting of shell material. In contrast, the core particles could be left with incomplete shells if the shell precursor concentration is very low [107, 108], see Figure 1. Tojo *et al.*, suggested that since the surfactant flexibility affects intermicellar exchange, choosing a surfactant accordingly can play a crucial role in steering the final structure towards core-shell type structure or a more alloyed structure.

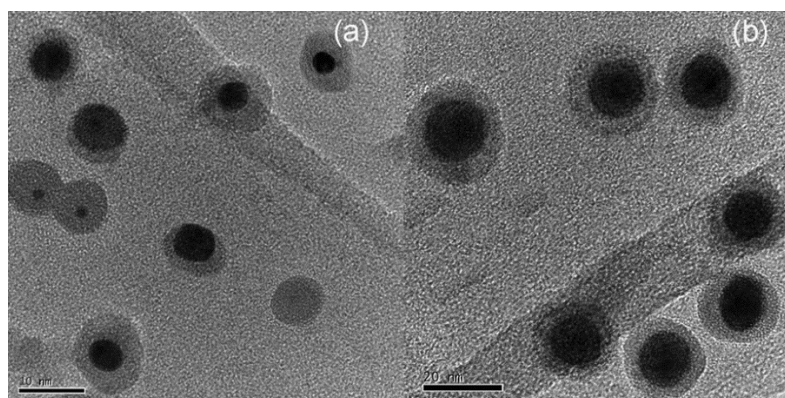


Fig 1. TEM micrographs of Ni-core Au-shell nanoparticles prepared in micro-emulsion using galvanic displacement for shell deposition. Core-shell particles prepared with a molar ratio of water to surfactant of 5: (a) display an example of inhomogeneous galvanic displacement whereas particles prepared with a higher ratio, 9; (b) have more even shell thicknesses (Reprinted with permission from [107], 2009, Elsevier).

One major challenge when synthesizing core-shell particles is to ensure a smooth and pin-hole free shell covering a well-defined core. There are many examples where the final structure deviates from this ideal. Upon deposition of the shell material on the core by a second-step reduction of metal ions, small metal particles can nucleate on the surface of the core and remain as spheres decorating the core, also referred to as “raspberry structure”. Such structures have been obtained by addition of polymeric surface active molecules, such as poly(vinylpyrrolidone) [79] or a polyethylene glycol-based polymer [109], preventing particle agglomeration. However, not fundamentally different structures were also obtained—albeit not intentionally—in core-shell synthesis routes based on hydrothermal synthesis [90], galvanic replacement in micro-emulsion [60, 106] and sequential deposition [106]. High

temperature annealing could smoothen such shells with the risk of sintering particles and hence reducing the active surface of the catalyst particles.

Another example of unwanted structures is hollow particles. Alongside the core-shell particles synthesized by a sequential deposition method [106] and a micro-emulsion method [92], hollow particles were also obtained, consisting of either mixed core and shell material or just the material in the shell. In addition, galvanic displacement has been used with the intention to create hollow particles [97]. By adding precursor material sequentially it is often assumed that a core-shell structure is achieved. Examples of both scenarios where, despite subsequent addition of the shell material, alloy particles were formed rather than core-shells are given in [110], and particles with an alloy core rather than a pure non-noble metal core in [104].

Although many synthesis strategies have been developed over the last years to improve controllability of the size, shape and shell thickness, the characterization step becomes utterly important in order not only to refine the synthesis routes to avoid any unwanted structures but also to correlate the final properties of the material with the true structure of the particles. In this contribution, the suitability of common characterization techniques for investigating the true nature of core-shell catalyst particles will be assessed and graded. In doing so, we have taken the liberty of citing only those works as deemed relevant to illustrate a particular point rather than making an extensive review of all work done in the field.

3.3 Methods

When the focus is on confirming or excluding the formation of core-shell structure in nanometre sized bimetallic catalyst particles, a number of properties need to be investigated, such as elemental composition and distribution, oxidation state and crystal structure, shell coverage or surface abundance of particular elements. In addition, information about the particle size and surface area, size distribution and possible agglomeration form the basis of particle characterization and may assist in the assessment. Complementary to spectroscopic and microscopic imaging techniques are measurements of the optical, magnetic and catalytic properties of the nanoparticles.

Many particle surface characterization techniques employ either electrons or photons as incident radiation and use either elastically or inelastically scattered electrons or photons for detection. The term absorption refers to the partial absence of scattered or transmitted radiation. A technique can be considered surface sensitive when the larger part of the radiation to be detected originates from no more than a few atomic layers depth in the sample [83, 110].

3.3.1 Electron Microscopy/Spectroscopy

For the study of nano-sized particles electron microscopy is highly relevant since electron beams can be focused down to small dimensions. When an electron beam is focused on a sample, the electrons interact with the specimen atoms giving rise to inelastic and elastic scattering of electrons, X-rays, and, if the sample is thin enough, some electrons will be transmitted through the sample. Apart from secondary electrons, backscattered electrons and Auger electrons being emitted from the sample upon irradiation by the electron beam, X-rays are emitted from areas corresponding to almost the complete penetration depth of the electron beam. In principle, all kinds of generated electrons, as well

as the characteristic X-rays, can be used for image formation - each of these leading to a different kind of microscopy technique.

In general, the volume of material analysed by an electron microprobe depends on many factors. The depth of penetration and the volume of sample with which it interacts is a function of its angle of incidence, the magnitude of its current, the accelerating voltage and the atomic number of the element under analysis [111]. The penetration depth is approximated by

$$x/\mu\text{m} = 0.1 E_0^{1.5}/\rho \quad (1)$$

where E_0 is the accelerating voltage in kV and ρ is the mass density in g/cm^3 . With an accelerating voltage of 10 kV and a mass density close to that of water one finds the typical value of 3 μm .

A Scanning Electron Microscope (SEM) is typically fitted with detectors for Backscattered Electron Imaging (BEI) and Secondary Electron Imaging (SEI). Backscattered electrons have energies close to those of the incident beam, *i.e.*, larger than 50 eV [112, 113]. Secondary electrons are emitted by atoms nearer to the surface of the sample, from 1–10 nm depth, making SEI more surface sensitive and of higher resolution compared to backscattered electrons where the escape depth is half the penetration depth and hence larger. On the other hand, backscattered electrons are sensitive to the electron density of the atoms giving a better image contrast between heavy and light elements. The spatial resolution of SEM depends on the size of the electron spot, which in turn depends on both the wavelength of the electrons and the electron-optical system which produces the scanning beam. The resolution is also limited by the size of the interaction volume, or the extent to which the material interacts with the electron beam. The spot size and the interaction volume are both large compared to the distances between atoms, so the resolution of SEM is not high enough to image individual atoms.

In Transmission Electron Microscopy (TEM) the image is generated by detecting primary electrons transmitted through an ultra-thin sliced sample, typically less than 100 nm [114]. In many modern TEMs there are two high resolution imaging modes: High-Resolution Transmission Electron Microscopy (HRTEM) and Scanning Transmission Electron Microscopy (STEM). HRTEM is essentially a phase contrast technique [83]. In STEM the electron beam is focused and scanned over the sample. The electrons that are scattered are collected in a series of detectors covering different angular ranges [115]. Generally, the spatial resolution is limited by the probe size of the microscope. In conventional high-resolution TEM and STEM the resolution of the final image is limited by the aberrations in the imaging lenses. The resolution is given by,

$$D = 0.43 C_s^{1/4} \cdot \lambda^{3/4} \quad (2)$$

where λ is the wavelength of the electrons and C_s is the aberration coefficient of the lens. Hence, the resolution can be improved by two methods—higher voltage and lower C_s . For an uncorrected, $C_s = 0.5$ mm, state-of-the-art 200 kV TEM microscope, $\lambda = 2.5$ pm, this gives a probe size of about 0.12 nm [115, 116]. For aberration corrected STEM microscopes, the probe size can nowadays approach 0.05 nm. The smaller probe gives not only better spatial resolution but also more current, resulting in a better signal-to-noise ratio and a higher sensitivity [83]. The discriminating compositional depth will be dependent on the maximum resolution, hence, shell thicknesses close to the resolution of a

specific instrument will be outside the range of detection. Spatial resolutions of around 0.1 nm are nowadays commonly achieved [117].

Although image contrast in TEM is specific to the type of element, TEM is usually complemented with spectroscopic detectors enabling compositional analysis, such as Energy Dispersive X-ray (EDX) spectroscopy. On the high end of the spectrum, STEM accompanied with Electron Energy Loss Spectroscopy (EELS) or High-Angle Annular Dark Field (HAADF) imaging, composition profiling can be made across the particles taking advantage of the close-to-atomic resolution [89, 106, 118]. In Electron Energy Loss Spectroscopy (EELS) the energy distribution of initially mono-energetic electrons, after they have interacted with the sample, is being measured using an energy loss filter [119, 120]. Transmission EELS can be used in conjunction with TEM, taking advantage of its imaging capabilities, when the sample is thin enough to transmit electrons, about 1 μm for an 100 kV beam, to obtain structural and elemental analysis [117]. In order to achieve surface sensitivity, in reflection EELS the angle of the incident beam is set to allow electrons to penetrate only up to shallow depths before being scattered. Transmitted electrons that have significantly altered their angular direction upon interaction with the sample atoms can be detected using a HAADF detector [83, 120]. The signal intensity depends on the number of atoms as well as the scattering properties of the atom, which in turn strongly depends on the atom number. Therefore, a STEM fitted with a HAADF detector enables compositional discrimination.

Upon excitation of an inner shell electron, an electron from an outer shell falls to the lower energy level. The energy released from the second electron consequently excites an Auger electron, leaving the atom with two vacancies. Such electrons have an escape depth in the order of 1 nm making Auger electron spectroscopy a surface sensitive technique. Auger electrons are, like secondary electrons, of low energy type, in the range of 20–500 eV. Ultrahigh vacuum is required and although Auger electrons can be generated with both incident electrons or X-rays the best spatial resolution is achieved with an electron beam, reaching around 2 nm resolution [117]. Generally a low current improves the spatial resolution but in some cases elemental sensitivity can be compromised and the higher current gives higher surface sensitivity. Auger electron energies are element specific allowing for elemental characterization. Imaging is further enabled by Scanning Auger Microscopy (SAM), in which the image resolution generally is influenced by some sample-specific effects: the Auger electron escape depth, the surface topography and the contribution from secondary electrons [116].

Depending on the material and intensity of incident electron beam, X-rays are generated in a region up to 2 μm in depth [83]. Generated X-rays are element specific, hence compositional analysis is enabled in scanning electron microscopy and transmission electron microscopy when fitted with EDX microanalysis detectors.

Electron beam methods, such as EELS or AES can be destructive, since inelastic scattering of the incident electrons can result in radiation damage. TEM on the other hand utilizes elastic scattering, which is relatively strong, however, radiation damage could still be a problem since this technique often is used to determine structure down to the atomic level [117].

3.3.2 X-ray Scattering

X-ray Diffraction (XRD) is carried out by irradiating a sample with X-rays at varying incident angles, thereby measuring the elastic scattering of X-rays. Depending on the crystal lattice spacing and the angle and wavelength of the incident X-rays, following Bragg's law, the scattered X-rays will either

constructively or destructively interfere and give rise to signal peaks in a so-called diffractogram. Intrinsically, XRD is a suitable technique for measuring lattice parameters and crystal symmetries. By scanning the sample through a range of angles, all possible diffraction directions of the lattice should be attained due to the random orientation of the material that is macroscopically in powder form. Conversion of the diffraction peaks to “*d*-spacings” allows identification of the crystal. Typically, this is achieved by comparison of *d*-spacings with standard reference patterns. Furthermore, the peak width, position and intensity is used to extract chemical composition, crystal structure and crystallite size. The usual information depth of XRD measurements ranges from a few micrometres to a few hundred micrometres, depending on the electron density of the material. The spot size is typically in the range of a few mm², making XRD a bulk analysis technique. Since XRD commonly scans over momentum rather than wavelengths it is strictly speaking not spectroscopy, although commonly referred to as being such. As described by Cullity et al., Bragg’s law can be utilized in two ways; in x-ray diffraction by using x-rays of known wavelength and measuring scattering angle, giving information about the spacing of various planes in a crystal. Alternatively, in x-ray *spectroscopy* a crystal with planes of known spacing can be used, measuring scattering angle, and thus exploring the wavelength space of the x-rays, wavelength or photon-energy [121].

X-ray Photoelectron Spectroscopy (XPS), also known as Electron Spectroscopy for Chemical Analysis (ESCA) is one of the most frequently used techniques for characterising core-shell catalyst particles as it provides information about the elements and their chemical states in the analysed layers. In XPS the sample is irradiated with an X-ray beam, typically from an Al K α source at 1486.6 eV or an Mg K α source at 1253.6 eV, thereby ejecting core electrons from the material. Due to the short range of the ejected photoelectrons, the detected photoelectrons originate from the surface region, typically the topmost 1–10 nm. The measured intensity for a given depth *z* in XPS, for homogeneous materials follows to a first approximation the exponential relationship

$$I(z) = I(z = 0) \exp(-z \cos \theta / \lambda) \quad (3)$$

where θ is the angle between the surface and the analyser direction. The mean free path λ of photoelectrons is element specific and proportional to the electron kinetic energy [122]. Consequently, the measured intensity of an XPS profile in a conventional XPS will be an average of the contribution from different depths [110]. For an extensive overview of the inelastic mean free paths, see Tanuma *et al.* [122]. The highest surface sensitivity, in the range of 1 nm, is obtained with electrons at kinetic energies around 15–100 eV. In this region, most of the emitted photoelectrons originate from the outermost atomic layer. Since the photon energy is fixed and the binding energy is specific for each shell and element, analysis of the energy spectra of photoelectrons provides an effective means to study elemental composition of a sample. Moreover, the peak shape and position are sensitive to the chemical state of the atom, XPS can also provide information about chemical bonding, e.g., on the difference in oxidation state, difference in molecular environment, difference in lattice site *etc.* [83, 123].

3.3.3 Absorption Spectroscopies

Due to inelastic scattering of incident X-rays on a sample some of the energy is absorbed by the sample in a way similar to optical spectroscopy. Transmission of X-rays through a sample is hence also described by a Lambert-Beer kind of relationship:

$$I_T = I_0 \exp(-\mu \cdot t) \quad (4)$$

where I_0 is the incident beam intensity, I_T is the transmitted intensity, μ the absorption coefficient and t the thickness. In X-ray Absorption Spectroscopy (XAS) the absorption coefficient is measured as a function of energy. When the energy of the incoming photon corresponds to the energy of a shell of the atom, e.g., K, L1 or L2, a sharp rise in the absorption coefficient occurs, called absorption edge. Such absorption edges are unique for each element making XAS an element specific technique. In the analysis region ranging from about 10 eV below to about 30 eV above the absorption edge E_0 , the method is called X-ray Absorption Near Edge Structure (XANES) and for the energy regions above $E_0 + 30$ eV, Extended X-ray Absorption Fine Structure (EXAFS). The two methods are complimentary: XANES giving information about oxidation state and coordination environment of the metal atoms and EXAFS revealing structural parameters like nearest-neighbour distance and adsorbates and ligands [83, 93]. The surface sensitivity is directly related to the absorption coefficient of the material and hence varies strongly as a function of wavelength.

Nano-sized particles have optical properties that depend on their size, shape, concentration, agglomeration state and refractive index. In UV-Vis spectroscopy the contribution from absorption relative to scattering is generally greater for smaller particles, less than 10 nm, and has been described by Mie theory [124, 125]. The surface of a metal is like plasma, having free electrons in the conduction band and positively charged nuclei. Surface Plasmon Resonance (SPR) is a collective excitation of the electrons in the conduction band on the boundary of the metal particles [126, 127]. Due to the confinement by the particle size and shape, the electrons are limited to specific vibration modes. Therefore, dispersions of metal particles show characteristic absorption bands in the UV and visible range. The absorption spectra of metal nanoparticles are dependent on the particle size and wavelength and can hence be used to determine size and to extract elemental information. The surface sensitivity of the technique is, as described above for XAS, strongly dependent on the absorption coefficient and hence strongly depends on wavelength.

3.3.4 Other

In Atomic Force Microscopy (AFM) an atomically sharp tip is scanned over a surface with constant height or with constant force, thus acquiring height or force information respectively. The tip is attached to a reflective cantilever and as it moves up and down over the surface and a photo detector measures how a laser beam directed to the cantilever is deflected. The signal is subsequently converted to a voltage and an image is produced [83]. Since the tip follows the profile of the outermost surface atomic layer, AFM is intrinsically a surface sensing technique. The radius of curvature of the end of the tip will determine the highest lateral resolution obtainable with a specific tip, meanwhile the vertical resolution is limited by the vibrational environment of the instrument. Typically, AFM instruments have a lateral resolution of around 1 nm and a vertical resolution of around 0.1 nm. If the particles are assumed to be spherical, the height measurement corresponds to the diameter of the particle.

(Electro-) chemical activity measurements are crucial for checking the suitability of the nanoparticles for the final purpose of the material but can also provide valuable information on the structure. In heterogeneous catalysis, it is primarily the surface properties that determine the activation and reaction mechanisms. Hence, for particles aimed to be used in heterogeneous catalysis, information about the surface structure is of highest importance. This, in principle, means that the outer-most layer of atoms of the catalyst particle is of particular interest. In techniques like Cyclic Voltammetry (CV) surface redox reactions are probed by letting the potential on the working electrode be swept

over a potential range as the current response is being measured. As a result, the potential and kinetics of the redox reactions can be used as material specific fingerprints and be correlated to properties like catalytic activity, electrochemically active surface area, affinity for adsorbates etc. [128].

3.4 Results

The aspects of the critical assessment of the available techniques are summarized in Table 1 and include depth and spatial resolution, composition and elemental distribution, geometrical structure and porosity, and other chemical or physical properties. The results are discussed below and are summarized in their entirety in Table 2. The following section will discuss the various entries in successive order.

Table 1 Criteria used for the critical assessment of available techniques.

Label used	--	-	0	+	++
Surface sensitivity	transmission	> 10 nm	3–10 nm	1–2 nm	< 1 nm
Spatial resolution	bulk	> 10 nm	2–10 nm	0.1–1 nm	< 0.1 nm
Composition	Signal strength, sensitivity to atom number, sensitivity to environment/neighboring atoms, oxidation state.				
Elemental distribution	Ability to determine the distribution of elements across the particle, alloying and crystal structure.				
Geometry/Porosity	Ability to determine particle size and geometry, particle dispersity and shell porosity.				

Table 2 Grading of characterization techniques.

Technique	Type	Technique	Surface sensitivity	Spatial resolution	Composition	Elemental distribution	Geometry/Porosity	Other chemical or physical properties
Electron Microscopy	$e^- \rightarrow e^-$	SEM, SEI, BEI	SEI + BEI -	○	n/a	-	--	
		TEM, HRTEM, STEM	--	++	n/a	+	+	
Electron Spectroscopy	$e^- \rightarrow e^-$	EELS	Tr-EELS-- Refl-EELS +	+	+	++	See TEM	
		AES	+	○	○	+	○	Adsorption and chemisorption of gases
		HAADF	--	+	+	+	See TEM	
	$e^- \rightarrow \lambda$	EDX	-	○	+	-	--	
X-ray Scattering	$\lambda \rightarrow \lambda$	XRD	-	--	+	○	--	
	$\lambda \rightarrow e^-$	XPS	+	--	++	++	-	Organic surface contaminants
Absorption spectroscopy	λ	XAS	--	--	+	+	+	Adsorbates /Ligands
	λ	UV-vis	+	--	○	-	○	SPR
Other		AFM	++	+	--	○	+	
		Cyclic Voltammetry	++	--	+	-	+	Catalytic activity

3.4.1 Electron Microscopy and Spectroscopy

Spotting individual particles on nanoscale, and even less so the potential core-shell structures therein, is for most standard SEM equipment too much of a challenge. SEM in conjunction with EDX microanalysis, however, offers a good alternative for bulk compositional analysis. TEM is commonly considered as perhaps the most, on its own, exhaustive imaging technique for determining core-shell structures in nanoparticles due to the high resolution achievable. However, the amount and accuracy of the information extracted depends strongly on the elemental composition of the particles and also on the quality of the instrument itself. Moreover, due to the fact that the electrons penetrate deep into if not through the sample, the response will inevitably contain mixed information from both the core and the shell phases [118], hence lacking the sensitivity to surface structure. The sub-nanometre resolution of some high resolution TEMs opens up the possibility to come close to spotting individual atoms within the nanoparticle [83, 120, 129]. Thereby, the distribution, crystal structure, particle size and dispersity can be visualized. For determining particle size in TEM the accuracy is limited since the size typically is uncertain to at least one or two lattice fringes, about 0.2 nm. For particles smaller than 2 nm, this induces a significant error, considering the difficulty in achieving perfectly monodispersed and homogeneous samples. In addition, beam heating during imaging resulting in particle melting or sintering can diffuse the particle boundaries. Furthermore, one obvious drawback in determining dispersity by using TEM is the tiny size of the area viewed relative to the entire sample [83]. Surface topography, particle distribution and crystal planes can be imaged using TEM but to extract

compositional information an element specific signal detector is needed. Compositional profiling of individual nanoparticles is often sought for and enabled when suitable spectroscopy techniques are accompanied with the TEM/STEM setup, such as EDX, EELS, HAADF, in order to discriminate core from shell. There are examples where standard laboratory TEM with EDX provides sophisticated compositional profiling across individual core-shell particles with down to 1 nm steps. One example is the study of silver-core platinum-shell type particles by Wojtysiak *et al.*, where profiling could help distinguishing core-shell particles from hollow Pt particles [106]. Even more impressive step resolution profiling is achieved with STEM-EELS setups [89, 90, 102, 118] with examples for particles not more than 2 nm in diameter [119]. Although this kind of profiling struggles to exclude the presence of pores through the shell, which could only be estimated visually, standard EDX has been used as a tool to investigate the intactness of the shell. In a study on Ni/Au core-shell particles made in micro-emulsion by Chen *et al.*, EDX was used to probe whether the core metal (Ni) had been oxidized in the presence of air through possible pores in otherwise the protective (Au) shell layer [107]. Further TEM compositional profiling methods are limited in determining possible alloying of two metals in bimetallic core-shell particles. An attempt to resolve the issue with inevitably combined signals from the core and shell was made by Mendis *et al.* [118]. By using STEM fitted with EELS and HAADF in combination with linear regression analysis, compositional profiles were made with resolution steps as small as 0.1 nm for a set of TiN-core Ti-oxide-shell and Cu-core Cu-oxide-shell particles. An analytical method was developed to determine the relative amount of each element within each region, *i.e.*, core, interface and shell. Inaccuracy arises, however, due to non-uniform shell thickness of “real” particles using a model that assumes an idealized spherical geometry. Nonetheless, the model was able to give qualitative results for elemental compositions within each region.

Because of the shallow escape depth of Auger electrons, AES is the most surface sensitive among the electron scattering techniques. However, the measured signal is relatively weak as only a fraction of the excited Auger electrons will be detected, which in practice makes the signal-to-noise ratio a limiting factor for the resolution [117, 123]. When using AES for compositional analysis it is important to keep in mind that the release of Auger electrons, and secondary electrons for that matter, from small core-shell type particles is rather different to that from flat surfaces. If the particle radius is smaller than the inelastic mean free path then all electrons generated inside the particle will escape without losing energy, hence corrupting the distinction between surface or shell and bulk or core signals [114, 116]. An example of that was performed by Liu *et al.*, who analysed alumina supporting 2 nm sized silver nanoparticles [116]. An option for slightly larger core-shell particles is to perform a line scan, benefitting from the surface sensitivity despite the moderate resolution [114]. Upon excitation of a core electron the released energy can either generate the emission of an Auger electron or the emission of X-ray photons. The two processes are complementary and the likelihood for either of the two to take place depends on the atomic number of the element. For low atomic number elements the dominating process is Auger electron emission while heavier elements are more likely to undergo relaxation via X-ray emission. Hence, since low atomic number elements have higher Auger yields, AES is particularly sensitive to these materials [114, 117].

For topographical analysis the imaging of SAM does not reach the same resolution as TEM, however, since AES is based on reflection rather than transmission it does not suffer from the intrinsic problem of mixed signals from core and shell.

3.4.2 X-ray Scattering

Due to the simplicity, speed and availability of XRD, this technique is extensively used for bulk compositional and crystal structure analysis in core-shell particle characterization. Because of the relatively low resolution of XRD, direct information about the distribution of elements is lacking, but on the other hand, crystal structure data can be used to verify or deny presence of alloyed or pure phases within the sample. It is, however, important to note that the distinction between a mix of separate core material particles and shell material particles, and core-shell particles would still be a remaining difficulty. It has been attempted to overcome this limitation [130]. In a study by Camardese *et al.*, with the purpose to study the shell thickness of about 10 μm sized Ni/Mn(OH)₂ core-shell particles, two reference materials were chosen: one representing the core material only and the other being a physical mix of core and shell materials in the same proportions as the core-shell sample. Due to absorption of X-rays by the shell, the signal from the core is reduced as compared to the reference mix material. A model was created to correlate the experimental results. There are some advantages using the absorption of X-rays of the shell as a basis for determining the shell thickness; the analysis is based on a large portion of the sample as opposed to single particle profiling. Furthermore, the analysis is quick, cheap and sample preparation is easy. On the other hand, uniformity is assumed and the absorption effect will decrease with decreasing shell thickness until a point where the effect is negligible. For particles smaller than approximately 100 nm, broadening of the X-ray diffraction lines occurs, allowing size measurement based on the Scherrer's equation [131]. This simple approximation is valid when the diffraction material is stress free, since stress contributes to peak broadening as well. The lower size limit for detection with XRD is in the range of 3 nm. An intrinsic limitation of XRD is the fact that amorphous phases cannot be detected. There are numerous examples of studies where the XRD diffractograms of bimetallic core-shell particles only show one of the two supposedly present phases [89]. In such cases, either one of the phases is "truly amorphous" or the crystallite size is under the detection limit of the XRD.

The fact that even standard XPS equipment reaches surface sensitivities as low as 1 nm makes XPS into a powerful tool for core-shell characterization, especially for particles with shell thicknesses larger than 1 nm [60, 83, 91, 132]. Despite the high surface sensitivity, a sampling depth comparable to the outermost atomic layer still cannot be reached [110]. In order to achieve more surface sensitive information there is an option to vary the emission angle in Angular Resolved XPS, ARXPS. However, this technique requires flat surfaces which makes it less suitable for nanoparticle analysis. The second option is to go for lower excitation energies. For this purpose, other sources than conventional laboratory sources like Al K α or Mg K α would be required, since the contribution from the topmost surface layer otherwise only accounts for about 30% of the total signal. Utilizing a synchrotron source and Excitation-energy Resolved XPS (ERXPS) represents one option for discriminating depth profiling of sub-nanometre scale. With the purpose of exploring the suitability of ERXPS for core-shell characterization, Merzlikin *et al.*, investigated a set of gold-core platinum-shell fuel cell catalyst particles. By using 10 nm gold nanoparticles as seeds for the nucleation and growth of small platinum nanoparticles on its surface through reduction by ascorbic acid, the core-shell particles were synthesized and subsequently supported on a standard carbon support [110]. The catalyst particles were then analysed in a synchrotron-based ERXPS. By correlating the relative intensities of the Au and Pt 4f peaks as a function of excitation energies with the escape depth, a composition-depth profile could be created. Interestingly, the results show no enrichment of Pt at

the surface of Au, but rather strong indications of an Au-Pt alloy type or possibly a mix between pure Au and pure Pt particles, despite the sequence of the synthesis route.

In the classical route to destructive depth profiling in XPS, layer by layer is removed from the surface by ion sputtering with consequent XPS measurements. However, the success of this approach in the context of nanometre sized core-shell particles relies on the particles being fixed in position when shot at with the sputtering gun [60, 133].

Since XPS is also sensitive to organic adsorbates it can be used to detect remnants from the synthesis steps, for example the presence of surfactants in case the particles were made in micro-emulsion [76].

3.4.3 Absorption Spectroscopies

XAS provides an option for compositional analysis due to the element specific characteristics, but nonetheless XAS is a bulk analysis technique. One advantage with XAS over other bulk techniques like SEM with EDX is the possibility of doing *in situ* measurements, an approach that has been increasingly used in for example fuel cell catalyst applications [102, 134].

Since the technique is based on measuring the average electronic state and local coordination on a per-atom basis, XAS provides an estimate of particle size, possibly only monometallic. Further information about the surface structure can be achieved thanks to the possibility to probe metal-adsorbate bonding. This is not only useful in cases where the surface roughness and porosity is to be determined but also in the case of catalyst poisoning, e.g., carbon monoxide adsorption to fuel cell catalysts [135].

While studying bimetallic Au/Pd catalyst particles, Balerna *et al.* demonstrated how XANES and EXAFS can be used to distinguish alloy particles from surface enrichment of one metal on top of the other [93]. By studying the nearest-neighbour ratio for Au and Pd in particles prepared via two different synthesis routes, the degree of alloying *versus* core-shell type structure was estimated. Kuttiyiel *et al.*, used XANES and EXAFS to verify the oxidation state of the Ni-core and to check the alloying of Au and Pd in the shell for their 4 nm sized AuPd-shell Ni-core particles [102]. Considerable contributions in this field have also been done by the group of Eichhorn [136-138].

Photons in the UV and visible region do not have sufficient energy to penetrate as deeply into a sample as higher energy photons like X-rays but are absorbed at the surface, making UV-vis spectroscopy relatively surface sensitive. Although UV-vis spectroscopy provides an easy and cheap means for compositional analysis, it is limited to bulk analysis. Furthermore, some metals are more suited for UV-vis analysis than others; gold being an example of a metal which displays distinct optical plasmon absorbance in the visible range [126]. One major application for UV-vis measurements in the characterisation of core-shell particles is to monitor the progress of the particle formation or shell deposition *in situ* [90, 109]. Naturally this holds for liquid-phase synthesis routes. In a study on Au-core SnO₂-shell nanoparticles, absorption spectra consequently taken during the shell deposition, starting from the pure core particles, gave information about the shell formation kinetics [90]. In another study, on Au-core Pt-shell particles the gradual disappearance of the plasmon peak for gold as platinum was deposited, was used as an indication for “complete” coverage of the shell [139]. Furthermore, UV-vis has been used to verify that no uncoated core particles are present alongside the core-shell particles, in terms of absent core-material absorption bands [92].

UV-vis spectroscopy can to a certain extent be used for particle size measurements, however, the contribution of the particle size to the absorption spectra becomes less and less significant with decreasing particle size [125]. Some disadvantages include the requirement of a certain degree of monodispersity and of regular shaped particles in order to achieve accurate measurements. Moreover, the particles need to be in a stable dispersion in order to be analysed as the optical properties are sensitive to agglomeration.

3.4.4 Other

Being a mechanical imaging technique, detailed information about elemental composition in the sample is not available through AFM, but unlike other 2D imaging techniques like SEM, AFM generates a 3D image of the surface, that can be valuable when determining particle distribution on a catalyst support as well as particle geometry and agglomeration [99, 126, 140]. With the intention to examine the extent of shell coverage, Kumar *et al.*, used AFM to characterize their 3 nm sized Au-core Pt-shell particles. After depositing approximately five monolayers of Pt on the gold particles, the coverage was visually determined and compared with complementary results from electrochemical analysis [101]. In practice, however, the resolution is limited by the tip radius and without element specific contrasts it is difficult to distinguish core and shell material at this resolution.

Techniques like CV are intrinsically surface specific techniques. Naturally electrochemical activity measurements provide key information on the suitability of the catalyst particles for their final application in terms of reaction order, kinetics, activation barriers, side reactions, durability *etc.*, In addition, electrochemical techniques can be used in characterization of catalyst nanoparticles. Surface redox reactions are element specific and can be used for compositional analysis; either the surface atoms can be stripped off the surface by oxidation potentials or characteristic adsorption and desorption of other elements, e.g., O, CO or H, on the surface can be measured [87, 91, 102, 106]. In an experiment using CO stripping as characterization method for investigating the surface composition of Ru-core Pt-shell nanoparticles Ochal *et al.*, could demonstrate a Pt shell free from Ru. For the sample consisting of supposedly core-shell type particles the main CO stripping peak is shifted relative to bulk Pt and bulk Ru, but may come from either pure core-shell particles or a shell consisting of both metals. The latter structure could be ruled out by performing CO stripping experiments on several reference materials. Since Ru is easily oxidized and dissolved at negative potentials, a redistribution of Ru takes place causing instability of the CO stripping peaks for reference materials containing surface exposed Ru. Such movement of Ru in the system is not observed for pure core-shell particles where the Ru is fully encapsulated [138].

The platinum-coated silver nanoparticles synthesized by Wojtysiak *et al.*, through different routes exhibit silver stripping (removal of silver from the surface) to varying extent. For the particles synthesized using a stronger reducing agent, a voltammogram similar to pure polycrystalline platinum is achieved and very little silver is stripped off the surface at 0.6 V. This led to the conclusion that a relatively pin-hole free shell was obtained and a minimum required shell thickness was estimated [106].

3.5 Discussion

In this section, we discuss which techniques are most suitable for determining what properties. A complete overview is displayed in Table 2.

Some techniques only reach their full potential when combined with appropriate accessories such as specialized detectors *etc.* Some of the techniques are surface sensitive: they characterize the first few monolayers of atoms. Others, using high energy electrons, probe deeper into the bulk or provide information integrated over the entire sample thickness. Which category of technique is preferable depends on the kind of information that is required. It is evident that as yet no technique can discriminate elements with an atomic resolution. Nevertheless, high-quality TEM microscopes are still in the range of 10 times higher resolution than other spectroscopic techniques. Especially when the characterization of core-shell structures rely on imaging the particles, the high spatial resolution is crucial. Concerning resolution, AFM provides a good alternative that does not require very special analysis conditions such as high vacuum [126].

For compositional analysis there is a wide toolbox at hand. Generally the depth from which the signal is generated, the strength of the signal and the precision of the signal are key elements to estimate the suitability for a specific technique for the specific core-shell particles studied. Both photoelectrons and Auger electrons are low energy electrons and originate intrinsically from near the surface, hence, AES and XPS as well as reflection EELS [117] come close in providing information about the outermost surface layer. For core-shell particles with shell thicknesses greater than 1 nm both AES and XPS are able to give reliable compositional signals. When the technique offers the possibility to vary the escape depth depending on the incident energy, the profiling will reach also beyond the surface layer. Considering the low signal intensity and low Auger yield for heavier elements, XPS is however likely to represent a better alternative for many metal catalyst particles [141].

In combination with excellent surface sensitivity, CV provides an informative tool for compositional analysis of the outermost surface layer.

For bulk composition analysis, both EDX and XRD provide both a cheap and easy option [83]. Moreover, the signal intensities are for both techniques greater as compared to AES and XPS, reducing the signal-to-noise ratio. EDX often represents the simpler choice over EELS for compositional studies, however they are fundamentally different in that EDX detects scattered X-rays and EELS scattered electrons. X-rays are generated from a relatively large volume in the sample as opposed to the lower energy electrons detected in EELS, giving EDX a poorer resolution. Further, the count rate of characteristic X-rays is less than that of core-loss electrons detected in EELS for the same beam current. Moreover, EELS is more sensitive to low atom number elements [117].

To study the distribution of elements within a core-shell particle the two top options consist of line profiling across the particle using STEM-EELS, using the possibility to assess single particles and ERXPS, as signals from each phase—core and shell—can be measured. AES, XRD, XPS and XAS are all sensitive to oxidation states of the atoms, hence, can be used to verify or deny the presence of alloys or oxidized phases [102], however XRD is not the option for very small particles.

Particle size measurements are achieved through various techniques and can be accurately measured through high resolution imaging techniques like TEM even if this is tedious if a size

distribution is to be estimated. XAS is here a bulk alternative but for particle distribution purposes light scattering techniques like Dynamic Light Scattering (DLS) (described elsewhere) might provide an option [142, 143].

Estimating the shell coverage or porosity turns out to be too much of a challenge for most spectroscopic and imaging techniques, although adsorbate sensitive techniques could provide some insight. In contrast, the element specificity and surface sensitivity of electrochemical techniques like CV allow for detection of exposed core atoms, making this a key tool for porosity assessment.

All techniques discussed are to some extent surface sensitive but lose their usefulness when the surface layer gets thinner. The limiting mono-atomic layers can, if at all, be analysed by the presented methods. Hence, no decisive information can be extracted from mono-atomic shell layers.

It is crucial to use a combination of characterization techniques in order to get as close as possible to verifying a core-shell structure. The above discussed results, see Table 2, can be used to find suitable combination of the different techniques.

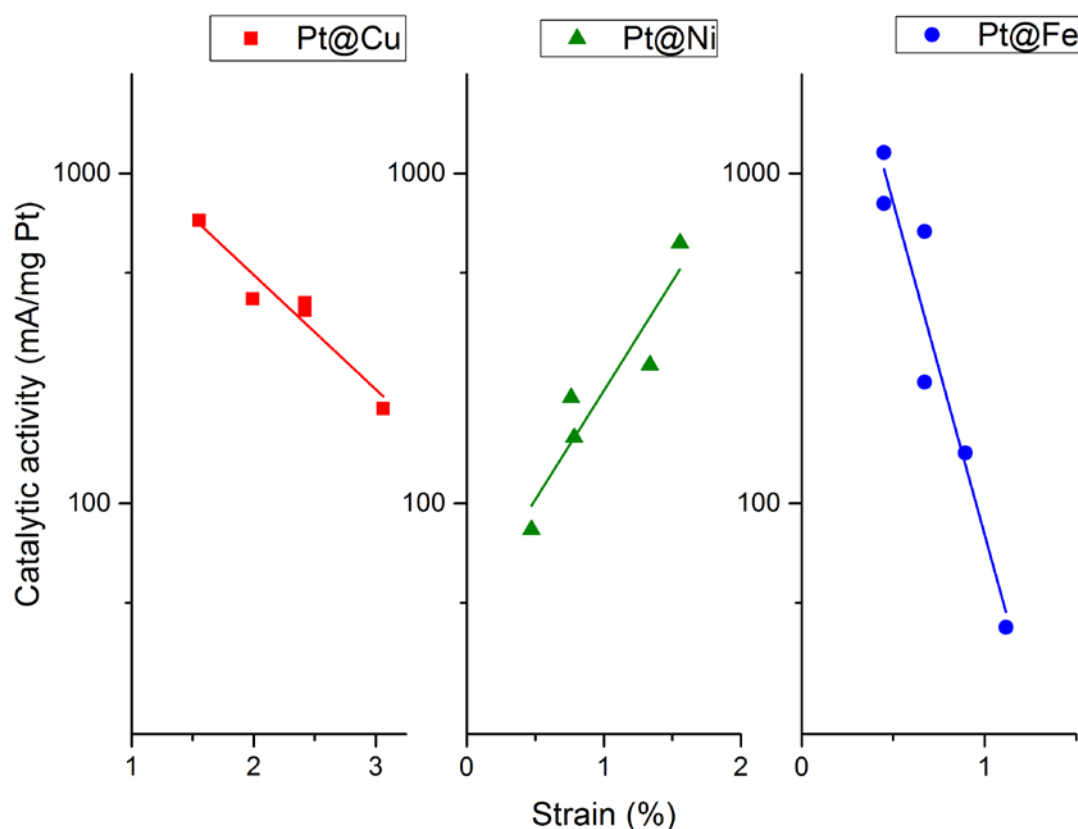
3.6 Conclusion

No synthesis technique so far possesses the ability to accurately control the (geometrical) properties of core-shell particles. Considering the fine balance between achieving a core-shell structure and ending up with unwanted structures, it is evident that a core-shell structure cannot be presumed but needs to be thoroughly investigated. The success of such an investigation depends heavily on the individual instrument quality and on how the available techniques are combined. However, there is no exclusive or general approach to determining core-shell structures.

Any surfactant molecules remaining on the surface on particles made in micro-emulsion will affect the characterization results and may ultimately hamper the catalytic activity for the particles. Surfactant molecules with high affinity for the particle surface are desired to prevent particles from agglomeration but on the other hand they must be removable without causing the final catalyst particles to sinter.

Proving a shell that is pinhole free cannot be done with any spectroscopic technique alone. Complementary electrochemical measurements are crucial in order to get an estimate of the shell porosity. A key feature is the composition of the outermost surface layer—not the least since catalyst particles are intrinsically surface active materials. Although rare, high quality techniques such as microscopes or spectroscopies with capabilities beyond nanometre scale are now emerging and becoming available, eventually opening up the possibility to determine even mono-atomic shell layers. Finally, taking into account the need for high-end instruments, extensive collaboration would benefit the general success in determining the nature of core-shell structured particles.

4 The effect of lattice strain on catalytic activity



4.1 Abstract

Considering the large potential implementation of proton exchange membrane (PEM) fuel cells it is of key interest to find ways to improve the poor oxygen reduction kinetics. A number of strategies have been explored including alloying, multi-layered particles and non-metallic catalysts (*PEM Fuel Cell Electrocatalysts and Catalyst Layers, Springer 2008*) and (*Bing et al 2009*). Apart from a more efficient material use, core-shell type particles provide a method to influence the shell material both geometrically, through lattice deformations, and energetically, through modification of the affinity. A key technique to interrogate the lattice structural modifications of thin Platinum shells is X-Ray Diffraction (XRD). Therefore, we analyse the various contributions of lattice strain and relate these to the corresponding crystallographic response in XRD. Furthermore, we present data on the correlation between strain and activity for three types of core-shell particles – Pt@Fe, Pt@Ni and Pt@Cu – and find an exponential dependence of the activity on strain for all three core-shell types. Finally, we decouple the changes in catalytic activity with respect to a geometrical and an energetic contribution, both of electronic origin.

4.2 Introduction

For core-shell particles a gain in mass activity is to be expected to scale with shell thickness, e.g. roughly 10% increase in mass activity for a 20% reduction of Platinum content in favour of iron. However, as demonstrated in this chapter other factors play a more important role. The motivation for our research is to explore how the catalytic properties of the core-shell surface can be enhanced by manipulating its physical properties.

All particles for the present study are made using a micro-emulsion as a template in order to obtain monodisperse nanoparticles with a high yield. In a micro-emulsion the core is synthesized, followed by the addition of a Platinum shell through galvanic replacement; see Figure 1 for a cartoon. Carbon is added as a support to maximize the accessibility of the catalyst particles. The final washing steps in this procedure remove surfactants, retrieve unreacted Pt and ensure that any uncoated cores are washed away leaving intact core-shell particles only.

Fitting a thin layer of Platinum onto another metal is bound to have consequences for the electronic properties of the Pt shell, both geometrically through lattice mismatch and electronically through shifting of the d-band and, as a consequence, the binding energies for e.g. the oxygen reduction intermediates [39, 144, 145]. Deposited on a metal with a smaller lattice spacing Pt would undergo compressive strain while deposited on a metal with larger lattice spacing, like Au, would result in lattice expansion [39]. The description of the various strain contributions to XRD response has so far only been fragmental in the literature [97, 121, 146] for which reason a short review is included in this chapter.

Similarly, hydrogen adsorption and desorption on Platinum is expected to be influenced by the distorted lattice. Because of this, the common way of calculating the electrochemically active surface area (ECSA) is likely to be little representative. This is because ECSA is estimated using the method, described in e.g. [147, 148], based on the charge associated with adsorption and desorption of hydrogen on a bulk Platinum surface, the Platinum loading on the electrode and an estimated Coulombic charge required to desorb hydrogen from Platinum.

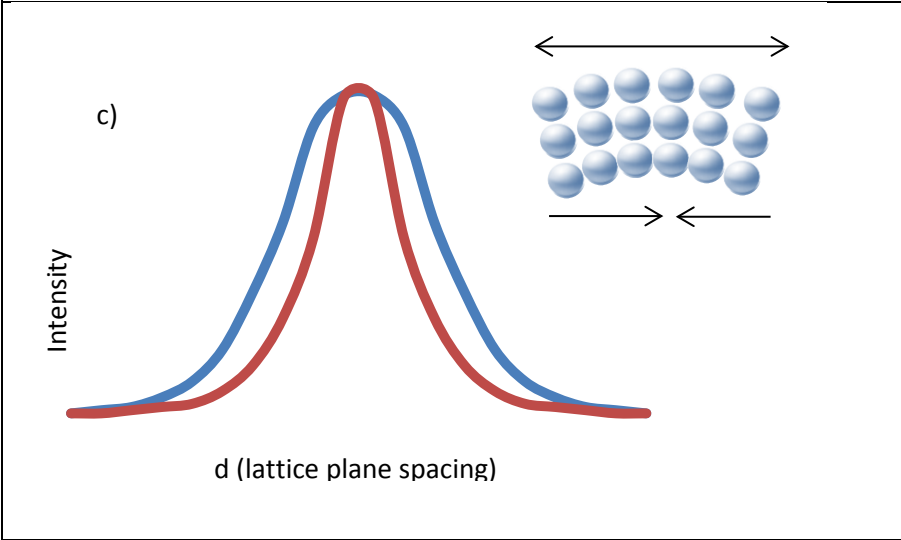
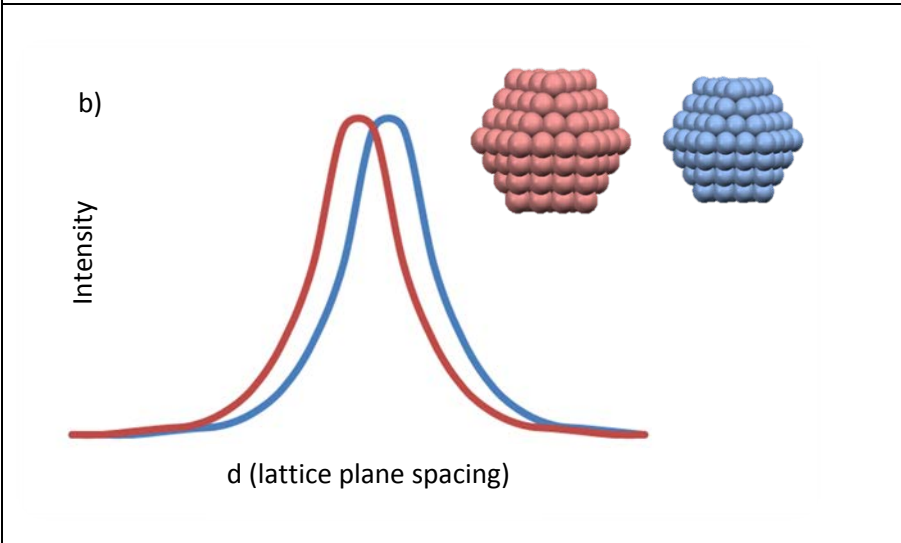
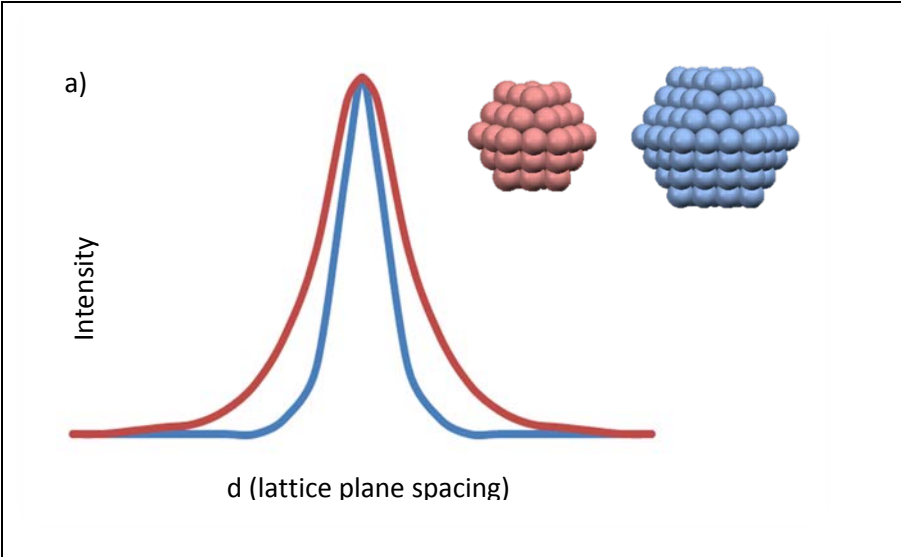
Correlation between surface strain and electro-catalytic activity has been proposed theoretically [144, 145] and demonstrated experimentally [97, 149]. The purpose of this work is to highlight and contribute to two, previously overlooked, aspects of this issue; Firstly, the multifaceted meaning of “strain” and its impact on XRD reflection analysis and secondly, the correlation between strain and catalytic activity for three different core metals. Here the aim is to build up a volcano-type activity-strain plot through demonstrating that the catalytic activity of Platinum is affected positively by lattice compression for Pt@Ni particles and negatively for Pt@Cu and Pt@Fe particles.

1.2. Predicting XRD reflections. The technique of choice to retrieve information on lattice properties is X-Ray Diffraction (XRD) [150]. XRD, in comparison to other techniques such as electron beam microscopy, holds the advantage of analysing large samples thus providing an average over a large number of particles. Commonly XRD is used to identify the crystal structure(s) in a sample and the crystallite size. However peak analysis is rarely performed to its full potential. In core-shell nanoparticle analysis in particular, XRD can provide valuable insight into the macroscopic structure of a nanoparticle and the lattice strain arising from its particular synthesis. Commonly peak shift and broadening larger than what can be ascribed to effects of crystallite size, are being overlooked in literature or referred to as an effect of mixing of metals [59, 104, 109, 150].

The intensity of a given reflection is largely determined by the form factor, i.e. the scatter from individual atoms, and the structure factor, i.e. the resultant wave from atoms in the unit cell. A core-shell particle consisting of two metals will result in scattering from the shell metal, the core metal and the interference between the two. The reflections from the shell will appear as those of a hollow sphere. In case the two constituting metals have a relatively large difference in atomic number Z , such as for Pt and Fe, the metal with the larger atomic number dominates the reflections to such an extent that the contribution from the metal with the smaller atomic number are not easily distinguished because its scattering intensity is a factor Z^2 smaller.

Particle size influences the peak width – a relation described by the Scherrer equation [131], illustrated in Fig. 2a. Furthermore, the smaller the particle the higher its Laplace pressure [151] which will lead to a compression of the particle and hence a peak shift to larger wave numbers, illustrated in Fig. 2b. Nano-sized particles will therefore have a different peak position relative to bulk material [121]. It can be assumed that a homogeneous internal pressure would act on a cubic lattice, however it is feasible that the pressure contributes to different amounts of strain in the various lattice planes resulting in different amount of shift for different peaks. Keeping in mind that particle size is determined both by the actual number of atoms making up the particle and the amount of lattice compression, both the peak position and the peak width might be affected.

Let us illustrate elongation strain by imagining a strip of a tensile metal. Pulling this strip of metal would cause elongation in the direction of the force and compression of the lattice in the vertical direction, shifting some peaks upwards and others downwards. Lattice compression would yield a peak shift towards higher angles meanwhile lattice elongation gives shift in the opposite direction (Figure 2b). If the strip would be bent the lattice would see an elongation and a compression simultaneously giving rise to a uniform peak broadening (Fig. 2c). Since no crystal is perfect due to its finite size, a broadening of diffraction peaks will, to a certain extent, always be present [121, 146]. A shear force, shifting successive lattice planes with respect to one another, causes the cubic lattice to deform into an orthorhombic lattice and causes peak shift or splitting (Fig. 2d).



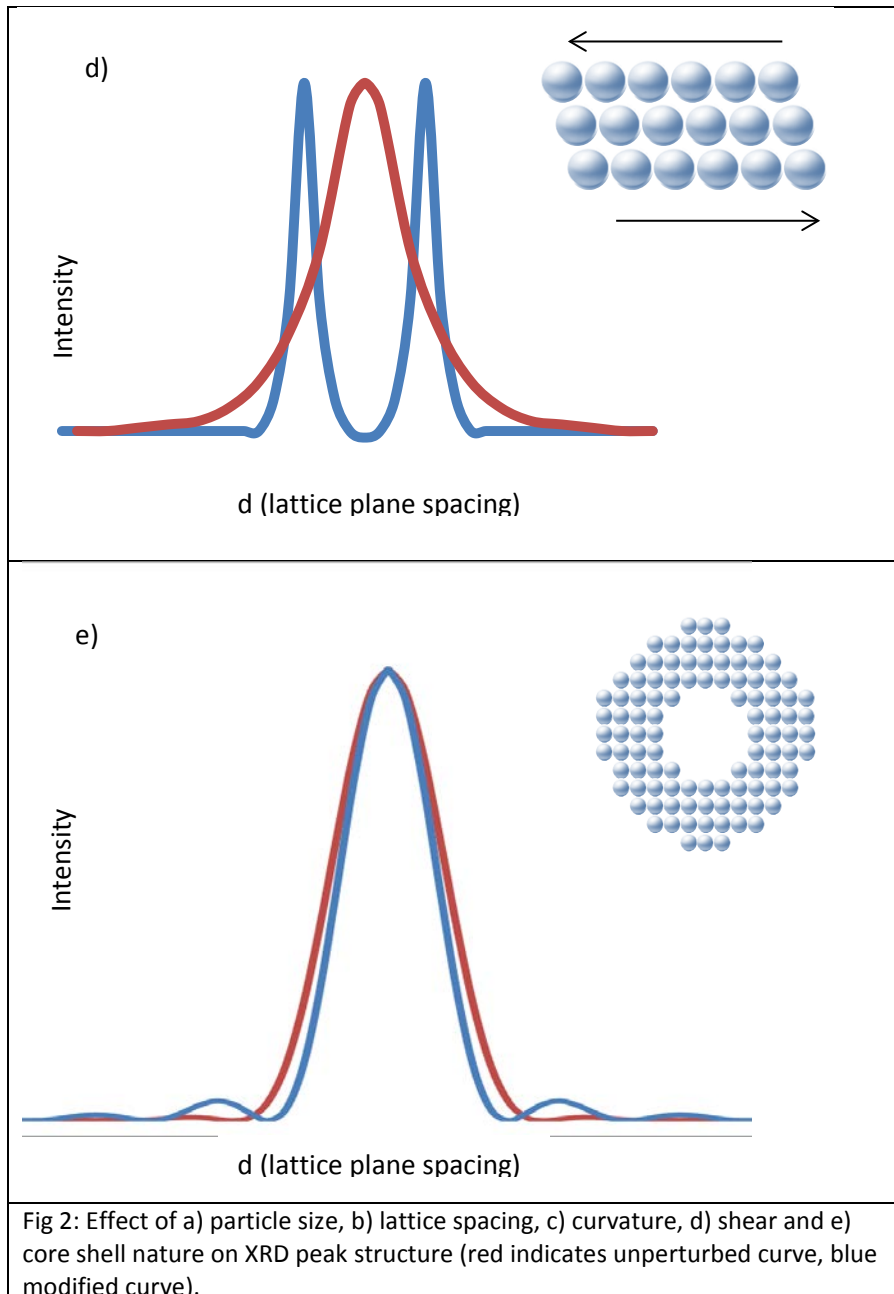


Fig 2: Effect of a) particle size, b) lattice spacing, c) curvature, d) shear and e) core shell nature on XRD peak structure (red indicates unperturbed curve, blue modified curve).

The Fourier transform of a certain geometrical structure, e.g. sphere or cube, describes the shape of the reflection. A hollow sphere or a shell around a, for XRD invisible, core would be described by the Fourier transform of a sphere (with diameter D_1) from which the centre (a sphere with diameter D_2) has been subtracted [152]. The shape of a hollow sphere (with shell thickness of $\frac{D_1 - D_2}{2}$) remains. The structure factor of such hollow sphere would result in a distribution with abnormally long tails compared to a solid sphere with the same diameter, taking into account that the oscillations in the tail even out if for a distribution of shell thicknesses [150]. This is illustrated in Fig. 2e, the cartoon being merely a rough sketch of reality.

The lattice constants of Pt, Fe, Ni and Cu are 3.920, 2.866, 3.524 and 3.615 Å respectively, hence, fitting Pt onto the core metal will cause lattice contraction. One monolayer of Pt on top of bulk Fe, Ni or Cu would theoretically generate a compressive strain of

$$\varepsilon_{ML} = \frac{d_{Pt} - d_{Me}}{d_{Pt}} \quad (\text{Eq. 1})$$

where d is the lattice constant. The peak displacement generated in the XRD diffractograms are relative to the Platinum lattice, hence it is useful that the formula similarly describes the strain of the Platinum lattice if it were to follow the core metal lattice. Throughout this paper strain means lattice contraction (reduction of interatomic distance) and to avoid confusion the numbers for strain are presented as negative numbers since it represent a reduction in lattice spacing.

4.3 Materials and methods

4.3.1 Instrumentation and Measurements.

The particle sizes were all determined using Dynamic Light Scattering (DLS) using a ZetaSizer Nano ZS from Malvern Instruments and Transmission Electron Microscopy (TEM) using a JEOL JSM 2012. With DLS the particle size is measured before the addition of carbon support whereas the particles are adsorbed on the carbon support when measured with TEM. The final composition of the particles was evaluated using Inductively Coupled Plasma Atomic Emission Spectroscopy (ICP-AES) by dissolving approximately 25 mg of the particles in Aqua Regia, diluting it with Milli-Q water to 50ml and analysing it using a PerkinElmer Optima 5300DV. Particle composition was also analysed with Energy Dispersive Spectroscopy (EDS) using a JEOL JSM-6010LA InTouchScope. All samples were characterized by X-Ray Diffraction (XRD) with Co $K\alpha$ radiation of wavelength 1.79 Å using a Bruker AXS D8 Discover.

To make sure that any peak displacement in XRD is not an artefact of axis offset – sample height in XRD – measurements with a calibration standard at lower and higher axis offset was made resulting in a maximum peak shift of $\pm 0.5\%$.

4.3.2 Electrochemical measurements.

Cyclic voltammetry (CV) and hydrodynamic voltammetry (HV) were performed in a standard single 3-electrode cell using a Reversible Hydrogen Electrode as reference electrode and a Pt mesh as counter electrode. A Rotating Disk Glassy Carbon Electrode (RDE) with a 5 mm in diameter glassy carbon disk and hence an electrode area of 0.198 cm² from PINE Research Instrumentation was used for the hydrodynamic measurements. To make the catalyst ink layers on the electrode 13 μ l of catalyst ink was drop caste on the disk, containing 6.5 μ g of catalyst material (i.e. carbon + core-shell particles) out of which 40-70 wt% was carbon. All experiments were conducted in a 0.1 M HClO₄ solution saturated with Ar for the cyclic voltammetry and O₂ for the hydrodynamic voltammetry using rotation speeds of 400, 900, 1600 and 2500 rpm [63]. Scan speed for CV was 50 mV and 5mV for HV.

Since the surface area of Platinum, A , covered by one hydrogen atom is proportional to the lattice constant squared, d^2 , for a cubic lattice, the relative change in area with lattice strain can be calculated according to Eq. 2, assuming that each lattice site is maximally occupied with one hydrogen.

$$\frac{\Delta A}{A} = \frac{d^2 - d_0^2}{d_0^2} \quad \text{Eq. 2}$$

where d_0 represents the unstrained lattice constant. If the lattice is strained, the lattice constant will be changed and hence the surface area per atom will change (see Table 1), bearing in mind that the assumption of one hydrogen per atom may at some point be lost for strained lattices.

Table 5 Predicted maximum strain ($\Delta d/d$) considering one monolayer of Pt on top of Fe, Cu and Ni (Eq. 1) and predicted decrease in ECSA ($\Delta A/A$) with lattice spacing (Eq. 2).

	$\Delta d/d$	$\Delta A/A$
Pt@Fe	- 26.8 %	- 60.7 %
Pt@Cu	- 7.8 %	- 16.2 %
Pt@Ni	- 10.1 %	- 21.2 %

4.4 Results

4.4.1 XRD response

Figure 4 presents the XRD patterns of some Pt@Cu, Pt@Ni, and Pt@Fe samples as well as pure Platinum particles prepared using the synthesis procedure described in Chapter 2. As expected, different core:shell ratios give rise to different amounts of peak shift representing lattice contraction compared to pure Pt particles. The relative lattice shift of the Pt in the core-shell particles with respect to that of pure Pt is interpreted as lattice strain and used to construct the abscissa of Fig. 1. Importantly, one Pt:Me ratio does not give rise to the same strain when the type of core metal is changed. The small peaks at $d=2.1 \text{ \AA}$ for Pt@Cu and Pt@Fe could not unambiguously be identified, likewise for the peak at $d=2.3 \text{ \AA}$ for Pt@Ni. They could possibly originate from interference between the two metals. Another possibility is impurities. The Pt@Ni sample shown in Fig 4 is the Pt@Ni sample with the highest activity and thinnest shell. For the samples with thicker shell no peaks at $d=2.3 \text{ \AA}$ were found. Due to the synthesis method and the voltammetric results any surface Ni atoms are not a likely cause of these additional peaks. It is not trivial to rule out that possible impurities or sub surface alloying between Pt and Ni in this particular sample have an influence on the catalytic activity but generally such influence is expected to be of marginal importance. The largest peak displacement (3%) was seen for the Pt@Cu (2:1) samples. These graphs were used to determine the lattice shift of the Pt on the core-shell particles and are used to construct the abscissa of Fig 7.

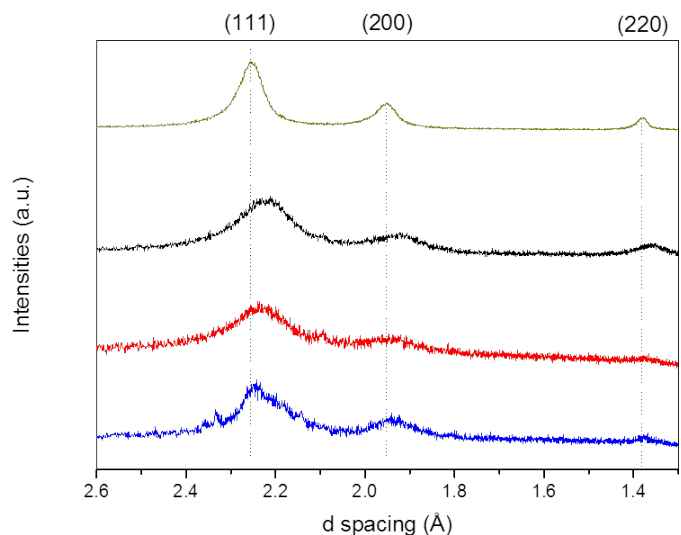


Fig 4 XRD result example of Pt@Cu (black), Pt@Fe (red) and Pt@Ni (blue) as well as pure Pt (green). The lines indicate the peak position for pure micro-emulsion made Pt nanoparticles and are intended as a guide to the eye.

In addition, samples with the most compressed Pt lattice also show the largest peak broadening i.e. a larger Full Width at Half Maximum (FWHM) value (Figure 5). Note that all particles, including pure Platinum, have a very similar particle size (see 3.2).

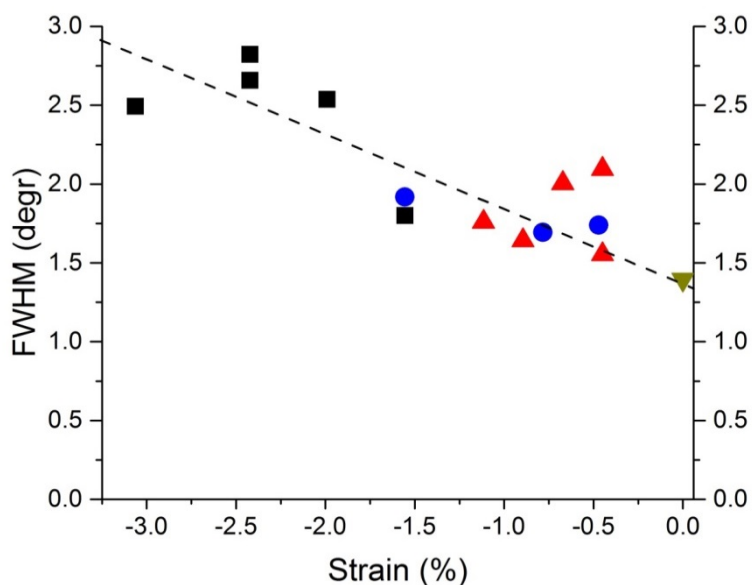


Fig 5 Peak broadening (Full Width at Half Maximum) relative to the peak replacement (strain in %) for four types of samples: Pt@Cu (black square), Pt@Ni (blue circle), Pt@Fe (red triangle) and pure Pt (green down-pointing triangle). All samples have similar particle size. The dashed trend line is a guide to the eye.

4.4.2 Catalytic performance.

Hydrodynamic voltammograms measured in oxygen saturated electrolyte show, despite slight agglomeration, onset potential values above 0.9 V for the oxygen reduction reaction. Although the exact mechanism of the oxygen reduction reaction is not yet fully explained, oxygen can be reduced via a 2-electron reduction pathway to H_2O_2 or via a 4-electron reduction pathway to H_2O , the latter being the preferred route in fuel cell applications [27]. Since Pt-based oxygen reduction electrocatalysts tend to predominantly favour the desired 4-electron reduction pathway, the selectivity in terms of reduction pathway of the catalysts has not been further studied here [15]. Due to non-ideal binding energies of the oxygen reduction intermediates to the Platinum surface, there will be an associated overpotential limiting the process from reaching the thermodynamic equilibrium potential of 1.23 V [53]. As a measure of the catalytic activity, the value of the current at 0.8 V was taken representing the region where the electrochemical reduction of oxygen is kinetically controlled. Interestingly, for the sample with the highest ratio Pt:Fe the kinetic current even outperforms that of pure Pt particles made in micro-emulsion.

The mass activity extracted from graphs including Fig. 6 for all particles were used to construct the vertical axis in Fig. 8.

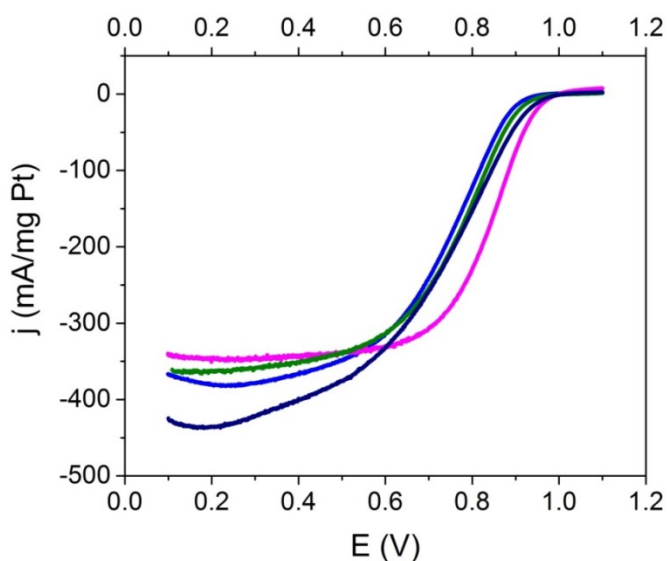


Fig 6 Mass activity of three core shell samples; Pt@Ni (blue), Pt@Fe (pink), Pt@Cu (green) along with pure Pt (black). All measurements are done in oxygen saturated 0.1 M $HClO_4$ at 900 rpm using a scan speed of 5 mV/s.

4.4.3 Activity vs strain

A plot of mass activity versus lattice strain reveals an exponential dependence where strain influences the activity negatively for Pt@Fe and Pt@Cu and positively for Pt@Ni.

For Pt@Fe particles and Pt@Cu particles an increased strain in the Pt lattice seems to decrease the catalytic activity whereas it has an improving effect for Pt@Ni particles, as illustrated in green in Fig 1. It is clear that the lattice strain is reduced as the Pt fraction in the particle – hence shell thickness –

increases as illustrated in blue in Fig 8. The thicker the Pt shell and the less strained lattice the larger the catalytic activity is for Pt@Fe particles and Pt@Cu particles, illustrated in red in Fig 8. On the contrary, a thin shell seems beneficial for the activity in Pt@Ni particles. The observation marked as a square in Fig 8 has been treated as an outlier since its position, even if repeated, deviates considerably from the general trends. Noteworthy, however, is that the largest strain among all samples prepared was achieved with this composition of Pt and Cu. Mass activity depends exponentially on strain and shell thickness, which is seen by the linear dependency in logarithmic scale in Fig 8. Strain and shell thickness on the other hand have a linear interdependency.

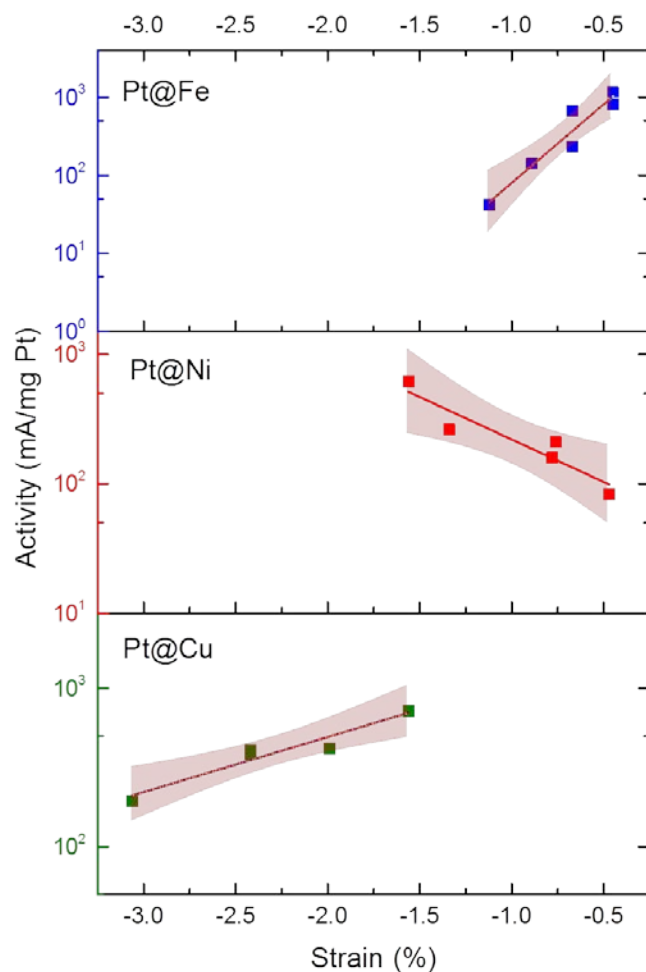


Fig 7 The exponential correlation between strain and oxygen reduction activity for the three different types of core-shell samples. Each observation is one unique particle sample for which activity has been measured using RDE and strain by using XRD. The fitted lines are a guide to the eye and the shaded area is the 95% confidence band.

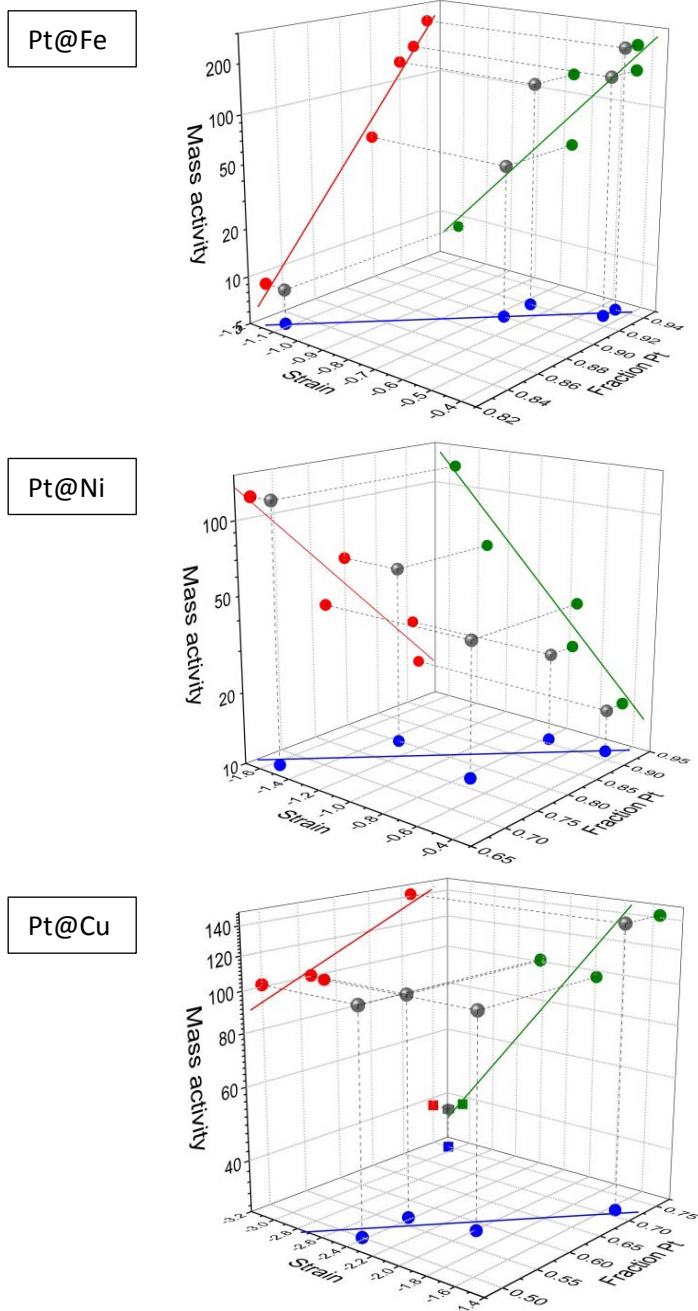


Fig 8 Pairwise correlations between mass activity (mA/mg Pt) and Pt fraction (red), strain (% relative to pure Pt) and mass activity (green), Pt fraction (1 for pure Pt and 0 for pure core metal) and strain (blue) and full correlation (black). Trend lines are discussed in text.

4.5 Discussion

4.5.1 Characterisation

The uniformity of the size-distributions allows us to discard specific peak broadening caused by size differences. Nevertheless, all core-shell type samples show peak broadening to a larger extent compared to pure Pt particles of the same particle size. The broadening increases proportional to the strain, as can be seen in Fig. 5. The broadening of the XRD reflections could be caused by the

distribution of different interatomic distances in the curved lattice, following the argumentation in Fig. 2c. Hence the FWHM can be used as a rough measure to interpret curvature. Any secondary shoulders due to a “hollow” structure (Fig. 2e) are too small to be resolved in our data.

It is also crucial to understand whether a hollow sphere acts like a single crystal or like crystal domains. In the case of micro particles there would most likely be grains making up the shell but for homogeneous nanoparticles the option of having a monodomain crystal becomes relevant. If the shell or solid particle is multidomain then the peak broadening will be more severe than what is predicted in terms of peak broadening due to size. Another situation would be that the crystal is single domain but exhibits internal stresses and strain to some extent [153]. Also this can give rise to peak broadening. If the particles were multi-domain, all peaks would most likely be lost since the broadening could flatten out the reflections completely. This is why the most likely scenario here is single crystalline Pt.

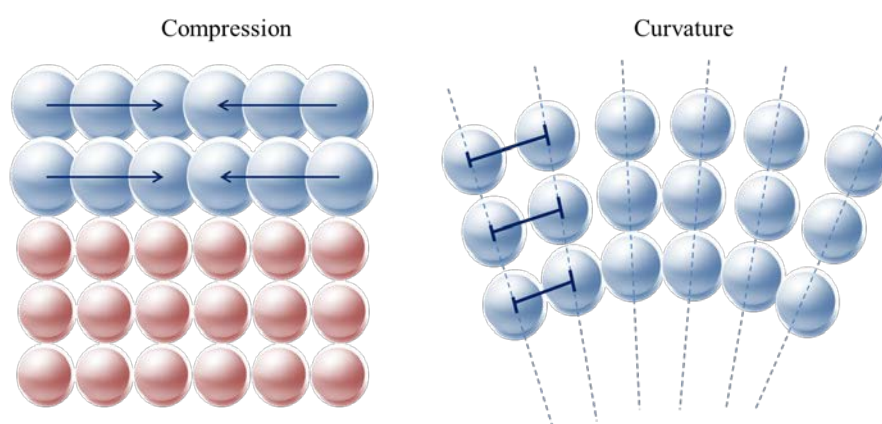


Figure 9 Core-shell structure in nano-particles give rise to geometric alterations of the crystal lattices. Here is shown the compression of the interatomic distance due to lattice mismatch and the effect of curvature in the lattice giving rise to a range of interatomic distances.

Secondly, most particles exhibit a significant shift of the Pt (111), Pt (200) and Pt (220) reflections towards higher 2θ angles compared to the expected positions of Pt and relative to the pure Platinum sample, due to the compressive strain arising from Pt being fit onto a core metal with smaller lattice spacing. Since strain contributes to both peak displacement as well as peak shape it would require extensive analysis to accurately and quantitatively build up a model describing the relation between particle composition and structure to strain.

We have assumed an isostatic pressure on cubic Platinum. This might or might not be true in which case the displacement of XRD peaks would not be of equal magnitude amongst the various crystal planes. To the extent of our work we have not seen signs of this.

4.5.2 Catalytic performance

The cyclic voltammograms for the core-shell samples show that Platinum is the surface dominating species, confirming the core-shell configuration. For up to 100 potential cycles there is little or no change in the voltammograms indicating no rearrangement or presence of transition metal atoms at the surface. Hence, no other metal than Pt is present in the shell.

The Electro-Chemically Active Surface Areas (ECSA) for some of the catalysts are smaller than expected compared to commercial Platinum. It must be remembered though that the calculation of ECSA is based on a number of assumptions well described in [148], including the presence of a set density of Pt atoms at the surface ($1.3 \cdot 10^{15} \text{ cm}^{-2}$), the completeness of the charge transfer assuming no alterations of the surface and issues arising with highly porous electrodes. Moreover, the adsorption and desorption of hydrogen is based on bulk Pt. These criteria might very well be compromised in the case of small particles with thin and strained Platinum shells. For these reasons activity is expressed in mass activity (mA/mg Pt) rather than specific activity (mA/cm² ECSA). One additional factor possibly affecting the surface area negatively is the presence of remaining surfactants on the catalyst surface, although the effect of remnant surfactant on catalytic surfaces has been ambiguously reported [21, 72, 154]. On the other hand, agglomeration of particles due to acid washing further keeps the surface area inferior.

Although the catalytic activities exhibited by our core-shell particles are slightly inferior to that of commercial Platinum, we see comparable or even a slight improvement in activity compared to pure Pt samples made in bi-continuous micro-emulsion. This is encouraging since there is still some performance to gain through maximizing the particle dispersion on carbon as well as surfactant removal in the synthesis procedure. Moreover, our aim was not to optimize our synthesis but to investigate the effect of strain on the activity.

4.5.3 Activity vs strain

The catalytic activity of a given metal – in this case Pt – is governed by a set of properties including its local geometric structure and electronic configuration [21, 155]. By creating particles with a core-shell structure it is likely that both these properties are altered, be it negatively or positively. The results in Fig. 1 strengthen the hypothesis of the two contributions: geometrical and energetic, both induced by shell thickness and core material. Furthermore, a change in interatomic distance in the Pt lattice alters the electron band structure and hence, compared to pristine Pt, an alteration in activity due to strain is to be expected. Such correlation has, however, been scarcely investigated due to the complexity of the strain contributions. As “strain” in our activity-strain graph, we have used only the contribution from lattice compression, measured as peak shift, since a fair deconvolution of peak shape is beyond the scope of this paper.

However, we have managed to generate core-shell particles with lattice strains ranging from 0.5% up to 3% and showed how the strain affects the ability to catalyse the ORR. For Pt@Fe and Pt@Cu we observe a decrease in activity with lattice strain and the contrary for Pt@Ni.

Since activity is largely controlled by the activation energy it strongly depends on the electronic state of the catalytic substrate [28]. Upon straining the catalyst lattice the activation energy is altered. There is no reason to believe that the unconstrained crystal lattice of the catalyst, Pt in this case, is optimal in activation energy for ORR so that any deviation would lead to deterioration. Hence, to a good approximation, we can assume that there is a linear relationship between activation energy and the lattice strain. It can be improved or worsened.

We attempt to decouple the contributions to the activity. On the one hand the contribution from a geometrical perturbation of the lattice, in other words strain, which is measured as peak displacement in XRD. On the other hand the energetic influence from the core metal, which is

measured as zero strain catalytic activity. The exponential variation of activity, A , with strain, δ , can be described as:

$$A = A_0 10^{\alpha\delta} \quad \text{Eq 3}$$

A_0 is the activity at zero strain and represents the contribution from the core metal. α is the linear variation of activation energy with strain (δ). The slope, α , and the intersect at zero strain, A_0 , are presented separately in figure 10-11. The exponential dependence of activation energy on strain is evidenced in Fig. 10. Furthermore, the Pt@Fe-type particles are the most negatively affected by strain.

The zero-strained activity, A_0 , in Fig. 11a is an extrapolated value since it is impractical to make Pt shells with infinitely little strain. However, the results predict an increase in the catalytic activity for unstrained Platinum for Pt@Cu and Pt@Fe. Such lattice would require a flat surface in the order of micrometres or more and in that case the benefit of large surface area for the particles would be lost.

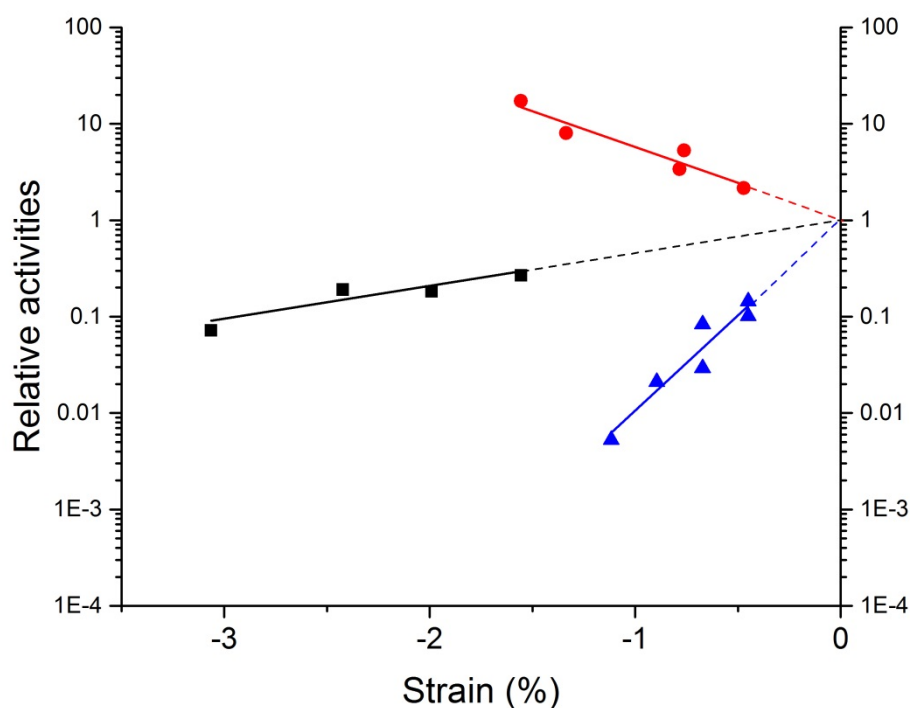


Fig 10 The effect of strain on the catalytic activity, where Pt@Ni (red), Pt@Cu (black) and Pt@Fe (blue). Relative activity is here defined as A/A_0 , where A_0 is the activity (mA/mg Pt) extrapolated to zero strain (induced by lattice mismatch).

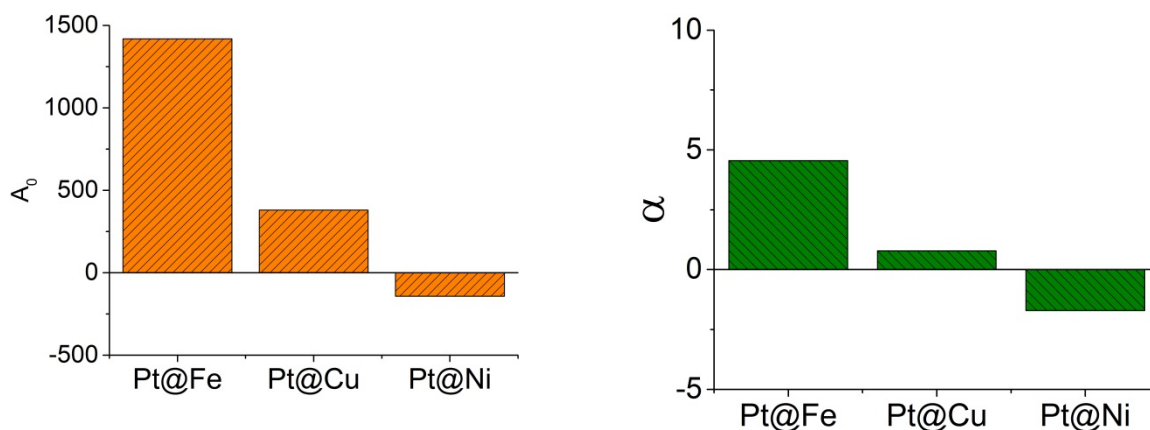


Fig 11 Separation of the metal effect A_0 (orange) and the strain effect (green) on the catalytic activity for Pt coated metal particles.

In this manner we can extrapolate to zero strain, i.e. zero geometrical effect, to obtain the pure energetic effect. Nevertheless, the energetic contribution and the geometric contribution to the overall catalytic behaviour of a specific catalyst are closely intertwined – both are consequences of electronic changes. It is however useful to understand the contributions that determine the catalytic behaviour in order to fine-tune it. Our results in Fig 8 and Fig 11 are a gesture to disentangle these effects.

4.6 Conclusions

By means of the core-shell particle synthesis described in this paper we were capable of demonstrating that the catalytic activity of the resulting nanoparticles can be tuned by surface strain and core material.

We predict the way core-shell particle structure and different types of strain affect the reflections in XRD. By measuring peak displacement in XRD the lattice compression, hence strain, could be estimated. We have found an exponential dependence of the activity on the strain – a negative such for Pt@Ni and a positive such for Pt@Cu and Pt@Fe.

Combining crystallographic measurements with catalytic activity measurements led us to conclude that the catalytic activity is affected by (at least) two effects: the geometrical effect due to lattice strain as well as the energetic effect on band structure of the shell metal caused by the interplay between the core and shell metal, for which the exact mechanism we leave for theoreticians to study. This is nevertheless a first systematic study of this behaviour.

Yet another result stressing the point that there is more information to gain from XRD analysis is the dependence of peak broadening on strain. We have shown that, for core-shell particles, the peak broadening in XRD is not only a result of particle size, but also varies systematically with the shell thickness, i.e. the strain. Here strain arising from curvature could be the dominating effect, suggestively shown by Fig 2c. It becomes evident that Fourier deconvolution of measured peaks, albeit an experimental challenge, becomes an important tool for understanding the real nature of

core-shell type particles. The peak shift and broadening, quantifying to a certain extent the lattice strain and curvature respectively, represents the geometric alteration of the Pt lattice.

Furthermore, standard electrochemical methods may represent properties of core-shell electrocatalyst particles poorly when operating outside assumptions of standard Platinum surfaces.

Manipulating Pt to shift its position in the Volcano plot opens up a new approach in designing catalyst particles. As an extension to this work, other metals than Pt could be studied and possibly take Platinum's place as the most active oxygen reduction catalyst.

5 The effect of magnetic field on catalytic properties in core-shell type particles



5.1 Abstract

Magnetic field effects can provide a handle on steering chemical reactions and manipulating yields. The presence of a magnetic field can influence the energy levels of the active species by interacting with their spin states. Here we demonstrate the effect of a magnetic field on the electrocatalytic processes taking place on platinum-based nanoparticles in Ar and O₂-saturated electrolyte. We have identified a shift in the potentials representing hydrogen adsorption and desorption, present in all measurements recorded in the presence of a magnetic field. We argue that the changes in electrochemical behaviour are a result of the interactions between the magnetic field and the unpaired spin states of hydrogen.

5.2 Introduction

Our aim is to explore how the catalytic behaviour of a specific electrochemical process can be altered, and hence, better understood. Previously in this thesis this was done by means of lattice spacing manipulations. We are here considering magnetic fields as a handle to influence electrochemical processes. Subatomic particles, like electrons, have mass, spin and charge. It is fair to assume that at least one of these properties – spin – can be perturbed by the presence of a magnetic field. Spin is intrinsic and gives rise to a magnetic moment that can be manipulated.

Steiner et al were the first to compose a bird's-eye review on magnetic effect on chemical reactions, including examples like magnetic fluorescence quenching, photo-addition of SO₂ to pentane, thermal decomposition of organic peroxides, reactions of alkali-metal alkyls with alkyl halides etc. [156]. Furthermore the review refers to a variety of reports on magnetic field effects on photophysical phenomena in (organic) molecular crystals, such as luminescence and photoconductivity. Even examples of simple experiments taking place between two laboratory magnets in which the reaction rate between organic radicals were measured proved to show a remarkable increase in the reaction rate [157]. As described by Steiner et al, most magnetic field effects in chemical processes take place in liquid solutions, mostly as a result of radical pair mechanism [156, 158]. In gas phase reactions on the other hand, the radical geminate re-encounter is unlikely and in solid phase reactions radical pairs do not separate easily. Shovkovy et al presented a review of a theoretical approach to magnetic field effects on chemical reactions [159]. Torun et al describe how the existence of a local magnetic moment of RuO₂ catalyst surfaces conserves the angular momentum and enables the production of magnetic oxygen from non-magnetic water [43].

For electron transfer reactions reports are scarcer. One of the first examples were presented by Periasamy et al, studying the electron-transfer reaction between diazabicyclooctane (DABCO) and fluorenone triplet in propylene carbonate [160]. For magnetic field effects in electrocatalysis there are even less reports. Leddy and co-workers are to our knowledge the only group working on magnetically modified electrodes with the purpose of enhancing electron transfer kinetics. They studied the magnetic field effect on Hydrogen Evolution Reaction (HER) on non-catalytic surfaces. Furthermore, they studied oxidation of CO₂ on a magnetically modified platinum electrode. The electrodes were made with magnetic micro-particles attached to the electrode surface, so that it could sustain a permanent magnetic field. Their studies show that oxidation of carbon monoxide at such modified Pt electrode surfaces are considerably altered compared to electrodes without magnetic micro-particles, through spin polarization [161]. The oxidation of carbon monoxide occurred at 600 mV lower overpotential. The enhancement of the electron transfer rate is claimed to originate from the suppression of entropy of the electron spin and hence a lowered activation barrier.

Jonsson et al. studied the effect of magnetic states on the reactivity of an iron surface using Density Functional Theory (DFT) calculations. Their results suggest that the charge-transfer between the catalyst surface and the adsorbate is strongly affected by spin-structure. In their study H₂ and CO adsorption and dissociation was modified by changes in spin-structure [162].

In this chapter we present our study on the effects of an external magnetic field on the electrocatalytic processes taking place on four platinum-based electrocatalysts. For this purpose, we have integrated strong magnets into the shaft of a Rotating-Disc Electrode and record the

electrochemical processes on Pt in Ar- or O₂ saturated acid electrolyte, in the presence and absence of a magnetic field. Due to the unpaired spin states in hydrogen as well as in oxygen, these species respond to a certain extent to a magnetic field.

The main electrochemical processes taking place in these conditions are firstly – if oxygen is present – Oxygen Evolution Reaction (OER) and Oxygen Reduction Reaction (ORR) with a thermodynamic equilibrium potential of 1.23 V vs SHE, see Fig 1. Oxygen adsorption and desorption proceeds these reactions. The ORR and OER are more thoroughly described in Chapter 1 of this thesis. The region in between the surface oxide formation/reduction region and the hydrogen adsorption/desorption region is usually referred to as the “double layer region”. In this region no faradaic processes take place but only capacitive processes [163]. Secondly, the Hydrogen Evolution Reaction (HER) and the Hydrogen Oxidation Reaction (HOR) have a thermodynamic equilibrium potential of 0 V vs SHE and characterize the features in the cyclic voltammogram around 0 V. When the potential is kept >0 V (vs SHE) only Hydrogen adsorption and desorption takes place, often referred to as H under-potential deposition (H_{upd}).

Hydrogen adsorption and desorption

Adsorption can be sorted as: 1) molecularly chemisorbed, 2) atomically chemisorbed and 3) molecularly physisorbed [15, 28, 164]. Molecular physisorption refer to electrostatic interactions between Pt and molecular H₂, where no electrons are shared and no dissociation occurs. As described elsewhere [164] molecularly chemisorbed H₂ is highly unlikely. H₂ will immediately dissociate implying that chemisorption of H₂ on Pt is atomic to the largest part.

The mechanism of hydrogen adsorption and evolution on platinum has been extensively studied [17, 19, 165]. This process is fast and electrochemically reversible and the equilibrium surface coverage depends on the electrode potential. Cyclic voltammograms recorded for platinum in acidic electrolyte show distinctive peaks at 0 – 0.4 V vs RHE. There seems to be a general consensus concerning the origin of the most prominent peaks [19, 21, 163, 164, 166], located around 0.125 V and 0.27 V, representing the (110) and (100) step sites on Pt, in the following manner described in detail by Diaz-Morales et al [166]:



where *hkl indicates a free site on the Pt surface with hkl Miller indices.

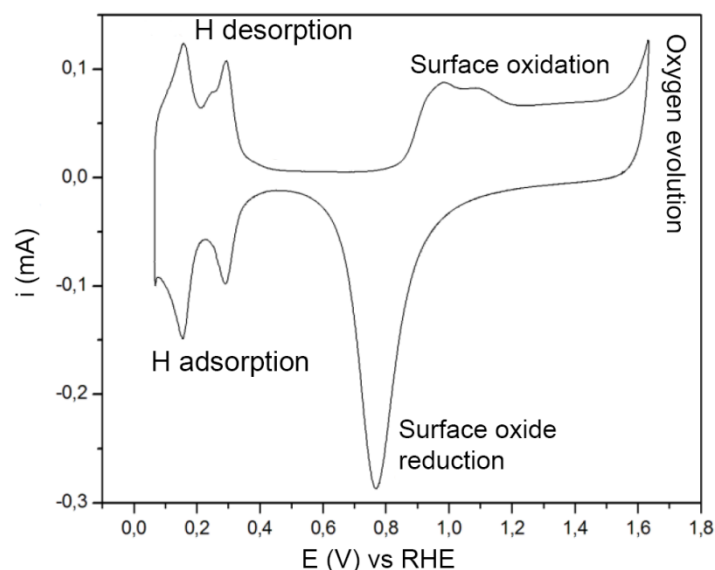


Fig 1 The typical features of cyclic voltammetry on Pt catalysts in acidic electrolyte. Adapted from Ref [163]

5.3 Materials and Methods

For this study three electrocatalysts were made according to our micro-emulsion based core-shell synthesis described in Chapter 2.3: Pt@Fe nanoparticles, Pt@Cu nanoparticles and pure Pt nanoparticles made in micro-emulsion. Further, commercial Pt on carbon (60wt% Pt on Vulcan XC-72R, Johnson Matthey, UK) was used.

5.3.1 Setup

To be able to achieve a magnetic field, as strong and as close as possible to the catalyst layer, the rotating disk electrode was modified and perfected in many steps. A Pine Instrument RDE electrode with removable glassy carbon disk of 5 mm was used as starting material for the build-up of an electrode with the option to be both magnetic and non-magnetic. To accommodate the magnets right in between the glassy carbon disk and the spring-loaded shaft, both the disk and the shaft had to be reduced in size. The length of the glassy carbon disk was reduced from 5 mm to 2 mm by ultra-fine polishing, thanks to *Surface Preparation Laboratory, Zaandam, NL*. A new, shorter shaft was made, keeping the spring-loaded tip to ensure good electrical contact with the magnets. The “cavity” inside of the modified RDE electrode was made such that it could accommodate either only magnets, only a non-magnetic brass cylinder or half-half magnets/brass as a crude way of varying the magnetic field strength. See Fig 2 for a schematic illustration.

The magnets (*Supermagnets, Dresden, Germany*) are Neodymium magnets of size 5mm in diameter and 2,3 and 5 mm long cylinders, coated with nickel. The magnets are of grade N52 which correspond to a magnetic field strength of approximately 0,4 T.

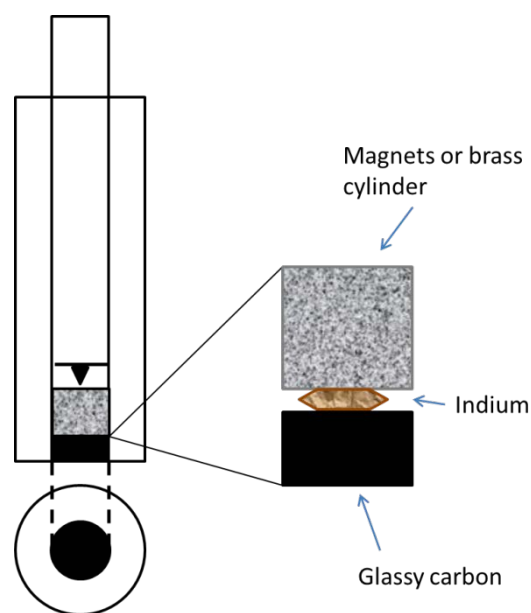


Fig 2 A schematic picture of the modified RDE shaft

5.3.2 Experimental

The catalyst samples, Pt@Fe, Pt@Cu and pure Pt, were prepared and characterized according to our micro-emulsion synthesis of core-shell particles described in Chapter 2.3. In order to get the most accurate comparison between activity measurements made with the magnetic electrode configuration relative to the non-magnetic configuration, the measuring sequence proved to be crucial. Two consecutive measurements – with and without magnetic field – had to be made either on two different ink layers and running the risk of having differences between the layers, or on one single layer in which both measurements with magnets and brass cylinder were done on the exact same layer. In the latter case the risk is that the layer gets slightly damaged upon switching the interior of the electrode, since it involves moving the glassy carbon disk. Furthermore, there is a risk that the potential cycling permanently changes the catalyst through the sets of measurements, in other words, a “memory effect”. A needle is used to push the catalyst coated glassy carbon disk into the PTFE holder upon removal/insertion of magnets into the shaft. “m” represents magnetic configuration and “b” represents brass cylinder, i.e. non-magnetic configuration in the figures. Table 1 explains how the measurements were labelled according to magnetic configuration and order.

For all electrochemical measurements, an Autolab PGSTAT 20 potentiostat was used, along with a 3-electrode cell and a Rotating Disc Electrode (RDE) from Pine Instruments with a 5 mm in diameter glassy carbon disk and hence an electrode area of 0.198 cm^2 . The working electrode were prepared by thoroughly polishing the glassy carbon disk with 1.0, 0.3 and $0.05 \mu\text{m}$ alumina particle polishing suspensions, rinsing in between each step. Any residual polishing medium was cleaned off in an ultrasonic bath. An ink was made by mixing 6.0 mg of catalyst powder (i.e. carbon + core-shell particles) with $4.56 \mu\text{l}$ Nafion suspension (5wt%) and 12 ml isopropanol. The ink was mixed using an ultrasonic bath. To make the catalyst ink layers on the electrode $13 \mu\text{l}$ of catalyst ink was drop casted on the disk. Cyclic voltammograms recorded in Ar-saturated electrolyte were measured at scan speeds of either 50 mV/s or 100 mV/s. Otherwise the scanning procedures for cyclic voltammetry and hydrodynamic voltammetry are the same as described in Chapter 2.3.

Table 1 illustrates an example of how the measurements were executed and how they were labelled accordingly.

	RDE configuration	Label	Pt@Fe	Pt@Cu	Commercial Pt	BME Pt
1 st ink layer	1. Magnetic	m1	CV/HV/Mic- roscopy photo	→		
	2. Non-magnetic	b2				
	3. Magnetic	m3				
2 nd ink layer	1. Non-magnetic	b1				
	2. Magnetic	m2				
	3. Non-magnetic	b3				

5.4 Results

Sample preparation

Each time the glassy carbon is being pushed into the PTFE holder by the needle, the geometrical area loss estimated by optical microscopy is approximately 1-5%, see Fig 3 for an example. This loss is inevitable unless the architecture of the electrode setup is completely altered.

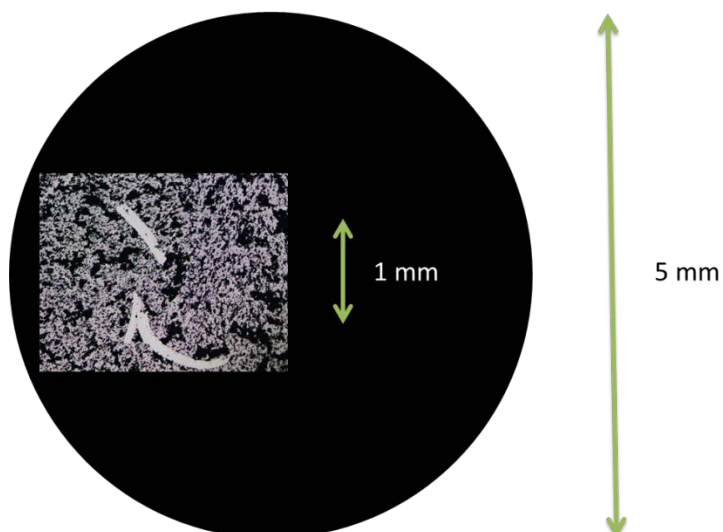


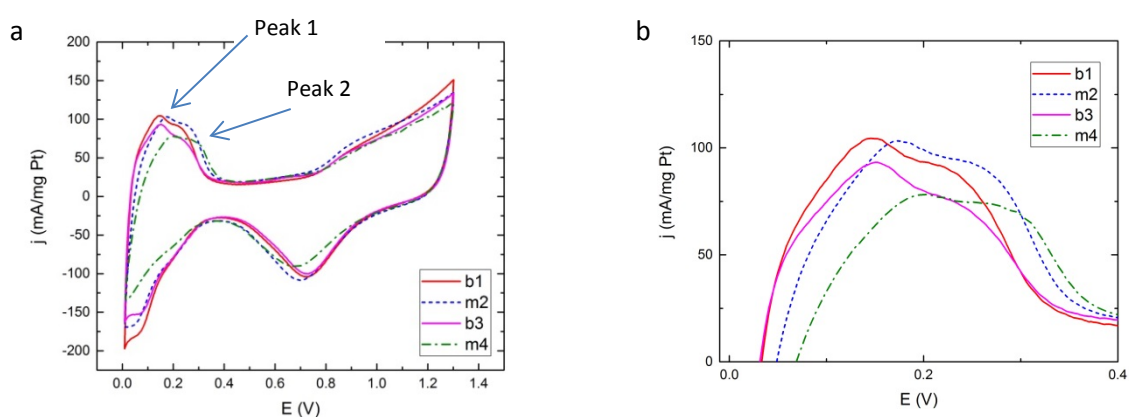
Fig 3 Photo of the scratches made when pressing down the glassy carbon disk into PTFE holder after switching configuration. The black circle represents the relative size of the glassy carbon disk.

Cyclic voltammetry

In the cyclic voltammograms in Fig 4 a loss in catalyst surface area, estimated by hydrogen adsorption and desorption peak areas, is observed upon switching configuration. This is, at least partially, due to the small damage to the catalyst layer arising from pushing the glassy carbon into the PTFE holder. The ECSA and ECSA loss was calculated according to commonly used methodology described first by Trasatti et al [148]. As an example, in a measurement of the sample “Pt@Fe” (Fig A1 in Appendix) the ECSA amounts to: $m_1=70\text{m}^2/\text{g}$, $b_2=62\text{m}^2/\text{g}$ and $m_3=53\text{m}^2/\text{g}$. The calculation of specific activity is based on these values. The loss estimated by ECSA is larger than the area loss estimated with optical microscopy.

Cyclic voltammograms for Pt@Cu, Pt@Fe and pure Pt made in bi-continuous micro-emulsion are presented in Fig A1-2 in Appendix, the only prominent result being the decrease in current density upon switching between the two configurations. The plots illustrate similar peak features in magnetic as well as non-magnetic configuration.

On the contrary, in cyclic voltammograms using commercial Pt as catalyst the hydrogen adsorption and desorption peaks are more prominent since the particles are better dispersed on the carbon support. Not only are they higher in relative terms but a behavioural difference between magnetic configuration, “m” and non-magnetic configuration, “b” (for brass) is unfolding. Although the number of different ink layers analysed with a sequence of magnetic and non-magnetic measurements are limited to approximately 10, each and every voltammogram contribute to a pattern of peaks shifting to higher potentials when scanning towards more oxidizing potentials, and vice versa, when a magnetic field is present, independent of measurement sequence. Figure 4 display voltammograms for samples measured at both 100 mV/s scan speed and 50 mV/s, using different measurement sequences. In Figure 4c the measurement order is magnetic-nonmagnetic-nonmagnetic in order to rule out any contribution from the configuration switch itself. Peak positions remain the same between “b2” and “b3”. A small shift in the position of oxygen desorption is visible in some measurements. In this initial study the focus has however been on the hydrogen region.



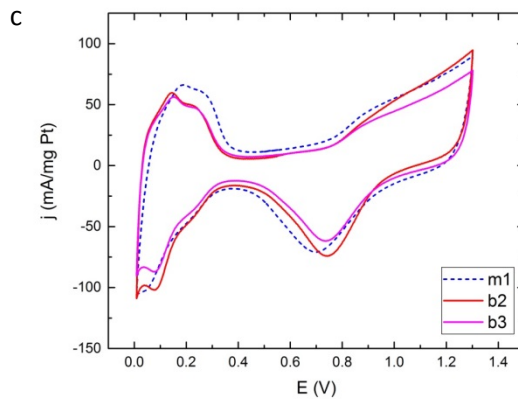


Fig 4 Cyclic voltammograms for Ar-saturated electrolyte for a) commercial Pt at 100 mV/s, b) close-up on the hydrogen desorption region and c) commercial Pt measured at 50 mV/s. Peak 1 corresponds to the desorption of hydrogen from Pt (110) sites and peak 2 represents desorption from Pt (100). The legend refers to the measurement sequence (1-4) and magnetic (m) or non-magnetic (b) measurement configuration as explained in Table 1.

Hydrodynamic voltammetry

After each measurement in Ar-saturated electrolyte, hydrodynamic voltammetry was carried out analysing the mass activity and specific activity of each configuration for each catalyst layer.

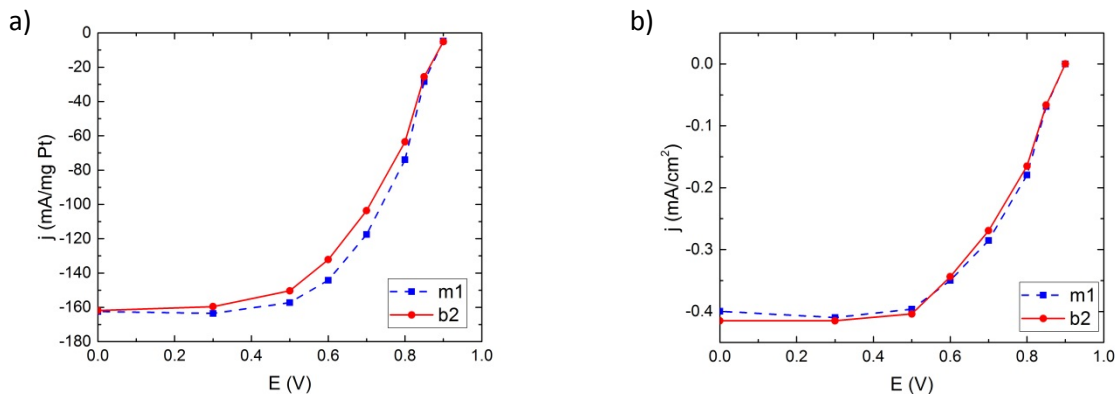


Fig 5 Hydrodynamic voltammograms for commercial Pt illustrating the catalytic activity for oxygen reduction in the two different magnetic configurations, calculated both as a) mass activity and b) specific activity.

An obvious and expected effect of the loss of catalyst is reflected in the loss of mass activity between the measurements, illustrated in Fig 5 as an example and in Appendix. If the total electrochemically active surface area of the layer is taken into account the measurements – magnetic and non-magnetic – overlap to a great extent. As results suggest, no significant difference in catalytic activity was detected between magnetic and non-magnetic measurements.

5.5 Discussion

The largest contribution to the errors in the measurements is the contact resistance upon switching between magnetic and non-magnetic configuration for a single layer. It is however crucial to perform both types of measurements on a single layer since the influence of the fabrication and permanent change to the catalyst during measurements cannot be ignored.

The loss of ECSA in percent between measurements is disproportionately large compared to the observed catalyst layer loss observed by microscope. However, ECSA loss throughout a sequence of measurements does not vary significantly between catalyst layers. As discussed in Chapter 4 it is problematic to use ECSA as an estimate for surface area on non-standardized surfaces. It can however serve a purpose as to estimate – within a single catalyst – the relative surface area. The catalyst loss calculated using ECSA is possibly more reliable than the loss estimated by microscopy, since specific activity plots seem to overlap.

Commercial Pt has the highest ECSA which means any effect would be most visible in this sample. Although the peak positions in the other samples do not display a clear shift, they are not countering the result from the commercial platinum. As an attempt to quantify the peak shift in commercial Pt samples, peak deconvolution using two Gaussian curves fitted to the data in OriginPro was carried out, see appendix and Fig 6 for an example. Since the hydrogen desorption peaks provided more prominent peaks, they compose the basis for such analysis. Although the adsorption peaks seemingly follow the same trend, a statistical assessment has not been made using that set of data.

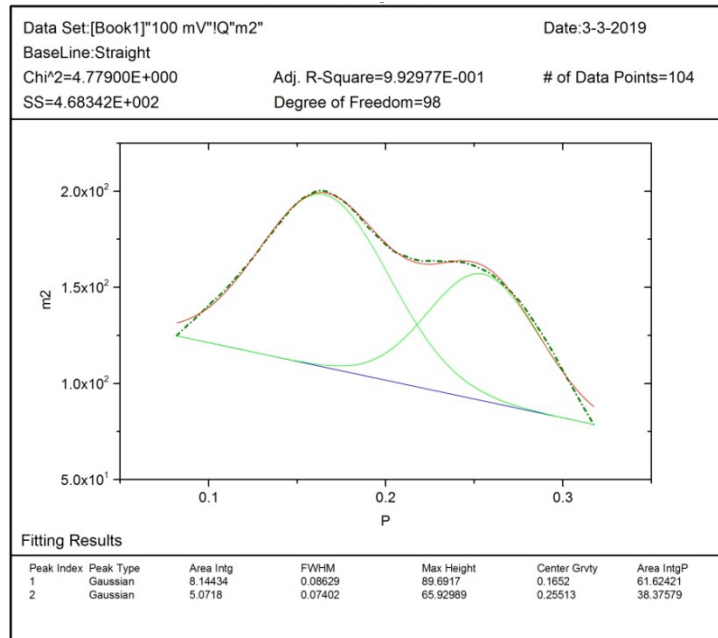


Fig 6 One example of peak fitting of hydrogen desorption peaks in OriginPro

The positions of the two peaks as a function of measurement order are illustrated in Fig 7. In general peak positions are shifted to higher potentials when a magnetic field is present. When the configuration is “switched” from magnetic to magnetic (i.e. glassy carbon including the catalyst layer

was removed and refitted again without changing the magnets for the non-magnetic cylinder) or non-magnetic to non-magnetic the peak positions do not show as much of a peak shift. Such measurements give an idea of the error in terms of peak positions in absence and presence of magnetic field *within one catalyst layer*. These data points are however too few to determine a reliable standard error. Another source of error arises from the reproducibility *between different catalyst layers*. This error is expected to be relatively large. As an example, two measurements named m1 (where “1” denotes the sequence number) from different catalyst layers should ideally overlap, but as illustrated in Fig 6, this is not the case. Nevertheless, the relative shift in peak position upon switching configuration is most relevant when compared with a measurement of the *same* layer.

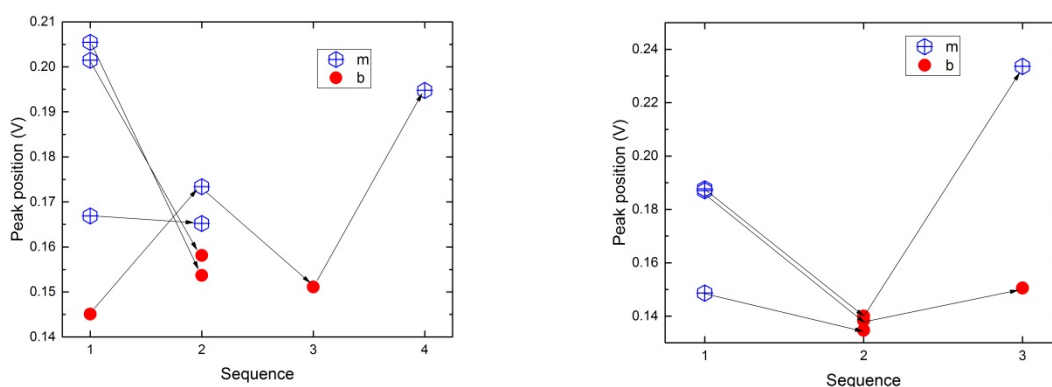


Fig 7 a) Peak position as a function of the measurement order for hydrogen desorption peak 1 for commercial Pt samples measured at 100mV/s, where “m” = magnetic configuration and “b” is non-magnetic configuration. The arrows connect the measurements done on one same layer.
 b) Peak 1 positions for samples measured at 50mV/s. For peak positions of peak 2, see appendix.

As a summary of all measurements the heights and positions of peak 1 are displayed in Fig 8. Magnetic and non-magnetic measurements clearly form two distinct clouds where the peak positions distinguish the two. The peak heights on the other hand do not separate the two configurations.

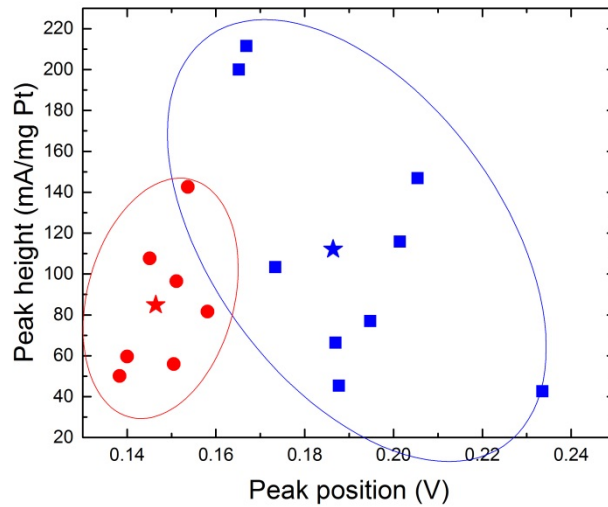


Fig 8 Peak position and peak height for desorption peak 1, where blue square=magnetic configuration and red circle=non-magnetic configuration. The stars represent the means (b: 0.146 ± 0.008 ; 84.86 ± 33.38 and m: 0.186 ± 0.024 ; 112.04 ± 62.76). The ovals provide a guide to the eye.

When performing a Two Sample t-Test where the threshold for statistical significance $\alpha=0.05$ is chosen, on the dataset of peak positions (both peak 1 and peak 2) for “m” and “b”, the means and population variances are significantly different between m and b. The average value for peak positions for peak 1 in magnetic configuration is $0.186 \text{ V} \pm 0.024$ and $0.146 \text{ V} \pm 0.008$ for non-magnetic configuration, illustrated with a star in Fig 8. This leaves a shift of approximately 0.04 V . The relative distances between the two peaks are presented in Fig 9. The means and variances are not significantly different in a Two Sample t-Test. Obviously, due to the small sample population the statistics has limited quality. However, this is an effort to disentangle the effect of the magnetic field on a limited dataset.

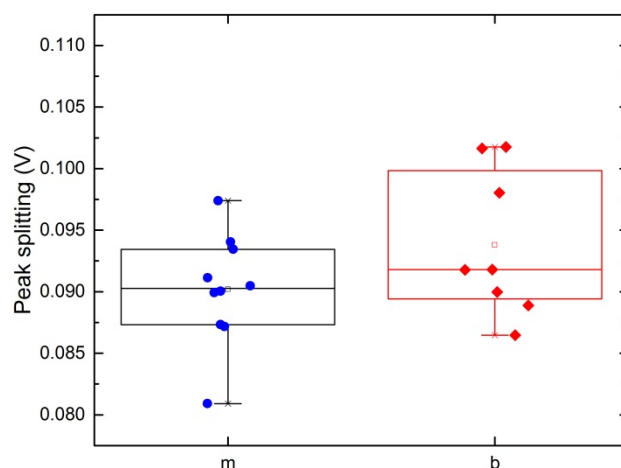


Fig 9 Peak splitting. A small difference between the two configurations is visible but not statistically significant.

The shift in peak positions suggestively caused by the presence of a magnetic field is small but however presents in all (commercial Pt) samples for various scan speeds. Our limited study on electrocatalytic behaviour with and without the presence of a magnetic field suggest that the desorption of H from the Pt surface is slowed down in the presence of a magnetic field.

In these experiments the surface is magnetized or non-magnetized. Any magnetic effect on the potential must be related to the spins of some active species interacting with the field. Hydrogen adsorption and desorption on Pt are two processes in our system. H_2 itself has two magnetic spins, one of the electron and one of the proton, whereas H^+ only have spin $\pm \frac{1}{2}$. In H_2 the + 1 and - 1 spin state will respond to the magnetic field whereas the antiparallel spin state does not interact with the magnetic field. This implies that 50% of the hydrogen is interacting with the magnetic field and 50% is not. As an effect, the binding energy of the H to the Pt surface is changed and that is what is observed in this study. However, if the energy levels in the atoms or molecules are changed by applying a magnetic field through the Zeeman effect the picture might change and the I-V curve peaks no longer represent what would be the case without a magnetic field. An in-depth analysis of the mechanism, however, is beyond the scope of this study. Nevertheless, it is, to our knowledge, the first experimental study discussing the effect of an external magnetic field on hydrogen adsorption on an electrocatalyst. Our results point in the same direction as predictions from calculations presented in [162].

5.6 Conclusions

We propose that the changes in the electrochemical behaviour observed in this study are due to the interaction of the magnetic states of hydrogen with the catalyst and that this causes a shift in the potentials for the hydrogen adsorption and desorption. At least some states of hydrogen are magnetic – so we presume that the electrochemical processes are influenced by the magnetic sets of hydrogen.

With the current setup and magnetic field strength, a clear and significant effect of magnetic field on the catalytic activity, either onset potential or kinetically limited current, towards oxygen reduction reaction has not been detected or does simply not exist.

Appendix Chapter 5

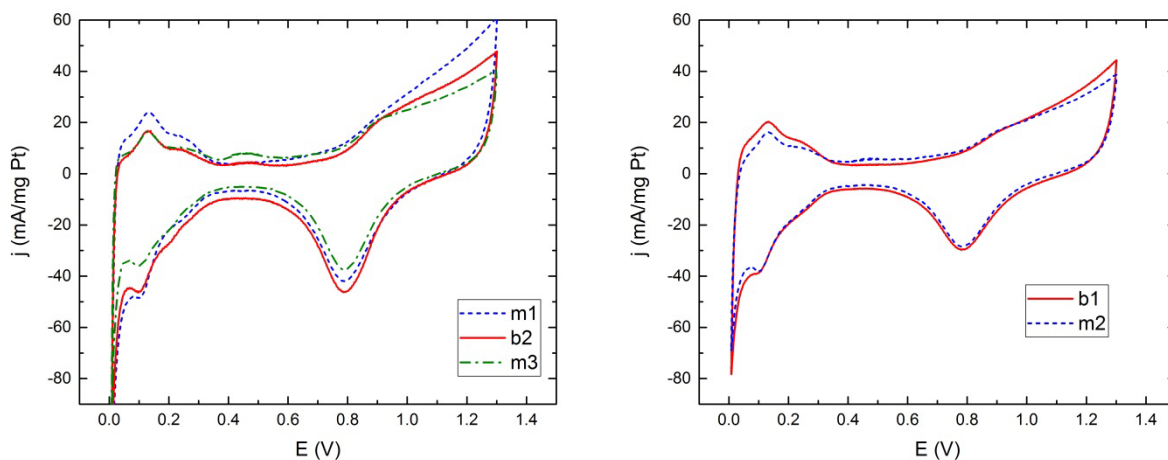


Fig A1 Cyclic voltammograms in Ar-saturated 0.1 M HClO₄ electrolyte with Pt@Fe as catalyst. The two plots represent two different catalyst layer for which the catalyst layer in voltammogram a) was measured firstly in the magnetic configuration (“m1”), secondly non-magnetic configuration (“m2”) and thirdly with magnetic configuration again (“m3”). In voltammogram b) the layer was initially measured in non-magnetic configuration and then in magnetic configuration. Each set of measurements consisted of CV:s in Ar and a set of HV:s in O₂.

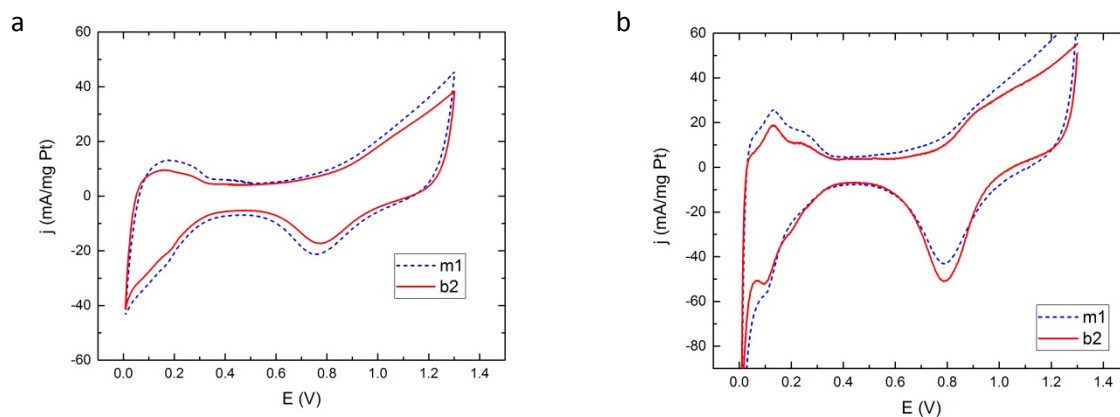


Fig A2 a) Pt@Cu at 50mV/s and b) Pt BME at 50 mV/s

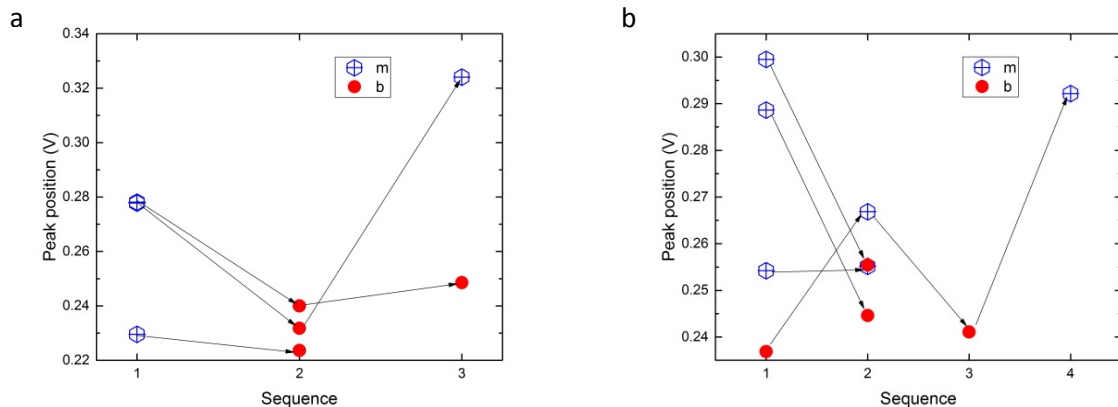


Figure A3 Positions for peak II as a function of measurement sequence at a) 50mV/s and b) 100mV/s scan speed

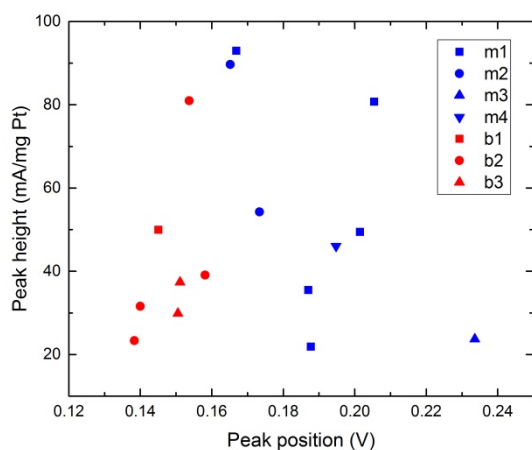


Figure A4 Peak height as a function of Peak position with legend indicating measurement sequence.

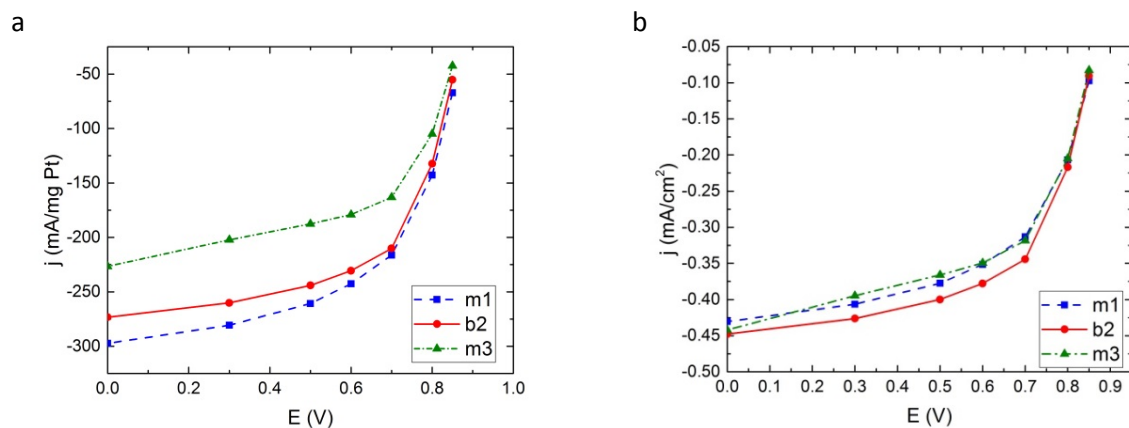
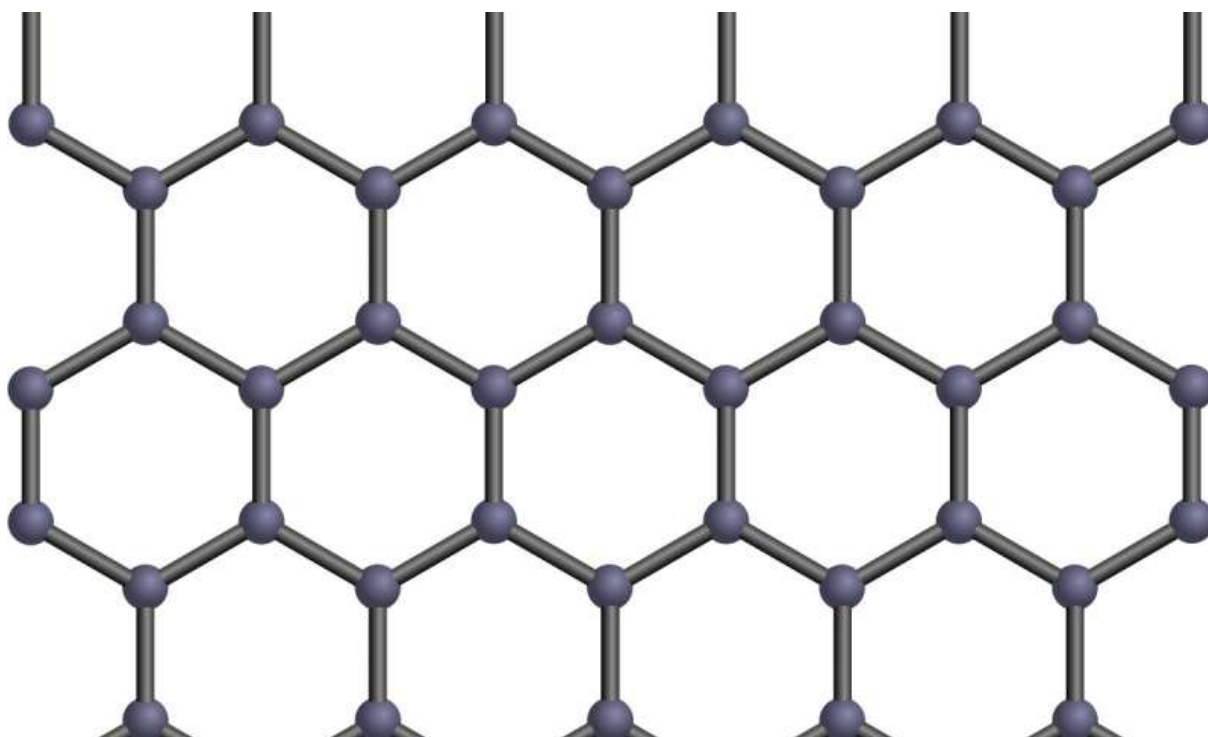


Fig A5 Hydrodynamic voltammograms for Pt@Fe illustrating the catalytic activity for oxygen reduction in the two different magnetic configurations, calculated both as a) mass activity and b) specific activity.

6 The ambiguity of the active centre in noble metal electrocatalyst alternatives



6.1 Abstract

Nitrogen-doped carbon-based materials have recently received much attention due to their activity towards the oxygen reduction reaction and the endless possibilities to tailor their electrocatalytic properties. It has been shown that by introducing nitrogen as a heteroatom into a graphitic structure, materials with electrocatalytic properties can be acquired. However, the synthesis of such materials often involves high temperature treatment that alters the original structure of the material with a rather random inclusion of nitrogen as a result. This leaves the exact nature of the active site in obscurity. The contribution of the different nitrogen configurations to the catalytic performance is widely disputed. Based on recent literature we discuss the role of nitrogen in non-noble metal oxygen reduction catalysts. Furthermore it is discussed whether transition metals play an active role in the catalysis mechanism of the nitrogen-doped graphitic materials.

6.2 Introduction

The first source of inspiration towards a non-noble metal alternative to platinum came from naturally occurring oxygen activation molecules. A structure not very different from the heme B group in blood cells, iron phtalocyanine, was studied by Yeager et al. [30] and was defined as a new type of material that exhibited activity for oxygen reduction. After Yeager's study followed a number of reports about various transition metal phtalocyanine and porphyrine like complexes. However, low electrochemical activities and issues with stability of the materials in the harsh fuel cell conditions limited the success [50]. As a strategy to improve the low stability of these, sometimes called organometallic complexes, a heat treatment step was included in the synthesis turning out not only to improve the stability but also increase the catalytic activity of the material. It was subsequently found that the starting material did not necessarily have to be of macrocyclic or even aromatic structure but required simply metal, carbon and nitrogen sources. Nevertheless, huge efforts followed exploring the influence of precursors, transition metal, ligand, synthesis routes and temperature with the goal to optimize the activity, selectivity, stability of the electrocatalytic materials [30, 45, 50, 167-171]. Moreover, recent studies have also shown that these materials exhibit activity also for Oxygen Evolution Reaction (OER) [49] and Hydrogen Evolution Reaction (HER) [165].

Following the discovery of carbon nanotubes and graphene, the area of non-noble metal ORR catalysts widened substantially. Introducing nitrogen as a heteroatom in graphitic structures turned out to make the materials catalytically active for oxygen reduction, while maintaining the superior mechanical and chemical properties of graphitic materials [172].

Since Yeager's pioneering results on phtalocyanines, numerous reports have shown that structures based on cheap and abundant materials like carbon, nitrogen and transition metals can successfully catalyse oxygen reduction and that nitrogen, regardless of the macrostructure it is a part of, plays a key role for the catalysis of non-noble metal materials [50].

The making of electrochemically active materials from simple precursors creating the active site moieties upon heat treatment represent a milestone in the research of non-noble metal catalysts and it certainly opens up an enormously wide range of possibilities. However, it is also generally agreed that the heat treatment alters the structure of the material leaving the exact nature of the active site in complete obscurity [50]. As a result, the variety of suggested active sites and mechanisms spans over nitrogen-doped graphitic materials as well as the macrocycle complexes, including or excluding a transition metal as an active part of the centre.

The question remains why there appears to be so little consensus regarding what controls the catalytic behaviour in non-noble metal catalysts? There are reasons to believe that the differences in the wide variety of catalyst materials might just be more related to the synthesis route than to the actual active site. More importantly, it follows that most likely the nitrogen modification of carbon is more important in yielding the active sites than the incorporation of metal, be it noble or non-noble.

This short review aims so summarize and discuss the latest views in the literature on the origin of catalytic activity in non-noble metal catalysts.

6.3 The role of nitrogen in doped graphitic structures

What does it take to catalyse the oxygen reduction reaction? The reaction is a multi-electron process involving a number of elementary steps and intermediates. Two main routes have been identified, although the exact mechanism is still not fully understood: the 4-electron reduction pathway from O_2 to H_2O , and the 2-electron reduction resulting in hydrogen peroxide. The oxygen reduction reaction (ORR) mechanism is most extensively studied on platinum. Norskov et al. showed through Density Functional Theory (DFT) modelling that among the pure metals, platinum seems to possess the optimal binding strength with the oxygen molecule in order to carry out the reduction reaction [26]. From the studies on platinum, the general consensus seem to be that an end-on chemisorption mode of the oxygen molecule tends to favour the $2-e^-$ reduction path to hydrogen peroxide. On the other hand, a bridge like chemisorption tends to increase the bond length in the oxygen molecule, thereby weakening the bond and hence facilitating the subsequent reduction steps following the 4-electron reduction pathway to water [52].

Analogous to the binding mechanism for platinum, a rather similar mechanism for nitrogen has been described: doping a graphitic structure with nitrogen as a heteroatom will change the chemisorption mode from an end-on configuration – as for un-doped carbon nanotubes – to a bridge like configuration steering the reaction towards the 4-electron reduction [52, 173]. Furthermore, it is claimed that doping graphitic structures with nitrogen can even enhance the conductivity in the graphitic carbon lattice [174]. N-doped carbon also shows increased oxidation resistance capability – a highly desirable property inside the harsh fuel cell conditions [175].

Wang et al [176] suggested that by introducing N into the carbon lattice the electronic density of states near the Fermi level of the doped graphitic structure would increase, hence facilitating electron transfer from the carbon electronic bands to the antibonding orbitals of O_2 . It has been proposed that nitrogen exhibits both donor properties, due to its 5 valence electrons compared to 4 for carbon, and acceptor properties, since nitrogen is more electronegative than carbon [174]. A wide spread theory is that this creates a net positive charge on the adjacent carbon atom in the graphitic structure, enabling the oxygen to chemisorb [44, 177-179]. Considering the conditions enabling a base for an active centre in the structure, two electrochemically different atoms – in this case nitrogen and carbon – are closely located to one another creating extremely high and accessible electric fields. Locally such fields approximate to 10^9 V/m, assuming 0.5 V over the distance between the atoms, about 0.15 nm, just as a rough estimate. For comparison, this is 10-100 times larger than typical dielectric strength breakdown field. High voltage insulation materials operate at electric fields ranging up to around 10^6 V/m.

A common way to produce N-doped graphitic materials such as carbon nanotubes involves thermal decomposition of nitrogen and carbon precursors over metal nanoparticles. Pyrolysis or Chemical Vapour Deposition (CVD) carried out around 700-1000 °C incorporates the nitrogen during the synthesis of the actual structure, involving few synthesis steps [173, 180]. In general, the process of doping graphitic structures with nitrogen can be seen as a competition between the formation of C-N bonds and C-C bonds where minimization of the internal energy of the structure is the driving force. This process is strongly dependent on the synthesis temperature where higher temperatures favour C-C bonding [181]. In accordance, several groups report that the total content of nitrogen decreases as the temperature is elevated [31, 182].

The activity for the oxygen reduction reaction has mostly been ascribed to three configurations of nitrogen in a sp^2 carbon lattice: the pyridinic-N, the pyrrolic-N and the graphitic-N configuration, see Fig 1.

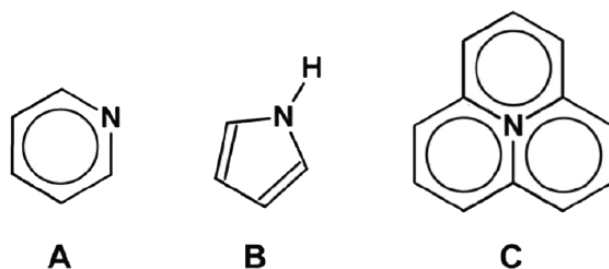


Fig 1 Pyridinic-N (A), pyrrolic-N (B) and graphitic-N (C) configuration of nitrogen in sp^2 carbon

Graphitic-N can be visualised as a nitrogen atom substituting a carbon atom in a sp^2 -carbon lattice. The three sp^2 hybridized orbitals are filled with one electron each thus creating σ bonds with neighbouring carbon atoms. Pyridinic-N is the configuration in which each N atom is bonded to two carbon atoms and donates one p-electron to the aromatic π -system. It has one lone pair of electrons in addition to the electron donated to the π bond. Pyrrolic N atoms creates together with 4 carbons a five-membered heterocyclic ring and contribute (like graphitic-N) with two p-electrons to the π -system [183, 184]. Apart from graphitic, pyrrolic and pyridinic groups researchers have identified other configurations that can exist in graphitic structures, such as amino groups [185], oxidized pyridinic groups [31, 172] and cyanide [186]. The potential contribution to electrocatalytic activity of these groups is, however, generally much less discussed.

As a result of the high temperature treatment of the catalyst materials, a controlled incorporation of nitrogen is rather difficult to achieve and the configuration of nitrogen sites hard to tailor. Therefore, several configurations of nitrogen often all appear simultaneously in the final structures [50, 180, 186, 187].

Whether only one, several or all configurations of nitrogen are able to contribute to the catalysis of oxygen reduction is widely disputed. Moreover, nitrogen configured in a pyridinic position is generally considered a preferred site for binding transition metals [31], hence, the list of possible active sites is amended with transition metal atoms coordinated to either two or four pyridinic nitrogen. Interestingly graphitic-N has been reported to be the only stable species at elevated temperatures amongst the above mentioned configurations. Kundu et al. showed that both pyridinic and pyrrolic-N tend to convert into graphitic-N at high temperatures [188].

Analogous to nitrogen the local charge shift in graphitic network can be tailored and tuned by other heteroatoms like sulphur [189-191], boron [192, 193] and phosphorus [194, 195], offering a range of electro-negativities and sizes. Whether the small difference in electronegativity between C and S is sufficient to create charge transfer large enough to enable symmetry breaking in O_2 has been questioned [25, 196].

Through significant efforts, catalysts have been produced with impressive activities, meaning comparable values to commercial Pt. However, high activity values for nitrogen-doped carbon based catalysts are often observed in alkaline conditions where small overpotentials and long-term

durability is more easily achieved [178]. Taking into account that acidic fuel cell technology is the much more wide-spread and commercially preferred option, alternatives are still few. Vertically Aligned N-doped Carbon Nanotubes (VA-NCNT) are among the more highly performing catalysts in terms of both activity and durability in PEM fuel cells [178]. Unfortunately, these materials are prepared through pyrolysis, losing out on control and tunability.

Although not the only method, XPS seems to be the most utilized technique to identify and distinguish the nitrogen sites. The nitrogen peak is deconvoluted into relative amounts of nitrogen-species present in the sample. It is however important to note that uncertainty regarding the exact amounts remains due to strong overlap of peaks in the spectra.

The electrocatalytic performance of the material can be tested using a rotating ring disk electrode (RRDE) in a 3-electrode cell, providing information about the onset potential, limiting current and selectivity [175]. Typically, the electrochemical performance is subsequently correlated with the XPS data in order to assign the different nitrogen species with possible contribution to the electrocatalytic activity.

Linfei Lai et al. fabricated two types of nitrogen-doped graphene by annealing graphene-oxide under ammonia and by annealing of a composite of N-containing polymer and reduced graphene oxide composite, where the first route resulted in mainly graphitic-N and pyridinic-N centres [184]. Annealing the composite of polyaniline and reduced graphene oxide yielded mainly pyridinic-N sites while with polypyrrole as the N-rich polymer more pyrrolic-N sites were generated. Comparing the results from rotating disk electrode setups, the graphitic-N rich material showed a higher limiting current compared to the sample rich in pyridinic or pyrrolic sites. Furthermore, a higher onset potential was achieved for the pyridinic-N rich material compared to pyrrolic-N. It was therefore concluded that graphitic-N is the most important configuration for the electrocatalytic activity while pyridinic-N can improve the onset potential. In addition, since higher total amounts of nitrogen in the structure not necessarily correlated to a higher catalytic performance this work indicates that not all configurations of nitrogen contribute to the catalytic activity and hence, must be incorporated selectively into the graphitic structure. Further aggravating the identification of the active site in N-doped graphene is the presence of metal impurities from the exfoliation process in graphene synthesis [25] or CVD of CNTs [48]. Moreover, Dommele and Wong discuss how over-inclusion of nitrogen into the graphitic carbon lattice can cause instability, structure collapse and inhibition of nanostructure formation [52, 174].

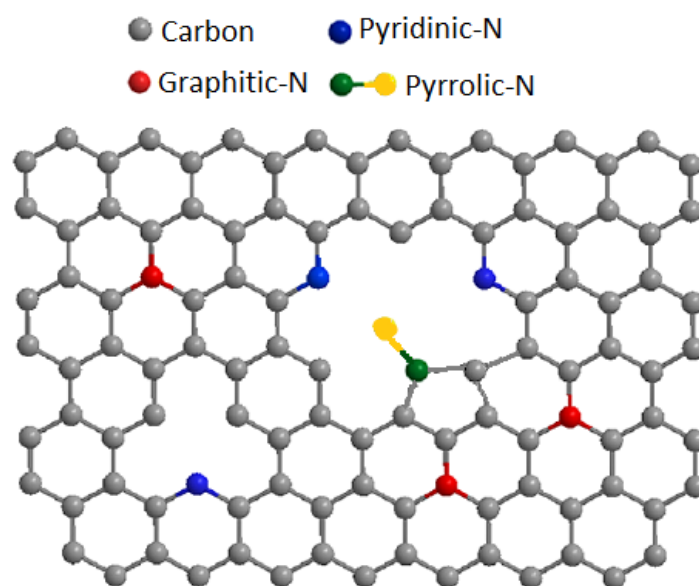


Fig 2 Nitrogen-doped sp^2 -hybridized carbon lattice

Subramanian et al investigated a nitrogen-modified carbon black-based catalyst created through synthesis of nitrogen-rich polymeric resins on oxidized carbon black [197]. The synthesis was followed by a heat treatment step creating samples fired at 400, 600, 700, 800 and 1000 °C respectively. XPS revealed the presence and proportion of pyridinic, pyrrolic and graphitic nitrogen groups in the different samples. In accordance with previous reports [186] pyridinic nitrogen groups tend to convert into graphitic nitrogen at elevated temperatures (>800 °C). The sample produced in 800 °C shows the largest fraction of pyridinic nitrogen and, as concluded from RRDE measurements of the catalytic performance, also the highest activity, indicating that pyridinic nitrogen sites are active for oxygen reduction.

In contradistinction, a material synthesized by Wong et al. showed no loss in catalytic activity when subjected to a stability test where almost all pyridinic groups were lost [198]. Moreover, other stability tests revealed that pyridinic-N is susceptible to protonation inside the acidic environment of PEMFCs, hence stop being active over time [52, 199, 200].

Parvez et al chose another interesting pathway in order to elucidate the contribution of nitrogen species to the ORR activity [31]. In their work they used cyanamide as a nitrogen source and graphene oxide as precursor to produce a carbon-nitride-graphene composite. The material was then thermally treated at 800, 900 and 1000 C in order to introduce nitrogen moieties into the graphene structure through the decomposition of the carbon nitride. The total nitrogen content in the resulting material was analysed by XPS and determined to be 12%, 5% and 4% in the samples fired at 800, 900 and 1000 °C respectively. Moreover, the pyridinic-N content seems to drop faster than graphitic-N as the temperature is increased which is consistent with the theory that pyridinic-N might convert into graphitic-N at high temperatures. Consequently the two samples fired at the higher temperatures contain a larger ratio of graphitic-N over pyridinic-N with the sample fired at 900 °C having the highest ratio. The electrochemical activity as tested with RRDE reveals that the best activity is achieved for the sample fired at 900 °C, hence the importance of the pyridinic-N to the ORR activity is ruled out here. Furthermore, it is suggested that the content of graphitic-N might be the important player in determining the catalytic performance.

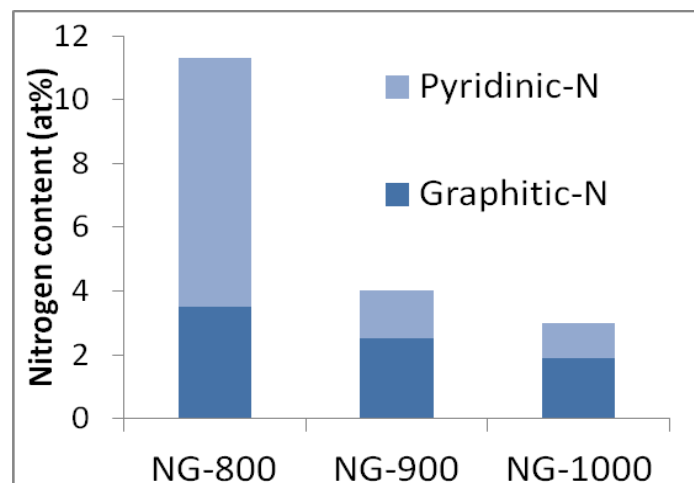


Fig 3 Amount of pyridinic- and graphitic-N in the nitrogen doped graphene samples produced by Parvez et al.

6.4 The role of transition metals in doped graphitic structures

Interestingly, the experiment of Parvez et al. was continued by introducing Fe nanoparticles into the synthesis, continued with the subsequent firing step [31]. It was argued that the Fe is being coordinated to the pyridinic-sites and that the activity can be increased until all pyridines are saturated with Fe. This point would be reached at a Fe content of 5wt% based on the reasoning that further increase of the metal content does not further increase the activity. However, after studying the results from the electrochemical evaluation of the samples, a different picture emerges. It becomes clear that introduction of 5wt% Fe nanoparticles in the synthesis results in as much improvement for the sample containing almost exclusively graphitic-N as it does for the sample with pyridinic-N as dominant species.

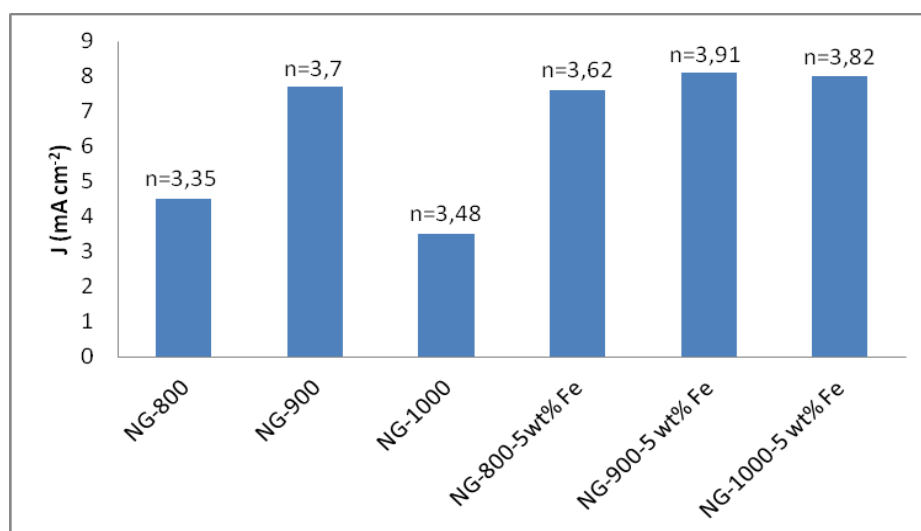


Fig 4 Results from electrochemical evaluation for samples synthesized with- and without the presence of Fe nanoparticles. “J” represents the current density and “n” the electron transfer number.

To the best of our knowledge this can only have two possible explanations. Either the pyridinic-N sites were conserved by the coordination with Fe atoms throughout the treatment of 900 – 1000 °C or the Fe particles served to help incorporating more graphitic-nitrogen into the structure, hence creating more active sites. Moreover, the very small difference in catalytic performance compared to the sample fired at 900 C with and without the presence of Fe seems to strengthen the theory of the metal playing a passive role in the catalysis.

To make sure that the remarkable performance showed by the vertically aligned nitrogen-doped carbon nanotubes made by Gong et al was not attributed to the residual metal particles remaining from the synthesis, the iron particles were removed completely by acid washing [201]. Since there was no decrease in catalytic activity it was concluded that the metal particles have no influence on the catalytic behaviour of the nanotubes.

Recently, a new branch of nitrogen-doped graphitic materials has emerged in which Metal Organic Frameworks (MOF), Covalent Organic Frameworks (COF) and biomass materials are used as precursors [14, 202-205]. Claimed advantages using such materials include intrinsic high surface area and no need for ammonia gas treatment or post doping with transition metals. What is originally a well-defined structure is typically carbonized at 700-900 °C in which process the activity increases and simultaneously the characterization becomes considerably harder. There is still little consistency in terms of what transition metal gives the best catalyst [202, 203].

Although extensive studies, dating back to Yeager's time, have shown high performing materials based on transition metals, the issue with low stability of such materials remains unsolved. Despite being coordinated to nitrogen, the transition metal can be leached out in the acidic environment of the PEM fuel cell [25, 51]. Moreover, transition metal centres run the risk of CO poisoning – an intrinsic advantage of the metal-free analogues [201]. Based on our reasoning, the metal-free oxygen reduction catalysts based on nitrogen-doping of graphitic structures have proven themselves as active ORR catalysts, making them the more stable, cheaper and more environmentally friendly alternative.

6.5 Dopant free graphitic structures

If transition metals play a limited role in the catalysis of doped graphitic materials and the main purpose of the heteroatom dopants is to create a charge shift on the adjacent carbon atom, catalytically active graphitic materials could possibly be made completely dopant free. A handful of recent studies have shown that the edges of graphitic planes as well as defect rich graphene are catalytically active [44, 48, 177]. Zhao et al were in 2016 the first ones to synthesize a metal-free defect-rich graphene with a high catalytic activity for ORR [48]. The types of defects were identified as pentagons, hexagons and octagons in the otherwise hexagonal carbon structure. Defects in pure carbon sp^2 -lattices are believed to be more stable than defects in the shape of heteroatoms – a desirable property in the harsh conditions of a PEM fuel cell. Ways to precisely and efficiently include the desirable defects and identifying which one(s) are causing the activity will remain a challenge in the coming years.

6.6 Conclusions

From our brief analysis of the literature we come to the conclusion that N-doped graphitic carbon in itself is active in the oxygen reduction reaction regardless of the activity of metal that has been incorporated. In addition, the chemical and thermal stability of the N-doped carbon is very good which can only be negatively affected by the introduction of metal, whereas nitrogen and carbon are readily available base chemicals.

Unfortunately, it is not fully clear which configuration of N contributes the most to the ORR, however, a pattern seems to emerge where graphitic nitrogen determines the limiting current density whereas the onset potential is governed by the amount of pyridinic nitrogen. Graphitic-N seems to be the only stable species at elevated temperatures. Moreover, it is not subject to protonation in fuel cell conditions.

Resolving the function of each nitrogen configuration has not been made clearer with synthesis methods involving firing of the structures, since the resulting material is left fully uncharacterized. In addition, firing processes favour C-C bonding at elevated temperatures, thus countering the objective of doping. Correlating XPS results with results from electrochemical testing does not really provide a definite answer. Although being a widely used procedure, it presents a rather indirect way of figuring out the structure of the active site, which is not an unimportant drawback since the conclusions strongly depend on the accuracy of data fitting.

Initial results from defect-rich pure carbon catalysts strengthen the idea that the key to catalytic activity in graphitic materials is *defects* rather than *dopants*. To break the oxygen bond and catalyse oxygen reduction, a conductive structure, i.e. sp^2 hybridized carbon, with local electric field variations is essential!

The synthesis of graphitic material many times involves the use of metal and it cannot be excluded that some gets trapped in the structures. Hence, a keen eye on the origin of catalytic activity of the resulting structures remains a clear issue!

Summary

The increasing energy demand of the world population in combination with tangible climate change effects stemming from rising carbon dioxide emissions is currently characterizing a large portion of the political and societal debate. Despite huge technological advancement in the field of renewable energy resulting in energy prices lower than that of fossil based energy, the rate of greenhouse gas emissions has not even levelled off but rather kept increasing. A part of the problem lies in the very nature of season and weather dependent energy conversion technologies producing electricity peaks that are hard to buffer. The solar and wind powered scenario is not yet able to completely replace the relatively demand flexible fossil fuel based power plants. The gap between energy production and energy use, in essence meaning storage and distribution of sustainable energy, constitutes one of the largest challenges of our times. Hydrogen has been proposed as a molecule with the potential of being an important energy carrier in a renewable energy based economy. In a fuel cell, hydrogen can be electrochemically oxidized to water, releasing its chemical energy without the emission of combustion by-products like carbon dioxide. Commonly platinum is used as a catalyst to speed up the anode and cathode reactions in a fuel cell. Reversibly, an electrolyser uses electricity to electrochemically split water into its constituents; hydrogen and oxygen. Ideally, hydrogen could be produced where and when the electricity is available or cheap and be stored or transported to the location where it is needed, although technical challenges as well as infrastructural hurdles are still to be solved. If electrochemical devices, such as fuel cells, are to play a major role in the future energy landscape a better understanding of catalytic processes along with cheap and scalable non-noble metal catalysts are still needed. These issues are being addressed in this thesis in the following manner;

Chapter 1 gives an introduction to energy related challenges in our society and the electrocatalytic processes that are through to play a role in the future of sustainable energy conversion and storage. The concept of hydrogen fuel cells is also reviewed in this chapter and how some of the key challenges in fuel cell technology are being investigated in this thesis.

In Chapter 2 we describe a method we developed for synthesizing monodispersed bi-metallic core-shell type nanoparticles. Such particles not only enable lower amounts of noble metals to be used in the catalyst but opens up the possibility to assess the properties of individual layers as well as to manipulate their structure. The method is based on galvanic replacement in bi-continuous micro-emulsions and offers a room-temperature and scalable route to monodisperse nanoparticles. Furthermore, the method is tuneable and we discuss for which metals it is most and least suitable.

Chapter 3 reviews the various analysis techniques that contribute to nanoparticle structural analysis. How can the structure of core-shell type nanoparticles be accurately and easily determined? This question is being answered by investigating the limits of contemporary analysis strategies as well as showing how common deviations from perfect core-shell structures can be identified. It is crucial to nanoparticle analysis that there are methods beyond visual imaging since sub-nanometre pin-holes in the shell may determine the performance and lifetime of the whole particle. A chart of pros and cons of individual analysis techniques and suggestions how they can be combined in elucidating core-shell structure, is provided in this chapter.

In Chapter 4 we relate the lattice properties of platinum with its catalytic properties, by combining crystallographic information from X-Ray Diffraction with electrochemical data acquired by Rotating Disk Electrode experiments. We also discuss the contribution of different types of strain on the crystallographic response. Results show that the activity of platinum as a shell material on non-noble metals, is influenced by both the lattice strain as well as the type of core metal. We find an exponential dependence of the activity on the strain for all three core-shell types included in the study. Finally, we decouple the changes in catalytic activity with respect to a geometrical and an energetic contribution, both being of electronic origin. Our results suggest that the catalytic performance of platinum can be both improved and worsened depending on the type of underlying lattice. The possibility of using core-shell structure to fine-tune the catalytic properties of the shell metal is encouraging since complex electrocatalytic reactions place high demands on their catalysts. Lattice modifications provide one possible route in replacing platinum as the best performing catalyst for oxygen reduction reaction with more abundant metals.

Chapter 5 deals with a largely unexplored route of manipulating electrochemical processes – magneto-electrochemistry. As long as the species involved in the reaction have unpaired spins, it is fair to assume that the presence of an external magnetic field may influence their chemical behaviour. In order to investigate the electrochemical processes taking place on platinum surfaces in fuel cell conditions when exposed to a magnetic field, a set of magnets were placed inside a modified electrode shaft close to the catalyst surface. When a magnetic field is present the peaks in the I-V curve corresponding to hydrogen adsorption and desorption are shifted relative to their positions observed in the non-magnetic setting. We propose that the changes in the electrochemical behaviour observed in this study are due to the interaction of the magnetic states of hydrogen with the catalyst. At least some states of hydrogen are magnetic – so we presume that the electrochemical processes are influenced by the magnetic states of hydrogen. Considering the catalytic activity towards oxygen the reduction reaction, no significant effect has been detected or does simply not exist.

Chapter 6 poses and aims to answer the question: What is the active centre in non-noble metal electrocatalysts? Striving to reduce the amounts of noble metals used in electrocatalysts, a myriad of catalyst materials have been developed across the scientific community, based on abundant elements like carbon, nitrogen and transition metals. Impressive catalytic activities have been recorded for such materials. Nevertheless, durability is still a serious drawback in many cases, and often the synthesis method of such materials leaves the final structure of the material in obscurity. There is still lack of consensus as to where exactly the catalysis takes place in these materials, however our small review strengthens the idea that the key to catalytic activity in graphitic materials is *defects* rather than *dopants*. To break the oxygen bond and catalyse oxygen reduction, a conductive structure, i.e. sp^2 hybridized carbon, with local electric field variations is essential!

In conclusion, this thesis modestly contributes to a field growing more important every day. Reaching the environmental targets acknowledged by every independent nation of the world is not an altruistic dream but a necessity for ensuring a safe and thriving future for all of society. Whatever pathway we decide to take in transitioning to sustainable energy it is clear that electrocatalysis will play a major role in such transition. However, there are still plenty of knowledge gaps yet to be filled, a couple of which are elucidated in this thesis. All in all, the development of non-noble metal catalysts may provide the only way forward in a future hydrogen propelled society.

Samenvatting

De toenemende vraag van de wereldbevolking naar energie in combinatie met tastbare klimaatveranderingseffecten als gevolg van de stijgende koolstofdioxide-uitstoot, kenmerkt momenteel een groot deel van het politieke en maatschappelijke debat. Ondanks de enorme technologische vooruitgang op het gebied van duurzame energie, waardoor de energieprijzen lager zijn dan die van energie op basis van fossiele brandstoffen, is de uitstoot van broeikasgassen niet gestabiliseerd, maar eerder toegenomen. Een deel van het probleem ligt in de aard van seizoen- en weersgebonden energiewinningstechnologieën waarvan de geproduceerde elektriciteitspieken moeilijk te bufferen zijn. Het scenario met zonne- en windenergie is nog niet in staat de vraag naar flexibele op fossiele brandstoffen gebaseerde energie volledig te vervangen. De kloof tussen energieproductie en energieverbruik, in essentie de opslag en distributie van duurzame energie, vormt een van de grootste uitdagingen van onze tijd. Waterstof is voorgesteld als een molecuul met het potentieel om een belangrijke energiedrager te zijn in een duurzame economie. In een brandstofcel kan waterstof elektrochemisch worden geoxideerd tot water, waardoor de chemische energie ervan vrijkomt zonder dat er verbrandingsnevenproducten zoals koolstofdioxide vrijkomen. Gewoonlijk wordt platina gebruikt als een katalysator om de anode- en kathodereacties in een brandstofcel te versnellen. Omgekeerd gebruikt een elektrolyscel elektriciteit om water elektrochemisch in zijn bestanddelen te splitsen; waterstof en zuurstof. In het ideale geval zou waterstof kunnen worden geproduceerd waar en wanneer de elektriciteit beschikbaar of goedkoop is en kan worden opgeslagen of vervoerd worden naar de locatie waar het nodig is, hoewel technische uitdagingen en infrastructurele hindernissen van waterstof nog moeten worden opgelost. Als elektrochemische apparaten, zoals brandstofcellen, een belangrijke rol moeten spelen in het toekomstige energielandschap, is een beter begrip van katalytische processen samen met goedkope en schaalbare niet-edelmetalkatalysatoren nodig. Deze kwesties worden in dit proefschrift op de volgende manier behandeld;

Hoofdstuk 1 geeft een inleiding tot energiegerelateerde uitdagingen in onze maatschappij en de elektrokatalytische processen die een rol spelen in de toekomst van conversie en opslag van duurzame energie. In dit hoofdstuk wordt ook het concept van waterstofbrandstofcellen besproken en hoe enkele van de belangrijkste uitdagingen in brandstofceltechnologie in dit proefschrift worden onderzocht.

In hoofdstuk 2 beschrijven we een methode die we hebben ontwikkeld voor het synthetiseren van monodisperse bi-metaal nanodeeltjes of basis van een core-shell configuratie. Dergelijke deeltjes maken niet alleen lagere hoeveelheden van edelmetalen die in de katalysator worden gebruikt mogelijk, maar opent ook de mogelijkheid om de eigenschappen van individuele lagen te beoordelen alsook om hun structuur te manipuleren. De methode is gebaseerd op galvanische vervanging in bi-continue micro-emulsies en biedt een kamer-temperatuur en schaalbare route naar monodisperse nanodeeltjes. Verder is de methode flexibel en bespreken we voor welke metalen deze het meest en minst geschikt is.

Hoofdstuk 3 geeft een overzicht van de verschillende analysetechnieken die elk bijdragen aan de structurele analyse van nanodeeltjes. Hoe kan de structuur van core-shell type nanodeeltjes

nauwkeurig en gemakkelijk worden vastgesteld? Deze vraag wordt beantwoord door de grenzen van hedendaagse analysestrategieën te onderzoeken en te laten zien hoe algemene afwijkingen van perfecte core-shell structuren kunnen worden geïdentificeerd. Het is van groot belang voor nanodeeltjesanalyse dat er methoden zijn die verder gaan dan visuele beeldvorming, aangezien sub-nanometer gaten in de schil de prestaties en levensduur van het hele deeltje kunnen bepalen. Een tabel van voor- en tegenargumenten van individuele analysetechnieken wordt gepresenteerd en suggesties over hoe ze kunnen worden gecombineerd in het ophelderen van de core-shell structuur worden in dit hoofdstuk gegeven.

In Hoofdstuk 4 relateren we de kristalstructuur eigenschappen van platina met zijn katalytische eigenschappen, door kristallografische informatie van röntgendiffractie te combineren met elektrochemische gegevens verkregen door Rotating Disk Electrode-experimenten. We bespreken ook de bijdrage van verschillende soorten spanning aan de kristallografische respons. Resultaten tonen aan dat de activiteit van platina als schilmateriaal op niet-edelmetalen wordt beïnvloed door zowel de roosterspanning als het type kernmetaal. We vinden een exponentiële afhankelijkheid van de activiteit voor alle drie typen nanodeeltjes die in het onderzoek zijn opgenomen. Tenslotte ontkoppelen we de veranderingen in katalytische activiteit met betrekking tot een geometrische en een energetische bijdrage, beide van elektronische oorsprong. Onze resultaten suggereren dat de katalytische prestaties van platina zowel kunnen worden verbeterd als verslechterd, afhankelijk van het type onderliggende rooster. De mogelijkheid om de kern-schilstructuur te gebruiken om de katalytische eigenschappen van het schilmetaal te verfijnen, is veelbelovend, aangezien complexe elektrokatalytische reacties hoge eisen stellen aan hun katalysatoren. Roostermodificaties verschaffen een mogelijke route bij het vervangen van platina als de best presterende katalysator voor zuurstofreductiereacties met minder schaarse elementen.

Hoofdstuk 5 gaat over een grotendeels onbekende route om elektrochemische processen te manipuleren, namelijk magneto-electrochemistry. Zolang de atomen die betrokken zijn bij de reactie ongepaarde spins hebben, is het redelijk om aan te nemen dat de aanwezigheid van een extern magnetisch veld hun chemische gedrag kan beïnvloeden. Om de elektrochemische processen te onderzoeken die plaatsvinden op platina-oppervlakken in brandstofcellen bij blootstelling aan een magnetisch veld werd een set magneten geplaatst in een gemodificeerde elektrode dichtbij het katalysatoroppervlak. Wanneer een magnetisch veld aanwezig is, worden de pieken in de I-V-curve die overeenkomt met waterstofadsorptie en -desorptie verschoven ten opzichte van hun posities die worden waargenomen in de niet-magnetische instelling. We stellen voor dat de veranderingen in het elektrochemische gedrag waargenomen in deze studie te wijten zijn aan de interactie van de magnetische toestand van waterstof met de katalysator. Sommige toestanden van waterstof zijn magnetisch - dus we nemen aan dat de elektrochemische processen worden beïnvloed door de magnetische vormen van waterstof. Er is geen significant effect van de katalytische activiteit ten opzichte van zuurstofreductiereactie, door een te klein signaal of gewoon het ontbreken van dit effect.

Hoofdstuk 6 heeft als doel de vraag te beantwoorden: wat is het actieve centrum in niet-edelmetaal elektrokatalysatoren? Met het streven om de hoeveelheden edelmetalen die worden gebruikt in elektrokatalysatoren te verminderen, zijn in de hele wetenschappelijke wereld talloze katalysatormaterialen ontwikkeld op basis van overvloedige elementen zoals koolstof, stikstof en overgangsmetalen. Indrukwekkende katalytische activiteiten zijn beschreven voor dergelijke

materialen. Toch is duurzaamheid in veel gevallen nog steeds een ernstig nadeel, en vaak laat de synthesemethode van dergelijke materialen de uiteindelijke structuur van het materiaal in het ongewisse. Er is nog steeds een gebrek aan consensus over waar precies de katalyse plaatsvindt in deze materialen, maar onze kleine recensie versterkt het idee dat de sleutel tot katalytische activiteit in grafietmaterialen eerder defecten dan doteringsmiddelen zijn. Om de zuurstofbinding te verbreken en de zuurstofreductie te katalyseren, is een geleidende structuur, d.w.z. sp²-gehybridiseerde koolstof, met lokale elektrische veldvariaties essentieel!

Concluderend draagt dit proefschrift op bescheiden wijze bij aan een steeds belangrijker wordend veld. Het bereiken van de milieudoelstellingen die door elke onafhankelijke natie van de wereld worden erkend, is geen altruïstische droom, maar een noodzaak om een veilige en bloeiende toekomst voor de hele samenleving te waarborgen. Welke weg we ook kiezen voor de overgang naar duurzame energie, het is duidelijk dat elektrokatalyse een belangrijke rol zal spelen in een dergelijke transitie. Er zijn echter nog tal van kennislacunes die nog moeten worden ingevuld, waarvan een aantal in dit proefschrift worden toegelicht. Al met al kan de ontwikkeling van niet-edelmetaalkatalysatoren de enige manier zijn om vooruit te komen in een toekomstige waterstofgedreven economie.

Bibliography

1. Rosling, H., O. Rosling, and A. Rosling Rönnlund, *Factfulness*. 2018, UK: Sceptre.
2. WorldHealthOrganization, *World health statistics 2018: monitoring health for the SDGs, sustainable development goals*. 2018: Geneva, Switzerland.
3. Harper, C., Harper, C., Snowden, M., *Environment and Society*. 2017, New York: Routledge.
4. IPCC, *Special Report: Global Warming of 1.5 C*. 2018: <https://www.ipcc.ch/reports/>.
5. UNFCCC, *The Paris Agreement*. 2015, United Nations Climate Change: <https://unfccc.int/process-and-meetings/the-paris-agreement>.
6. Burke, M., W.M. Davis, and N.S. Diffenbaugh, *Large potential reduction in economic damages under UN mitigation targets*. *Nature*, 2018. **557**(7706): p. 549-553.
7. EUROSTAT, *Share of energy from renewable sources*. 2019, European Commission: ec.europa.eu/eurostat.
8. Wagner, H.A., *Space-shuttle fuel cell*, in *Handbook of Fuel Cells*, W. Vielstich, A. Lamm, and H.A.G.a.H. Yokokawa, Editors. 2010.
9. Behling, N., M.C. Williams, and S. Managi, *Fuel cells and the hydrogen revolution: Analysis of a strategic plan in Japan*. *Economic Analysis and Policy*, 2015. **48**: p. 204-221.
10. Elmer, T., et al., *Fuel cell technology for domestic built environment applications: State-of-the-art review*. *Renewable and Sustainable Energy Reviews*, 2015. **42**: p. 913-931.
11. Verne, J., *The mysterious Island*. 1874, USA: Airmont Publishing Company.
12. Carter, D., *Fuel Cells Today: Analyst View*. 2014: fuelcellstoday.com.
13. Liu, X. and L. Dai, *Carbon-based metal-free catalysts*. *Nature Reviews Materials*, 2016. **1**(11).
14. Zhan, Y., et al., *Non Noble Metal Catalyst for Oxygen Reduction Reaction and Its Characterization by Simulated Fuel Cell Test*. *Journal of The Electrochemical Society*, 2018. **165**(15): p. J3008-J3015.
15. Kulkarni, A., et al., *Understanding Catalytic Activity Trends in the Oxygen Reduction Reaction*. *Chem Rev*, 2018. **118**(5): p. 2302-2312.
16. Suen, N.T., et al., *Electrocatalysis for the oxygen evolution reaction: recent development and future perspectives*. *Chem Soc Rev*, 2017. **46**(2): p. 337-365.
17. Murthy, A.P., J. Madhavan, and K. Murugan, *Recent advances in hydrogen evolution reaction catalysts on carbon/carbon-based supports in acid media*. *Journal of Power Sources*, 2018. **398**: p. 9-26.
18. Li, Y. and J. Lu, *Metal–Air Batteries: Will They Be the Future Electrochemical Energy Storage Device of Choice?* *ACS Energy Letters*, 2017. **2**(6): p. 1370-1377.
19. Kreuer, K.-D., *Fuel Cells*. Springer, 2013. **ISBN 978-1-4614-5784-8**.
20. Zhang, J., *PEM Fuel Cell Electrocatalysts and Catalyst Layers*. 2008, London, UK: Springer.
21. Shao, M., *Electrocatalysis in Fuel Cells - A non- and low platinum approach*. 2013, London: Springer.
22. GrandViewResearch, *Fuel Cell Market Size, Share & Trends Analysis Report By Product (PEMFC, PAFC, SOFC, MCFC), By Application (Stationary, Transportation, Portable), By Region, And Segment Forecasts, 2018 - 2025*. 2018: www.grandviewresearch.com.
23. Bai, J., et al., *Nitrogen-doped graphene as catalysts and catalyst supports for oxygen reduction in both acidic and alkaline solutions*. *International Journal of Hydrogen Energy*, 2013. **38**(3): p. 1413-1418.
24. Kleijn, S.E., et al., *Electrochemistry of nanoparticles*. *Angew Chem Int Ed Engl*, 2014. **53**(14): p. 3558-86.

25. Ambrosi, A., et al., *Graphene and its electrochemistry - an update*. Chem Soc Rev, 2016. **45**(9): p. 2458-93.
26. Norskov, J.K., et al., *Origin of the Overpotential for Oxygen Reduction at a Fuel-Cell Cathode*. J. Phys. Chem. B, 2004. **108**(46): p. 17886-17892.
27. Koper, M.T.M., *Theory of multiple proton-electron transfer reactions and its implications for electrocatalysis*. Chemical Science, 2013. **4**(7): p. 2710-2723.
28. Roduner, E., *Understanding catalysis*. Chem Soc Rev, 2014. **43**(24): p. 8226-39.
29. Koper, M.T.M., *Fuel Cell Catalysis: A surface Science Approach*, ed. A. Wieckowski. 2008, Hoboken, New Jersey, USA: Wiley.
30. Othman, R., A.L. Dicks, and Z. Zhu, *Non precious metal catalysts for the PEM fuel cell cathode*. International Journal of Hydrogen Energy, 2012. **37**(1): p. 357-372.
31. Parvez, K., et al., *Nitrogen-Doped Graphene and Its Iron-Based Composite As Efficient Electrocatalysts for Oxygen Reduction Reaction*. ACS Nano, 2012. **6**(11): p. 9541-9550.
32. James, B., *2018 Cost Projections of PEM Fuel Cell Systems for Automobiles and Medium-Duty Vehicles*, U.S.D.o. Energy, Editor. 2018, Strategic Analysis Inc: www.energy.gov.
33. Tanç, B., et al., *Overview of the next quarter century vision of hydrogen fuel cell electric vehicles*. International Journal of Hydrogen Energy, 2018.
34. Bing, Y., et al., *Nanostructured Pt-alloy electrocatalysts for PEM fuel cell oxygen reduction reaction*. Chem Soc Rev, 2010. **39**(6): p. 2184-202.
35. Johnston, R.L., *Metal Nanoparticles and Nanoalloys*. 2012. p. 1-42.
36. Peng, Z. and H. Yang, *Designer platinum nanoparticles: Control of shape, composition in alloy, nanostructure and electrocatalytic property*. Nano Today, 2009. **4**(2): p. 143-164.
37. Colón-Mercado, H.R. and B.N. Popov, *Stability of platinum based alloy cathode catalysts in PEM fuel cells*. Journal of Power Sources, 2006. **155**(2): p. 253-263.
38. Huang, Y.L., et al., *Fe@Pt core-shell nanoparticles as electrocatalyst for oxygen reduction reaction in acidic media*. Ionics, 2018. **24**(1): p. 229-236.
39. Cai, Y. and R.R. Adzic, *Platinum Monolayer Electrocatalysts for the Oxygen Reduction Reaction: Improvements Induced by Surface and Subsurface Modifications of Cores*. Advances in Physical Chemistry, 2011. **2011**: p. 1-16.
40. Adzic, R.R., et al., *Platinum Monolayer Fuel Cell Electrocatalysts*. Topics in Catalysis, 2007. **46**(3-4): p. 249-262.
41. Stephens, I.E.L., et al., *Understanding the electrocatalysis of oxygen reduction on platinum and its alloys*. Energy & Environmental Science, 2012. **5**(5): p. 6744.
42. Gao, L., et al., *The effect of external magnetic fields on the catalytic activity of Pd nanoparticles in Suzuki cross-coupling reactions*. Nanoscale, 2016. **8**(15): p. 8355-8362.
43. Torun, E., et al., *Role of Magnetism in Catalysis: RuO₂(110) Surface*. The Journal of Physical Chemistry C, 2013. **117**(12): p. 6353-6357.
44. Zhou, N., et al., *Probing Active Sites on Metal-Free, Nitrogen-Doped Carbons for Oxygen Electroreduction: A Review*. Catalysts, 2018. **8**(11): p. 509.
45. Bezerra, C.W.B., et al., *A review of heat-treatment effects on activity and stability of PEM fuel cell catalysts for oxygen reduction reaction*. Journal of Power Sources, 2007. **173**(2): p. 891-908.
46. Geng, D., et al., *Non-noble metal oxygen reduction electrocatalysts based on carbon nanotubes with controlled nitrogen contents*. Journal of Power Sources, 2011. **196**(4): p. 1795-1801.
47. Li, H., et al., *Nitrogen-doped carbon nanotubes with high activity for oxygen reduction in alkaline media*. International Journal of Hydrogen Energy, 2011. **36**(3): p. 2258-2265.
48. Zhao, X., et al., *Defect-driven oxygen reduction reaction (ORR) of carbon without any element doping*. Inorganic Chemistry Frontiers, 2016. **3**(3): p. 417-421.
49. Zhao, Y., et al., *Nitrogen-doped carbon nanomaterials as non-metal electrocatalysts for water oxidation*. Nat Commun, 2013. **4**: p. 2390.

50. Chen, Z., et al., *A review on non-precious metal electrocatalysts for PEM fuel cells*. Energy & Environmental Science, 2011. **4**(9): p. 3167.
51. Baker, R., D.P. Wilkinson, and J. Zhang, *Electrocatalytic activity and stability of substituted iron phthalocyanines towards oxygen reduction evaluated at different temperatures*. Electrochimica Acta, 2008. **53**(23): p. 6906-6919.
52. Wong, W.Y., et al., *Recent progress in nitrogen-doped carbon and its composites as electrocatalysts for fuel cell applications*. International Journal of Hydrogen Energy, 2013.
53. Norskov, J.K., et al., *Origin of the overpotential for oxygen reduction at a fuel-cell cathode*. Journal of Physical Chemistry B, 2004. **108**(46): p. 17886-17892.
54. Duan, S. and R. Wang, *Bimetallic nanostructures with magnetic and noble metals and their physicochemical applications*. Materials International, 2013. **23**(2): p. 113-126.
55. Kowlgi, K., *Nano Lego - From Self-Assembly to Functional Devices*. PhD Thesis, Technical University of Delft, 2012.
56. Cui, C., et al., *Compositional segregation in shaped Pt alloy nanoparticles and their structural behaviour during electrocatalysis*. Nat Mater, 2013. **12**(8): p. 765-71.
57. Wei, Z.D., et al., *Electrochemically synthesized Cu/Pt core-shell catalysts on a porous carbon electrode for polymer electrolyte membrane fuel cells*. Journal of Power Sources, 2008. **180**(1): p. 84-91.
58. Negro, E., R. Latsuzbaia, and G.J. Koper, *Bicontinuous Microemulsions for High Yield Wet Synthesis of Ultrafine Platinum Nanoparticles: Effect of Precursors and Kinetics*. Langmuir, 2014. **30**(28): p. 8300-7.
59. Sarkar, A. and A. Manthiram, *Synthesis of Pt@Cu Core-Shell Nanoparticles by Galvanic Displacement of Cu by Pt⁴⁺ Ions and Their Application as Electrocatalysts for Oxygen Reduction Reaction in Fuel Cells*. Journal of Physical Chemistry C, 2010. **114**(10): p. 4725-4732.
60. Geboes, B., et al., *Surface and Electrochemical Characterisation of a Pt-Cu/C Nano-structured Electrocatalyst, Prepared by Galvanic Displacement*. Applied Catalysis B: Environmental, 2013.
61. Koper, R.L.E.N.G., *Synthesis, Stabilization and Activation of Pt Nanoparticles for PEMFC Applications*. Fuel Cells, 2015. **4**.
62. Kowlgi, K., et al., *Uniform metal nanoparticles produced at high yield in dense microemulsions*. J Colloid Interface Sci, 2012. **372**(1): p. 16-23.
63. Garsany, Y., et al., *Analytical Procedure for Accurate Comparison of Rotating Disk Electrode Results for the Oxygen Reduction Activity of Pt/C*. Journal of the Electrochemical Society, 2014. **161**(5): p. F628-F640.
64. Kolhatkar, A.G., et al., *Tuning the magnetic properties of nanoparticles*. Int J Mol Sci, 2013. **14**(8): p. 15977-6009.
65. Kowlgi, K., et al., *Anomalous magnetism in noble metal (nano)particles*. Colloids and Surfaces A: Physicochemical and Engineering Aspects, 2012. **413**: p. 248-251.
66. N. Aguiló-Aguayo, M.J.I.-I., J. García-Céspedes, E. Bertran, *Morphological and Magnetic Properties of Superparamagnetic Carbon-Coated Fe Nanoparticles Produced by Arc Discharge*. Journal of Nanoscience and Nanotechnology, 2009. **9**: p. 1-4.
67. Vollath, D., *Nanomaterials: An Introduction to Synthesis, Properties, and Applications*. 2009: Wiley.
68. Lado-Tourin, L.M.L.-M.I., *Reduction and Stabilization of Silver Nanoparticles in Ethanol by Nonionic Surfactants*. Langmuir, 1996. **12**: p. 3585-3589.
69. Harada, M., et al., *Characterization of water/AOT/benzene microemulsions during photoreduction to produce silver particles*. J Colloid Interface Sci, 2010. **343**(2): p. 423-32.
70. Lee, M.H., et al., *Preparation of silver nanoparticles in hexagonal phase formed by nonionic Triton X-100 surfactant*. Colloids and Surfaces a-Physicochemical and Engineering Aspects, 2002. **210**(1): p. 49-60.

71. Andersson, M., J.S. Pedersen, and A.E.C. Palmqvist, *Silver nanoparticle formation in microemulsions acting both as template and reducing agent*. *Langmuir*, 2005. **21**(24): p. 11387-11396.
72. Newton, J.E., et al., *Nanoparticle catalysts for proton exchange membrane fuel cells: can surfactant effects be beneficial for electrocatalysis?* *Phys Chem Chem Phys*, 2014. **16**(23): p. 11435-46.
73. Crespo, P., et al., *Permanent Magnetism, Magnetic Anisotropy, and Hysteresis of Thiol-Capped Gold Nanoparticles*. *Physical Review Letters*, 2004. **93**(8).
74. Vesperinas, A., et al., *Light-induced flocculation of gold nanoparticles*. *Chem Commun (Camb)*, 2007(38): p. 3912-4.
75. Eastoe, J., *Photo-destructible Surfactants in Microemulsions*. 2006. **133**: p. 106-110.
76. J. Prabhuram, et al., *Synthesis and Characterization of Surfactant-Stabilized Pt/C Nanocatalysts for Fuel Cell Applications*. *J. Phys. Chem. B*, 2003(107): p. 11057-11064.
77. Papaderakis, A., et al., *Electrocatalysts Prepared by Galvanic Replacement*. *Catalysts*, 2017. **7**(12): p. 80.
78. Kettner, M., W.B. Schneider, and A.A. Auer, *Computational Study of Pt/Co Core-Shell Nanoparticles: Segregation, Adsorbates and Catalyst Activity*. *The Journal of Physical Chemistry C*, 2012. **116**(29): p. 15432-15438.
79. Lee, J.P., et al., *Well-organized raspberry-like Ag@Cu bimetal nanoparticles for highly reliable and reproducible surface-enhanced Raman scattering*. *Nanoscale*, 2013. **5**(23): p. 11620-11624.
80. F. Maillard, S.P., E.R. Savinova, *Size effects in electrocatalysis of fuel cell reactions on supported metal nanoparticles*, in: *M. Koper, Fuel Cell Catalysis*. 2009, New York, USA: John Wiley & Sons.
81. Hosokawa, M., *Nanoparticle technology handbook*. 2007, Amsterdam, The Netherlands: Elsevier.
82. Eftekhari, A., *Nanostructured materials in electrochemistry*. Vol. 1. Weinheim, Germany: Wiley. 489.
83. Barcari, G., *Metal Nanoparticles and Nanoalloys*, ed. J. Wilcoxon and R.L. Johnston. Vol. 3. 2012: Elsevier. 213-247.
84. Kitchin, J., et al., *Role of Strain and Ligand Effects in the Modification of the Electronic and Chemical Properties of Bimetallic Surfaces*. *Physical Review Letters*, 2004. **93**(15).
85. Oezaslan, M., F. Hasché, and P. Strasser, *Pt-Based Core-Shell Catalyst Architectures for Oxygen Fuel Cell Electrodes*. *The Journal of Physical Chemistry Letters*, 2013. **4**(19): p. 3273-3291.
86. Roller, J., et al., *Flame-Based Synthesis of Core-Shell Structures Using Pd-Ru and Pd Cores*. *Electrochimica Acta*, 2014. **138**: p. 341-352.
87. Hammer, B.M., Y.; Norskov, J. K. , *CO Chemisorption at Metal Surfaces and Overlayers*. *Phys Rev Lett*, 1996. **76**(12).
88. Holmblad, P.M.L., J. H.; Chorkendorff, I.; Nielsen, L. P.;, F.S. Besenbacher, I.; Laegsgaard, E.; Kratzer, P.;, and B.N. Hammer, J. K. , *Designing surface alloys with specific active sites*. *Catalysis Letters*, 1996. **40**: p. 131-135.
89. Teng, X. and H. Yang, *Synthesis of magnetic nanocomposites and alloys from platinum-iron oxide core-shell nanoparticles*. *Nanotechnology*, 2005. **16**(7): p. S554-61.
90. Yu, Y.-T. and P. Dutta, *Synthesis of Au/SnO₂ core-shell structure nanoparticles by a microwave-assisted method and their optical properties*. *Journal of Solid State Chemistry*, 2011. **184**(2): p. 312-316.
91. Liu, Y.-T., et al., *Electrochemical activity and stability of core-shell Fe₂O₃/Pt nanoparticles for methanol oxidation*. *Journal of Power Sources*, 2013. **243**: p. 622-629.
92. Xia, L., et al., *A one-step facile synthesis of Ag-Ni core-shell nanoparticles in water-in-oil microemulsions*. *Colloids and Surfaces A: Physicochemical and Engineering Aspects*, 2010. **367**(1-3): p. 96-101.

93. Balerna, A., et al., *EXAFS and XANES structural characterization of bimetallic AuPd vapor derived catalysts*. Journal of Physics: Conference Series, 2013. **430**.
94. Wang, C., et al., *Monodisperse Pt(3)Co nanoparticles as electrocatalyst: the effects of particle size and pretreatment on electrocatalytic reduction of oxygen*. Phys Chem Chem Phys, 2010. **12**(26): p. 6933-9.
95. Zhang, J., et al., *Platinum monolayer on nonnoble metal-noble metal core-shell nanoparticle electrocatalysts for O₂ reduction*. J Phys Chem B, 2005. **109**(48): p. 22701-4.
96. Mayrhofer, K.J., et al., *Adsorbate-induced surface segregation for core-shell nanocatalysts*. Angew Chem Int Ed Engl, 2009. **48**(19): p. 3529-31.
97. Zhang, Y., et al., *Hollow core supported Pt monolayer catalysts for oxygen reduction*. Catalysis Today, 2013. **202**: p. 50-54.
98. Pigozzi, G., et al., *Effects of size reduction on the structure and magnetic properties of core-shell Ni₃Si/silica nanoparticles prepared by electrochemical synthesis*. Journal of Alloys and Compounds, 2014. **584**: p. 119-127.
99. Yang, Y., et al., *Preparation of Au-Ag, Ag-Au core-shell bimetallic nanoparticles for surface-enhanced Raman scattering*. Scripta Materialia, 2008. **58**(10): p. 862-865.
100. Steinbrück, A., et al., *Preparation and Optical Characterization of Core-Shell Bimetal Nanoparticles*. Plasmonics, 2006. **1**(1): p. 79-85.
101. Kumar, S. and S. Zou, *Electrooxidation of Carbon Monoxide and Methanol on Platinum-Overlayer-Coated Gold Nanoparticles: Effects of Film Thickness*. Langmuir, 2007(23): p. 7365-7371.
102. Kuttiyiel, K.A., et al., *Pt monolayer on Au-stabilized PdNi core-shell nanoparticles for oxygen reduction reaction*. Electrochimica Acta, 2013. **110**: p. 267-272.
103. Najjar, R., *Microemulsions - An Introduction to Properties and Applications*. 1st edition ed. 2012, Rijeka, Croatia: InTech Publisher.
104. Sieben, J.M., et al., *Synthesis and characterization of Cu core Pt-Ru shell nanoparticles for the electro-oxidation of alcohols*. International Journal of Hydrogen Energy, 2014. **39**(16): p. 8667-8674.
105. Tsai, C.W., et al., *Magnetically recyclable Fe@Co core-shell catalysts for dehydrogenation of sodium borohydride in fuel cells*. International Journal of Hydrogen Energy, 2012. **37**(4): p. 3338-3343.
106. Wojtyasiak, S., et al., *Synthesis of core-shell silver-platinum nanoparticles, improving shell integrity*. Colloids and Surfaces A: Physicochemical and Engineering Aspects, 2014. **441**: p. 178-183.
107. Chen, D., et al., *Nanometre Ni and core/shell Ni/Au nanoparticles with controllable dimensions synthesized in reverse microemulsion*. Journal of Alloys and Compounds, 2009. **475**(1-2): p. 494-500.
108. Tojo, C., M.d. Dios, and F. Barroso, *Surfactant Effects on Microemulsion-Based Nanoparticle Synthesis*. Materials, 2010. **4**(1): p. 55-72.
109. Li, C. and Y. Yamauchi, *Facile solution synthesis of Ag@Pt core-shell nanoparticles with dendritic Pt shells*. Phys Chem Chem Phys, 2013. **15**(10): p. 3490-6.
110. Merzlikin, S., *Depth Profiling by X-ray Photoelectron Spectroscopy*, in *Fakultät für Chemie*. 2007, Ruhr-Universität Bochum.
111. Goldstein, J., *Scanning Electron Microscopy and X-ray Microanalysis*. 3 ed. 2003, New York, USA: Springer.
112. Crewe, A.V., *The use of backscattered electrons for imaging purposes in a scanning electron microscope*. Ultramicroscopy, 1976. **1**: p. 231-238.
113. Carter, H.W., *Backscattered Electron Imaging: Theory and Applications*. Micron, 1980. **11**: p. 259-260.
114. Lukasczyk, T., *Generation of pure iron nanostructures via electron-beam induced deposition in UHV*, in *Der Naturwissenschaftlichen Fakultät*. Friedrich-Alexander-Universität Erlangen-Nürnberg.

115. Vogt, T., W. Dahmen, and P. Binev, *Modeling Nanoscale Imaging in Electron Microscopy*. Nanostructure Science and Technology. 2012, New York, USA: Springer.
116. Liu, J., et al., *High-Resolution Auger-Electron Spectroscopy and Microscopy of a Supported Metal Catalyst*. Surface Science, 1992. **262**(3): p. L111-L117.
117. Egerton, R.F., *Electron Energy-Loss Spectroscopy in the Electron Microscope*. 3 ed. 2011, New York, USA: Springer.
118. Mendis, B.G. and A.J. Craven, *Characterising the surface and interior chemistry of core-shell nanoparticles using scanning transmission electron microscopy*. Ultramicroscopy, 2011. **111**(3): p. 212-26.
119. Zhou, W. and Z.L. Wang, *Scanning Microscopy for Nanotechnology*. 2007, New York, USA: Springer.
120. Li, Z., *Scanning Transmission Electron Microscopy Studies of Mono- and Bimetallic Nanoclusters*. 2012. **3**: p. 213-247.
121. Cullity, B.D., *Elements of X-Ray Diffraction*. 3 ed. 1956, Massachusetts: Addison-Wesley Publishing Company Inc.
122. Tanuma, S., C.J. Powell, and D.R. Penn, *Calculations of electron inelastic mean free paths. IX. Data for 41 elemental solids over the 50 eV to 30 keV range*. Surface and Interface Analysis, 2011. **43**(3): p. 689-713.
123. Tilinin, I.S., *Qualitative Surface Analysis by Auger and X-Ray Photoelectron Spectroscopy*. Progress in Surface Science, 1996. **52**.
124. Hergert, W. and T. Wriedt, *The Mie Theory*. Vol. 169. 2012, Heidelberg, Germany: Springer.
125. Creighton, J.A. and D.G. Eadon, *Ultraviolet Visible Absorption-Spectra of the Colloidal Metallic Elements*. Journal of the Chemical Society-Faraday Transactions, 1991. **87**(24): p. 3881-3891.
126. Cookson, N.J., *Preparation and characterisation of bimetallic core-shell particles*, in *School of Chemistry*. 2009, University of Birmingham.
127. Eccles, J.W.L., et al., *UV-Vis plasmon studies of metal nanoparticles*. Electron Microscopy and Analysis Group Conference 2009 (Emag 2009), 2010. **241**.
128. Pletcher, D.G., R., *Instrumental Methods in Electrochemistry*. 2001, Cambridge, UK: Horwood Publishing.
129. Vogt, T., W. Dahmen, and P. Binev, *The Application of Scanning Transmission Electron Microscopy (STEM) to the Study of Nanoscale Systems* 2012.
130. Camardese, J., et al., *Determination of Shell Thickness of Spherical Core-Shell Ni_xMn_{1-x}(OH)₂ Particles via Absorption Calculations of X-Ray Diffraction Patterns*. Journal of the Electrochemical Society, 2014. **161**(5): p. A814-A820.
131. Zolotoyabko, E., *Basic Concepts of X-Ray Diffraction*. 2014, Weinheim, Germany: Wiley.
132. Merzlikin, S.V., et al., *Resolving the depth coordinate in photoelectron spectroscopy – Comparison of excitation energy variation vs. angular-resolved XPS for the analysis of a self-assembled monolayer model system*. Surface Science, 2008. **602**(3): p. 755-767.
133. Silva, D.O., et al., *Straightforward synthesis of bimetallic Co/Pt nanoparticles in ionic liquid: atomic rearrangement driven by reduction-sulfidation processes and Fischer-Tropsch catalysis*. Nanoscale, 2014. **6**(15): p. 9085-92.
134. Kendrick, I. and E.S. Smotkin, *Infrared and X-ray Absorption Spectroscopy of Operating Fuel Cells*. Physical Chemistry Chemical Physics.
135. Russell, A.E. and A. Rose, *X-ray absorption spectroscopy of low temperature fuel cell catalysts*. Chem Rev, 2004. **104**(10): p. 4613-35.
136. Zhufang Liu, Z., et al., *PtMo Alloy and MoOx@Pt Core-Shell Nanoparticles as Highly CO-Tolerant Electrocatalysts*. J. Am. Chem. Soc., 2009. **131**.
137. Selim Alayoglu, P.Z., Bryan Eichhorn, Adele Qi Wang, Anatoly I. Frenkel, Peter Chupas, *Structural and Architectural Evaluation of Bimetallic Nanoparticles: A Case Study of PtRu Core-Shell and Alloy Nanoparticles*. ACS Nano, 2009. **3**.
138. Ochal, P., et al., *CO stripping as an electrochemical tool for characterization of Ru@Pt core-shell catalysts*. Journal of Electroanalytical Chemistry, 2011. **655**(2): p. 140-146.

139. Henglein, A., *Preparation and Optical Absorption Spectra of AuCorePtShell and PtCoreAuShell Colloidal Nanoparticles in Aqueous Solution*. *J Phys Chem B*, 2000(104): p. 2201-2203.
140. Rao, A., et al., *Characterization of nanoparticles using Atomic Force Microscopy*. *Journal of Physics: Conference Series*, 2007. **61**: p. 971-976.
141. Shard, A.G., *A Straightforward Method For Interpreting XPS Data From Core–Shell Nanoparticles*. *The Journal of Physical Chemistry C*, 2012. **116**(31): p. 16806-16813.
142. Lim, J., et al., *Characterization of magnetic nanoparticle by dynamic light scattering*. *Nanoscale Res Lett*, 2013. **8**(1): p. 381.
143. Pecora, R., *Dynamic light scattering*. 1985, New York, United States: Plenum Press.
144. Norskov, B.H.J.K., *Theoretical Surface Science and Catalysis—Calculations and Concepts*. *Advances in Catalysis*, 2000. **45**: p. 71-129.
145. Santos, E., P. Quaino, and W. Schmickler, *On the electrocatalysis of nanostructures: Monolayers of a foreign atom (Pd) on different substrates M(111)*. *Electrochimica Acta*, 2010. **55**(14): p. 4346-4352.
146. Bindu, P. and S. Thomas, *Estimation of lattice strain in ZnO nanoparticles: X-ray peak profile analysis*. *Journal of Theoretical and Applied Physics*, 2014. **8**(4): p. 123-134.
147. T. Biegler, D.A.J.R., R. Woods, *Limiting Oxygen Coverage on Platinized Platinum; Relevance to Determination of Real Platinum Area By Hydrogen Adsorption*. *Journal of Electroanalytical Chemistry*, 1971. **29**(2).
148. Trasatti, P., *Real Surface Area Measurements in Electrochemistry*. *Pure & Appl. Chem.*, 1991. **63**(5): p. 711-734.
149. Temmel, S.E., et al., *Investigating the Role of Strain toward the Oxygen Reduction Activity on Model Thin Film Pt Catalysts*. *ACS Catalysis*, 2016. **6**(11): p. 7566-7576.
150. Popescu, R., et al., *Structure of hollow spheres analyzed by X-ray diffraction, transmission electron microscopy, and dynamic light scattering*. *Journal of Nanoparticle Research*, 2013. **15**(6).
151. Koper, G.J.M., *An introduction to Interfacial Engineering*. 2009, Delft, The Netherlands: VSSD.
152. H. Ibach, H.L., *Solid-State Physics: An Introduction to Principles of Materials Science*. 2003, Berlin Heidelberg: Springer-Verlag 501.
153. Zhao, Y. and J. Zhang, *Microstrain and grain-size analysis from diffraction peak width and graphical derivation of high-pressure thermomechanics*. *Journal of Applied Crystallography*, 2008. **41**(6): p. 1095-1108.
154. Westsson, E. and G. Koper, *How to Determine the Core-Shell Nature in Bimetallic Catalyst Particles?* *Catalysts*, 2014. **4**(4): p. 375-396.
155. Pintu Saji, A.K.G., Mohsin A. Bhat, Pravin P. Ingole, *Probing the Crystal Structure, Composition-Dependent Absolute Energy Levels, and Electrocatalytic Properties of Silver Indium Sulfide Nanostructures*. *ChemPhysChem*, 2016. **17**: p. 1195–1203.
156. Steiner and Ulrich, *Magnetic Field Effects in Chemical Kinetics and Related Phenomena*. *Chem. Rev.*, 1989. **89**: p. 51-147.
157. Turro, N.J. and B. Kraeutler, *Magnetic field and magnetic isotope effects in organic photochemical reactions. A novel probe of reaction mechanisms and a method for enrichment of magnetic isotopes*. *Accounts of Chemical Research*, 1980. **13**(10): p. 369-377.
158. Okazaki, M. and T. Shiga, *Product Yield of Magnetic-Field-Dependent Photochemical-Reaction Modulated by Electron-Spin-Resonance*. *Nature*, 1986. **323**(6085): p. 240-243.
159. Shovkovy, I.A., *Magnetic Catalysis: A Review*, in *Strongly Interacting Matter in Magnetic Fields*. 2013, Springer, Berlin, Heidelberg.
160. Periasamy, N. and H. Lindschitz, *Cage Escape and Spin Rephasing of Triplet Ion-Radical Pairs: Temperature-Viscosity and Magnetic Field Effects in Photoreduction of Fluorenone by DABCO*. *Chemical Physics Letters*, 1979. **64**(2).
161. Dunwoody, D.C., et al., *Magnet Incorporated Carbon Electrodes: Methods for Construction and Demonstration of Increased Electrochemical Flux*. *Electroanalysis*, 2005. **17**(15): p. 1487-1494.

162. Melander, M., K. Laasonen, and H. Jónsson, *Effect of Magnetic States on the Reactivity of an FCC(111) Iron Surface*. The Journal of Physical Chemistry C, 2014. **118**(29): p. 15863-15873.
163. Łukaszewski, M., M. Soszko, and A. Czerwiński, *Electrochemical Methods of Real Surface Area Determination of Noble Metal Electrodes – an Overview*. International Journal of Electrochemical Science, 2016. **11**: p. 4442-4469.
164. Oudenhuijzen, M.K., J.H. Bitter, and D.C. Koningsberger, *The Nature of the Pt-H Bonding for Strongly and Weakly Bonded Hydrogen on Platinum A XAFS spectroscopy study of the Pt-H antibonding state shaperesonance and Pt-H EXAFS*. J. Phys. Chem. B, 2001. **105**: p. 4616-4622.
165. Zheng, Y., et al., *Toward design of synergistically active carbon-based catalysts for electrocatalytic hydrogen evolution*. ACS Nano, 2014. **8**(5): p. 5290-6.
166. Diaz-Morales, O., et al., *Hydrogen adsorption on nano-structured platinum electrodes*. Faraday Discuss, 2018. **210**(0): p. 301-315.
167. Bezerra, C.W.B., et al., *A review of Fe–N/C and Co–N/C catalysts for the oxygen reduction reaction*. Electrochimica Acta, 2008. **53**(15): p. 4937-4951.
168. Deng, X., X. Wang, and Z.-F. Ma, *Influence of preparation process on non-noble metal-based composite electrocatalysts for oxygen reduction reaction*. Journal of Power Sources, 2008. **183**(2): p. 604-608.
169. Karim, N.A. and S.K. Kamarudin, *An overview on non-platinum cathode catalysts for direct methanol fuel cell*. Applied Energy, 2013. **103**: p. 212-220.
170. Kobayashi, M., et al., *Indirect contribution of transition metal towards oxygen reduction reaction activity in iron phthalocyanine-based carbon catalysts for polymer electrolyte fuel cells*. Electrochimica Acta, 2012. **74**: p. 254-259.
171. Zhu, H., S.J. Paddison, and T.A. Zawodzinski, Jr., *The effects of the ligand, central metal, and solvent on the O₂ binding of non-precious metal catalyst model systems: an ab initio study*. Electrochimica Acta, 2012.
172. Chen, Z., D. Higgins, and Z. Chen, *Nitrogen doped carbon nanotubes and their impact on the oxygen reduction reaction in fuel cells*. Carbon, 2010. **48**(11): p. 3057-3065.
173. Chen, Z., D. Higgins, and Z. Chen, *Electrocatalytic activity of nitrogen doped carbon nanotubes with different morphologies for oxygen reduction reaction*. Electrochimica Acta, 2010. **55**(16): p. 4799-4804.
174. Dommele, S.V., *Nitrogen Doped Carbon Nanotubes: synthesis, characterization and catalysis*. 2008, Universiteit Utrecht.
175. Zhang, J., *PEM Fuel Cell Catalysts and Catalysts Layers*. ISBN 978-1-84800-935-6, 2008.
176. Wang, P., et al., *Origin of the catalytic activity of graphite nitride for the electrochemical reduction of oxygen: geometric factors vs. electronic factors*. Phys Chem Chem Phys, 2009. **11**(15): p. 2730-40.
177. Tao, L., et al., *Bridging the Surface Charge and Catalytic Activity of a Defective Carbon Electrocatalyst*. Angew Chem Int Ed Engl, 2019. **58**(4): p. 1019-1024.
178. Shui, J., et al., *N-doped carbon nanomaterials are durable catalysts for oxygen reduction reaction in acidic fuel cells*. Sci Adv, 2015. **1**(1): p. e1400129.
179. Bhatt, M.D., G. Lee, and J.S. Lee, *Density Functional Theory (DFT) Calculations for Oxygen Reduction Reaction Mechanisms on Metal-, Nitrogen- co-doped Graphene (M-N₂-G (M = Ti, Cu, Mo, Nb and Ru)) Electrocatalysts*. Electrochimica Acta, 2017. **228**: p. 619-627.
180. Podyacheva, O.Y., et al., *Nitrogen doped carbon nanotubes and nanofibers: Composition, structure, electrical conductivity and capacity properties*. Carbon, 2017. **122**: p. 475-483.
181. Xue, Y., et al., *Low temperature growth of highly nitrogen-doped single crystal graphene arrays by chemical vapor deposition*. J Am Chem Soc, 2012. **134**(27): p. 11060-3.
182. Zhao, Y., K. Watanabe, and K. Hashimoto, *Self-supporting oxygen reduction electrocatalysts made from a nitrogen-rich network polymer*. J Am Chem Soc, 2012. **134**(48): p. 19528-31.
183. Chung, H.T., et al., *Cyanamide-derived non-precious metal catalyst for oxygen reduction*. Electrochemistry Communications, 2010. **12**(12): p. 1792-1795.

184. Lai, L., et al., *Exploration of the active center structure of nitrogen-doped graphene-based catalysts for oxygen reduction reaction*. Energy & Environmental Science, 2012. **5**(7): p. 7936.
185. Zhang, C., et al., *Synthesis of amino-functionalized graphene as metal-free catalyst and exploration of the roles of various nitrogen states in oxygen reduction reaction*. Nano Energy, 2013. **2**(1): p. 88-97.
186. Kumar, A., A. Ganguly, and P. Papakonstantinou, *Thermal stability study of nitrogen functionalities in a graphene network*. J Phys Condens Matter, 2012. **24**(23): p. 235503.
187. Zherebtsov, D.A., et al., *Anomalous resistivity of heavily nitrogen doped graphitic carbon*. Diamond and Related Materials, 2018. **83**: p. 75-79.
188. Kundu, S., *Electrocatalytic Activity and Stability of Nitrogen-Containing Carbon Nanotubes in the Oxygen Reduction Reaction*. J. Phys. Chem. C, 2009. **113**: p. 14302-14310.
189. Zhang, L., et al., *Catalytic Mechanisms of Sulfur-Doped Graphene as Efficient Oxygen Reduction Reaction Catalysts for Fuel Cells*. The Journal of Physical Chemistry C, 2014. **118**(7): p. 3545-3553.
190. Lu, Z.S., et al., *Sulfur doped graphene as a promising metal-free electrocatalyst for oxygen reduction reaction: a DFT-D study*. Rsc Advances, 2017. **7**(33): p. 20398-20405.
191. Hoque, M.A., et al., *Optimization of sulfur-doped graphene as an emerging platinum nanowires support for oxygen reduction reaction*. Nano Energy, 2016. **19**: p. 27-38.
192. Agnoli, S. and M. Favaro, *Doping graphene with boron: a review of synthesis methods, physicochemical characterization, and emerging applications*. Journal of Materials Chemistry A, 2016. **4**(14): p. 5002-5025.
193. Zheng, Y., et al., *Two-step boron and nitrogen doping in graphene for enhanced synergistic catalysis*. Angew Chem Int Ed Engl, 2013. **52**(11): p. 3110-6.
194. Li, R., et al., *Phosphorus-doped graphene nanosheets as efficient metal-free oxygen reduction electrocatalysts*. Rsc Advances, 2013. **3**(25): p. 9978-9984.
195. Zhang, C., et al., *Synthesis of phosphorus-doped graphene and its multifunctional applications for oxygen reduction reaction and lithium ion batteries*. Adv Mater, 2013. **25**(35): p. 4932-7.
196. Jeon, I.Y., et al., *Edge-selectively sulfurized graphene nanoplatelets as efficient metal-free electrocatalysts for oxygen reduction reaction: the electron spin effect*. Adv Mater, 2013. **25**(42): p. 6138-45.
197. Subramanian, N.P., et al., *Nitrogen-modified carbon-based catalysts for oxygen reduction reaction in polymer electrolyte membrane fuel cells*. Journal of Power Sources, 2009. **188**(1): p. 38-44.
198. Wong, W.Y., et al., *Nitrogen-containing carbon nanotubes as cathodic catalysts for proton exchange membrane fuel cells*. Diamond and Related Materials, 2012. **22**: p. 12-22.
199. Liu, G., et al., *Studies of oxygen reduction reaction active sites and stability of nitrogen-modified carbon composite catalysts for PEM fuel cells*. Electrochimica Acta, 2010. **55**(8): p. 2853-2858.
200. Niwa, H., et al., *X-ray absorption analysis of nitrogen contribution to oxygen reduction reaction in carbon alloy cathode catalysts for polymer electrolyte fuel cells*. Journal of Power Sources, 2009. **187**(1): p. 93-97.
201. Gong, K., et al., *Nitrogen-doped carbon nanotube arrays with high electrocatalytic activity for oxygen reduction*. Science, 2009. **323**(5915): p. 760-4.
202. Voloskiy, B., et al., *Tuning the Catalytic Activity of a Metal-Organic Framework Derived Copper and Nitrogen Co-Doped Carbon Composite for Oxygen Reduction Reaction*. ACS Appl Mater Interfaces, 2016. **8**(40): p. 26769-26774.
203. Lin, Q., et al., *New heterometallic zirconium metalloporphyrin frameworks and their heteroatom-activated high-surface-area carbon derivatives*. J Am Chem Soc, 2015. **137**(6): p. 2235-8.
204. Papandrea, B., et al., *Three-dimensional graphene framework with ultra-high sulfur content for a robust lithium-sulfur battery*. Nano Research, 2016. **9**(1): p. 240-248.

205. Ma, W., et al., *An efficient electrocatalyst for oxygen reduction reaction derived from a Coporphyrin-based covalent organic framework*. *Electrochemistry Communications*, 2015. **52**: p. 53-57.

Acknowledgements

The years in which I completed my thesis were a time of both scientific development and personal growth. Many people contributed to this. A few pages in the end of my thesis are utterly insufficient to express my gratitude to all of you but I will take the opportunity to try.

I am deeply grateful to my supervisor Ger Koper. You have not only been my supervisor but also my mentor and friend. Our scientific discussions taught me a lot and you guided me on the multifaceted path in becoming an independent researcher. Your support, in an otherwise not always family friendly system, when I became a mum meant a lot to me. You are genuinely interested in people, which has been encouraging for me.

Furthermore, I would like to express my gratitude to my promotor Stephen Picken. Your contribution to this thesis and to my scientific development is of great significance. You have the ability to make science accessible and exciting by connecting fundamental research with applications, not the least inspiring kids to do more science.

I would like to thank Fokko Mulder and Hans Geerlings for your insightful comments and suggestions during the course of my thesis. I am further deeply grateful for the time and efforts from the other excellent committee members.

The ASM group has been my second family and all the staff, PhDs, Post-docs and students have all contributed immensely to my scientific development as well as to shared laughter, hardship, struggles and success.

Eduardo, your spirit cannot be contained or reduced to squared efficiency but blooms as it flies.

Jan and Rienk, thank you for welcoming me in the group and also for your suggestions and advices.

Ben, you are a gift to the group. You taught me a lot, not only about XRD. You became a grandfather at the same time as I became a mum, and you helped me putting this experience into words.

Bart, I am going to miss our corridor discussions about important and unimportant things. Thanks for your support and encouragement to be as strong as Pippi Långstrump.

Marcel, your enthusiasm and contagious inspiration you kindly share not only with us but with the next generation of scientists.

Veby, thank you for your support. Your warm personality is precious to all of us.

Angie, you are not only my closest colleague but also like a sister to me. You have meant, and still mean, a lot to me. Never stop believing in yourself, at least I will never stop believing in you.

Tomasz, I already miss you loads. Your kind, empathic and cunning mind always makes me smile and feel at home.

Serhii and Katja, wherever your road leads you, your friendship will always mean a lot to us. Thank you also for looking after the girls when we needed it the most.

Nathan, we became very good friends from the moment you arrived to Delft. Your support and encouragement meant a lot to me in the final stage of my PhD. I am looking forward to keep in touch and keep sharing thoughts. Best of luck with your new life in Colorado!

Vasu, we shared struggles and joy throughout our PhD journeys. Thank you for all the support! I appreciate a lot your optimism, humour and your attitude that nothing is impossible!

Simge, although we live far apart you are still a dear friend, a mentor and a role-model, both scientifically and personally. Your integrity, courage and ability to make everyone feel seen and heard have made a great impression on me.

Qian, thank you for all your lovely warm hugs and your incredible generosity! Best of luck, wherever your next step leads you.

Hendrik, thank you for all the inspiration and fun chats while taking the “short-cut” through the fuel cell lab.

Susan, Michelle and Audrey, thank you for all the fun moments together at work and elsewhere! You manage to brighten up just any moment!

Fanny, there is only one of you in the world! Thank you for being the curious and inspiring person you are and for teaching me to think outside the box!

Kai, best of luck to you and your family in all adventures ahead!

Karolis, I enjoyed a lot sharing office with you, listening to ABBA and discussing anything from world politics to neuroscience! Lucky me who got to know you.

Roman and Emanuela, thank you for everything you taught me. Your work greatly contributed to this piece of work.

Jos, Elena, Vincent, Yiming, Wouter, Dainius, Sander, Frank and Matija, you were all indispensable parts of our group and you made coming to work interesting and fun. Thank you for everything I learned from you!

Peggy, thank you for all the lovely chats in the lab! Your kindness and knowledge are great assets to the group!

Suellen, Elmira, Tobias, Cansel, Bowen, Fan, Irene, Lars and Benjamin, it was a pleasure working with you! Best of luck with all your different projects and ideas!

Laura and Sumit, thank you for all the great moments and your positive energy!

Mark, you were such a great office mate. Your humour make us all smile! Thank you also for correcting my Dutch summary!

Throughout my PhD I had the pleasure to collaborate with some lovely people, including Prof. Alessandro Monteverde Videla from Politecnico di Torino and the people in CarbonX, MXPolymers, ECN, NanoNextNL and HyET.

Rob Potter, thank you for giving me the chance to embark on this electrocatalysis journey! If it was not for your encouragement I am not sure I would have applied for this PhD. Your leadership will always serve as a great example to me.

Dear Lennard, Thijs, Thomas, Nirupa, Roy, Sander, Quentin and Pieter, for me one of the most enjoyable parts of my job was to supervise students. There is not anything quite like the fulfillment of seeing curious and enthusiastic students initiate projects, grow and finally master a topic. Your contribution to this thesis and to my experience as a PhD is immense. Thank you all!

~

My deepest gratitude I would like to express to my family, scattered both in Sweden, Germany and Peru. Your never-ending support and love have persistently lifted me up when I struggled. You are all each a beautiful piece of the puzzle making my life complete. Nelly, gracias por abrir mis ojos, mi corazon. Farmor, ditt intresse för lärande och ditt stora engagemang för dina barnbarn och barnbarnsbarn har betytt enormt mycket!

Maja and Alice, you make my life 4-dimensional. Your beautiful and enquiring minds fill my days with wonder and endless love. A doctor title fades in comparison to the title of being your Mum.

Last but not least, I would like to thank my dearest David, who believed in me long before I did myself. You give my life meaning and perspective. Like many other things, this thesis is our shared piece of effort.

About the author

Emma Westsson was born on May 6th 1986 in Umeå, Sweden. She received her bachelor and master degree in Chemical Engineering from Umeå University, including 6 month of exchange studies at Universidad de Murcia, Spain and 6 months of exchange studies at University of Northern British Columbia, Canada. One year she spend working at Permascand (AkzoNobel), Sweden, investigating coatings on stainless steel bipolar plates for fuel cells. She then moved to Oxfordshire, England to join Johnson Matthey as a Marie Curie Junior Researcher. There her project was focusing on applied fuel cell technology, including catalyst development and characterization. After two years she started her doctoral studies at Delft Technical University under supervision of Dr.ing Ger Koper and Prof.dr. Stephen Picken, resulting in this thesis and a number of publications.

